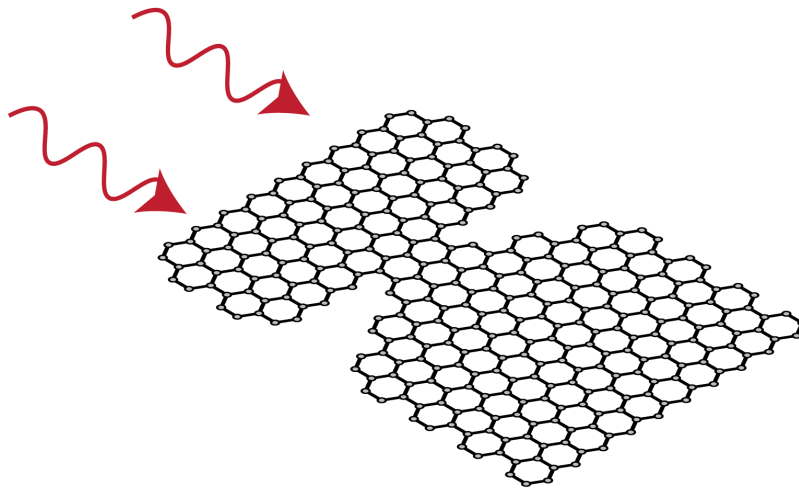MASTER THESIS

Solar energy harvesting using graphene rectennas: a proof-of-concept study

Author:
Sean Alexander Stellingwerff

Graduation committee:
Dr. ir. Herman Offerhaus (OS)
Prof. dr. Jennifer Herek (OS)
Prof. dr. ir. Wilfred van der Wiel (NE)
Prof. dr. ir. Harold Zandvliet (PIN)

UNIVERSITY OF TWENTE.

Optical Sciences
April 10, 2015

Abstract

Presented in this work is the research performed as part of a Masters assignment at the Optical Sciences group at the University of Twente. In this research, a new technique for harvesting energy from sunlight, called solar rectification, is investigated. Using graphene patterned in specific geometric shapes, it is hoped that sunlight can be converted into AC electricity by use of antennas, and then converted into usable DC electricity using so-called geometric diodes made from graphene. The hope is that graphene can be patterned in such a way that it serves both purposes simultaneously. Simulations have been done to investigate the ideal shape of geometric diodes. Graphene from different sources was characterized and several devices were fabricated. Research was done to see if these graphene devices could be used as geometric diodes, in a first step toward realizing solar rectification using geometrically patterned graphene. A successful fabrication process was established, and it was found that devices could be fabricated that showed nonlinear behavior. It could not be concluded that these devices worked as diodes, but the knowledge and experience gained during this project are expected to help future research into this topic.

Uittreksel

In dit verslag wordt het onderzoek uiteengezet, dat is gedaan als onderdeel van een afstudeeropdracht bij de vakgroep Optical Sciences aan de Universiteit Twente. In dit onderzoek is een nieuwe techniek voor het opwekken van energie uit zonlicht onderzocht, genaamd *Solar rectification* (losjes vertaald: het gelijkrichten van zonlicht). Door grafeen een bepaalde geometrische vorm te geven, wordt gehoopt dat het grafeen in staat zal zijn om zonlicht te absorberen en om te zetten in een wisselstroom, waarna deze wisselstroom met zogenoemde geometrische diodes, eveneens gemaakt van grafeen, gelijkgericht kan worden, om zo bruikbare gelijkstroom te produceren. De hoop is dat grafeen zowel kan werken als antenna en als geometrische diode. Om de ideale vorm van geometrische diodes te analyseren, zijn simulaties gedaan. Grafeen uit verschillende bronnen zijn gekarakteriseerd, en meerdere structuren zijn geproduceerd. Deze structuren zijn vervolgens geanalyseerd om te onderzoeken of deze structuren zich gedragen als geometrische diodes. Er is aangetoond dat de fabricatiemethode goed werkt en dat verschillende structuren gemaakt kunnen worden, waaronder structuren die niet-lineair gedrag vertoonden. Er kon niet worden geconcludeerd dat de structuren zich gedroegen als geometrische diodes, maar door de opgedane kennis en ervaring is het de hoop dat toekomstig onderzoek hier snel toe in staat zal zijn.

Contents

List of abbreviations

Abbreviation	Full meaning
AU	Astronomical unit
IR	Infrared
FIB	Focused ion beam
SEM	Scanning electron microscope
AC	Alternating current
DC	Direct current
FDTD	Finite-difference time-domain
MFPL	Mean free path length
CVD	Chemical vapor deposition
SP	Surface plasmon
SPP	Surface plasmon polariton
SPR	Surface plasmon resonance

Introduction

Motivation

In a world whose need for energy increases every year, fossil fuels still provide the majority of the energy today. With this use of fossil fuels come important considerations. For example, fossil fuels will run out in a not too distant future, and the use of fossil fuels contributes significantly to global warming. For these reasons, we are in need of finding reliable, environmentally less impacting methods for energy production using renewable energy sources, such as sunlight, water or the wind. Furthermore, there is a need to make these methods usable anywhere in the world and, not unimportantly, affordable to even the poorest and most remote countries. It is not surprising then that a large amount of research is focused on trying to find or optimize renewable methods for energy production. Some of these methods rely on sunlight as the source of energy. By harvesting the energy contained in sunlight, electricity can be generated, which can then directly power our cities and vehicles. The advantages of using sunlight are apparent: sunlight is a renewable source of energy and can provide usable amounts of energy almost everywhere in the world[1].

Solar energy harvesting is already a well-known phenomenon. For example, commercial technology is widely available to heat water using solar collectors or to generate electricity using solar panels. While top range commercial solar cells have reached efficiencies of around 25%, research-grade solar cells have even been shown to reach efficiencies of up to 46% [16]. These efficiencies are enough to make solar panels commercially viable alternative energy sources. However, commercial-grade and especially research-grade solar panels feature complicated technology. Most solar cells are based on specialized semiconductor technology and require rare earth materials, specially grown crystals under strict conditions and more. This naturally translates to a relatively high price for solar panels, making the widespread implementation of such technology more difficult. As a result, researchers and industry are investing greatly in research and development, resulting in more and more innovations opening up opportunities for improving or simplifying current solar panel technology, or inventing new ways of harvesting energy from sunlight.

One such innovation is made possible by the discovery of materials such as graphene. This technology works by using antennas to couple to an oscillating electromagnetic field such as radio frequency electromagnetic fields, which produces alternating current (AC) electricity. This AC electricity is then rectified, i.e. allowing current to flow only in one direction and reducing the oscillations in or 'flattening' the signal, producing direct current (DC) electricity, which can be used to power electrical devices. Because no devices existed previously that could rectify the high frequency current produced by electromagnetic fields that make up visible- or sunlight, this technology could not be used to harvest energy from it. However, with the discovery of materials such as graphene, visible light now falls within the range of rectifiable electromagnetic fields and this may lead to a new type of solar cell

---

[1]when measured as the annual average energy per square meter. At higher latitudes the amount of incident power will decrease, but even in the northern latitudes the amount of energy is above 1000 kWh/m^2 (annual average) [7].

being produced in the future.

In this thesis, a proof-of-concept study is presented which aims to investigate this new technique for solar energy harvesting. The goal of the research is to see if graphene could be patterned in such a way that a device is formed that can simultaneously couple to light like an antenna, and rectify it, like a diode, to produce DC electricity. Previous research [22] has shown that graphene can be patterned into an asymmetric shape to form what is called a geometric diode. This diode was shown to be able to rectify electromagnetic fields with a frequency of 28 THz, which is the frequency of infra-red light. In this research project, an attempt was made to make such geometric diodes as well.

Thesis outline

This thesis is split into two parts. The first part of this thesis, chapters 1 and 2, covers the theory needed to understand how the proposed device would work. Chapter 1 explains the concept of the proposed design. Chapter 2 describes the simulation models that were constructed to optimize the shape of the device. The second part of the thesis, chapters 3 through 5, covers our efforts to design, fabricate and measure the first simple devices to test the concept. Chapter 3 discusses the materials and methods of the fabrication process. Chapter 4 explains how we produced devices. Chapter 5 discusses the measurement results. The thesis is concluded with a discussion, outlook and recommendations are presented to guide future research into this topic.

Chapter 1

Background & Theory

In this chapter, background information and theory needed in the rest of the thesis is explained. The chapter begins by explaining how the most common device to harvest electrical energy from sunlight — the semiconductor-based solar cell — works. The limits and difficulties of solar cells are explained, and an alternative solar energy harvesting device, called a rectenna, is proposed. This device directly rectifies the electromagnetic field of sunlight. It will be explained that to rectify sunlight, an ultra fast diode is needed, and that conventional diodes do not respond fast enough. A new type of diode is presented, called a geometric diode, and the material that can be used to create such a diode, graphene, is introduced. Finally, the last ingredient needed to rectify sunlight, optical antennas, are introduced, and it is discussed how graphene might also be used as an antenna.

1.1   Semiconductor-based solar energy harvesting

One of the most common ways to generate electricity from sunlight today is through the use of semiconductor solar cells [15]. It is insightful to investigate how these solar cells work to understand their limitations. Coincidentally, the theory will also be useful in later sections, when we investigate an alternative method to harvest energy from sunlight.

In Fig. 1.1, n-type semiconductor and p-type semiconductor together form an interface known as a p-n junction. Such a junction is commonly found in solar cells, diodes and LEDs [11]. An n-type semiconductor is a semiconductor (e.g. silicon) that is doped with impurity ions that *donate* additional electrons to the semiconductor, making electrons the majority charge carriers in the semiconductor. This also raises the Fermi level to be closer to the conduction band than for the intrinsic semiconductor. An example of an n-type semiconductor is silicon (four electrons in the outer shell), doped with phosphorus (five electrons in the outer shell). In comparison, a p-type semiconductor is doped with impurity ions that accept electrons, meaning that holes become the majority charge carriers and consequently lowering the Fermi level to be closer to the valence band. An example of a p-type semiconductor is silicon doped with boron (three electrons in the outer shell).

When a p-n junction is formed, close to the p-n junction, electrons from the n-type semiconductor diffuse into the p-type semiconductor to recombine with holes, and holes diffuse from the p-type semiconductor into the n-type semiconductor to recombine with electrons [12]. This is illustrated in the bottom part of Fig. 1.1. This migration of charge carriers (electrons in n-type and holes in p-type semiconductors) results in a region around the p-n junction known as the depletion zone, where no current can flow from one side to the other through the junction. As electrons diffuse into the p-type semiconductor, they create negatively charged ions there, and as holes diffuse into the n-type semiconductor, they create positively charged ions. This results in an internal electric field, which prevents more
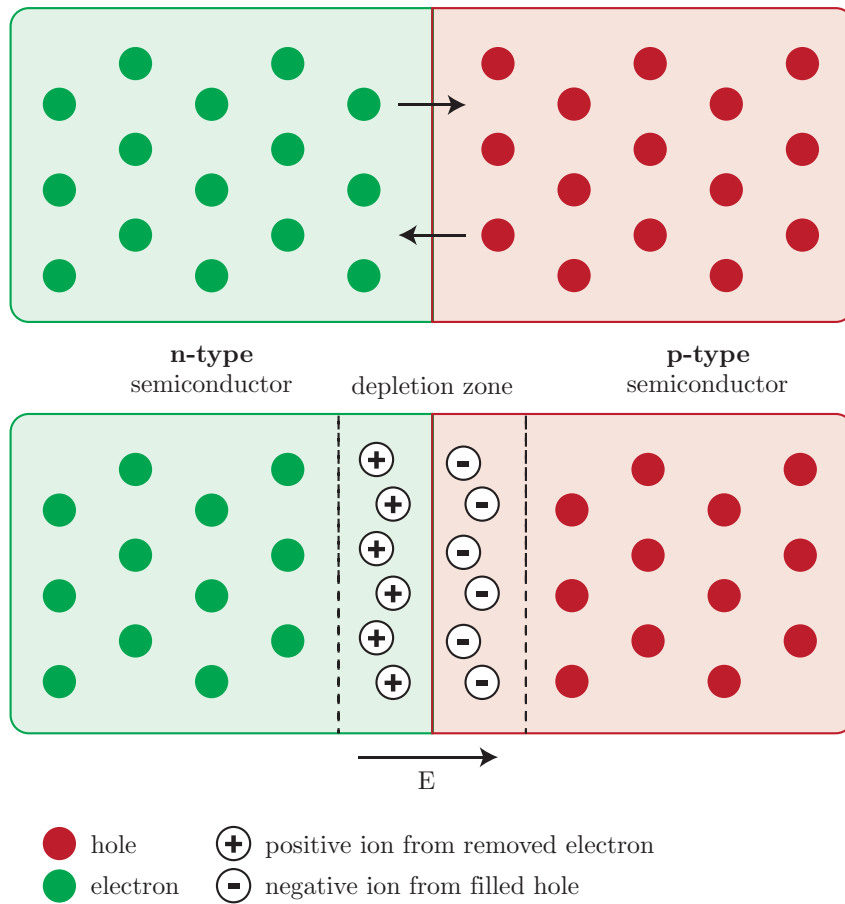
Figure 1.1: Schematic representation of a p-n junction. Two types of semiconductor, one n-type and one p-type, are brought into contact. (top) Due to an surplus of electrons in the n-type semiconductor, and a surplus of holes in the p-type semiconductor, electrons from the n-type semiconductor diffuse into the p-type semiconductor, close to the p-n junction, and vice versa. Close to the junction, this creates negatively charged ions in the p-type semiconductor, and leaves behind positively charged ions in the n-type semiconductor. (bottom) This creates a region, called the depletion zone, through which more charges cannot flow. This region grows in width until the induced internal electric field is too strong for more electrons and holes to diffuse to the other side.
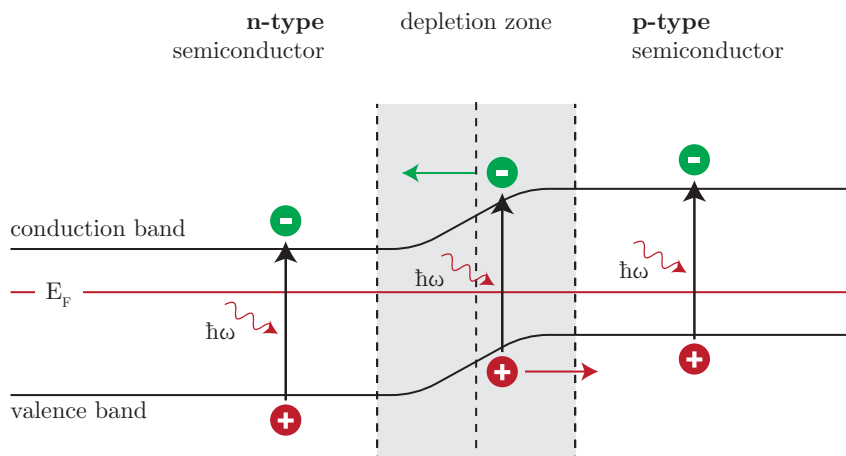
n-type semiconductor   depletion zone   **p-type** semiconductor

conduction band

E_F

$\hbar\omega$

valence band

Figure 1.2: Schematic representation of the bandgap structure of a p-n junction and the absorption of photons. Photons with an energy greater than the bandgap can generate electron-hole pairs inside the semiconductor material. Electron-hole pairs created in or around the depletion zone will experience a drift force and will flow out of the depletion zone, creating a current. Electron-hole pairs created far away from the depletion zone do not experience such a force and do not contribute significantly to the induced photo-current. (Note: in this schematic only absorption in the depletion zone is shown to generate a current for simplicity. In reality, absorption close to the depletion zone will also lead to a (small) contribution to the total photo-current.)

charges from flowing through. The width of the depletion zone will not grow indefinitely, as the internal electric field will eventually be too strong for more electrons to diffuse into the p-type semiconductor, and vice versa. This process results in a potential barrier inside the p-n junction, eventually inhibiting the flow of charges through the material.

In Fig. 1.2, the band structure of the p-n junction is drawn schematically [12], and photons are shown to be incident on the semiconductor in various regions of the p-n junction. A photon with an energy larger than the bandgap of the semiconductor, incident on the semiconductor material, can promote an electron from the valence to the conduction band, and in the process create an electron-hole pair. The electron-hole pair can be created in various regions of the p-n junction, but as can be seen in Fig. 1.2, only electron-hole pairs that are created close to the depletion zone will experience the internal electric field and will be separated, producing a current in the device. Electron-hole pairs that are created far from the depletion zone experience no such force and are likely to recombine and e.g. re-emit a photon. It is then obvious that the more photons are incident on the p-n junction, close to or inside the depletion zone, the more current will be produced.

Semiconductor-based solar cells are still the topic of much research, since efficiencies have not yet reached the theoretical limits, and production costs can potentially be reduced. Efficiencies in the commercial sector are reaching 20%, whereas research labs have reported efficiencies of up to 44.7% [15, 16]. The theoretical limit of a solar cell using a p-n junction is described by the Shockley-Queisser limit, which states that a maximum efficiency of 33.7% can be reached for a solar cell with a single p-n junction [18]. This limit occurs because the devices are selective in the photons they absorb. The photons need to have a minimum photon energy that is greater than the bandgap of the semiconductor material. Solar cells made with multiple layers of p-n junctions can overcome this limit, with a theoretical limit of 86.8% if the device is composed of an infinite number of layers [17]. Although these efficiencies and costs of production are sufficient for widespread commercialization (i.e. they are affordable enough and can earn themselves back in a reasonable amount of years), the devices come with significant complexity in terms of fabrication. Semiconductor solar cells
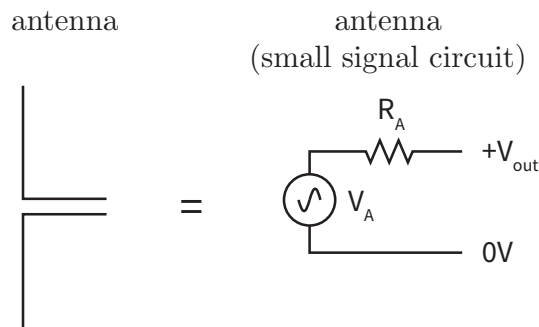
Figure 1.3: Schematic representation of an antenna which converts incident electromagnetic radiation into an oscillating voltage. The antenna can be seen as a voltage source V_A in series with an internal resistance R_A, shown on the right in the figure.

are difficult and expensive to produce, as they require e.g. the specially grown semiconductor crystals mentioned above, in specific arrangements, and transparent electrodes made with rare-earth elements. Much of the current research therefore not only focuses on trying to improve existing solar cell technology, but also on new solar energy harvesting methods.

As is apparent from the above theory, semiconductor-based solar cells rely on the photoelectric effect. An alternative method for generating electricity from light that is gaining more and more interest is called *solar rectification*. This technique makes use of so-called optical antennas in combination with rectifiers to produce DC electricity from the electromagnetic field that is light. The next section will explain how solar rectification works, and which challenges need to be overcome if this technique is to become successful.

1.2 An alternative method, rectifying EM fields

Electromagnetic fields, from microwaves to radio waves and visible light, can be coupled electrically using antennas [13]. In this coupling process, electromagnetic fields couple to electrons in the antennas, converting and concentrating the energy of the electromagnetic field into localized oscillations of electrons inside the antenna. Such antennas can be found in a wide variety of devices, from radios to mobile phones. In the case of optical antennas, applications are found in e.g. microscopy techniques where light is effectively focused well beyond the diffraction limit. The physics behind optical antennas will be discussed in more detail in section 1.5. For now, it is relevant to know that when such an antenna is connected to an electrical circuit, the antenna produces an AC-voltage output with the same frequency as the electromagnetic field. The antenna can then be seen as a voltage source with an internal resistance, as displayed in Fig. 1.3 [19].

To harvest energy from electromagnetic radiation, it is not enough to create an antenna which converts the energy in electromagnetic fields into moving electrons. The AC electricity generated by these antennas needs to be converted into DC electricity so that it can power a device at lower frequencies. This can be done using a rectifying circuit. The concept of rectification is illustrated in Fig. 1.4. Four different circuits are shown in the top-half of the figure, and the output voltage of each circuit is shown in the four graphs in the bottom-half of the figure. Circuit (1) shows an antenna (modeled here without the internal resistance for simplicity) connected to a load (modeled as a resistance). This circuit will have an output current as shown in graph (1). As can be seen, assuming the electromagnetic field has a sinusoidal shape, the output would be an alternating current with the same frequency as the electromagnetic field that induced the current. A diode could be added, which will only allow current to pass through in the forward direction. This is shown in circuit (2) and the

output is shown in graph (2). In this case, only the positive current is seen to pass through, and the output is zero whenever the current before the diode flows in the opposite direction. To increase the performance of the device further, circuit (3) adds a rectifier bridge, which converts the backwards flowing current into forward flowing current, increasing the effective energy content of the resulting total current after the rectifying bridge. This produces the output shown in graph (3). The last step is to add e.g. a low pass filter, as shown in circuit (4). This filter serves to filter out the high frequency oscillations, and in the end produces an output with far less oscillation, approximating DC electricity, as shown in graph (4).

The total process of harvesting energy from electromagnetic radiation then involves coupling to an electromagnetic field using an antenna, which generates AC electricity. This current can then be rectified using a rectifier circuit (e.g. diodes in a special configuration) after which the rectified signal is fed through a DC filter to produce DC electricity to a load (a device). The completed device is called a rectenna and is illustrated in a simplified form in Fig. 1.5.

The concept has been researched and successfully demonstrated in the past, although the focus was mostly on wireless energy transfer (e.g. see [9, 10])[1]. Most of these methods involved transmitting and rectifying microwave radiation and as such operated at GHz frequencies. The question is then if this technique could also be applied to electromagnetic fields with frequencies on the order of $10 - 10^3$ THz, corresponding to the range from IR to visible or even up to UV light. Optical-frequency nano-antennas have existed for some time [13] and have been shown to reach high coupling efficiencies. The same cannot be said for the rectifying part, however. As illustrated above, to rectify a signal, diodes are needed. Most diodes are based on semiconductor material, and these come with an inherent problem. This can be best understood using the theory that was already discussed in the case of semiconductor-based solar cells.

Semiconductor diodes, just as the solar cells described earlier, work using a p-n junction. As was discussed before, in a p-n junction, a depletion zone is formed which prevents current from flowing through the diode, since there are no charge carriers to carry the current. Another way of explaining this phenomenon is by saying that there is a potential barrier in the depletion zone. The height of the potential barrier depends on the width of the depletion zone. The wider the depletion zone, the higher the potential barrier. For an electron to travel through the barrier, it must have more energy than the potential barrier. To understand how a diode then blocks current in one direction but allows it to flow through in the other, a voltage source is connected to a diode, as shown illustrated in Fig. 1.6.

In Fig. 1.6.A, the voltage source is set to 0 V. This is effectively the same as having no battery connected at all, and so the width of the depletion zone is the equilibrium width. In Fig. 1.6.B, the voltage source is set to produce a voltage of 0.4 V across the diode, where the negative terminal of the source is connected to the n-type semiconductor and the positive terminal is connected to the p-type semiconductor. In this case, electrons are injected into the n-type semiconductor, and holes are injected into the p-type semiconductor. This pushes the electrons in the n-type semiconductor and holes in the p-type semiconductor closer to the p-n junction, reducing the width of the depletion zone. It can also be seen as an external electric field that is applied across the diode, which opposes the internal electric field inside the depletion zone. The result is that as the voltage is increased (for typical diodes to 0.7 V), the depletion zone is reduced in width until it collapses, as illustrated in Fig. 1.6.C. At this point the diode is said to be forward-biased, and electrons can cross the p-n junction, i.e. a current can flow through the diode.

The opposite occurs when the polarization of the voltage source is reversed, as illustrated in Fig. 1.6.D. In this case, the positive terminal is connected to the n-type semiconductor

_____

[1]the concept was proven to be effective in a rather extreme way in the 60s by the US Department of Defense, with the development of a helicopter whose rotors were powered using an onboard antenna-rectifying setup. See [9] for more information.
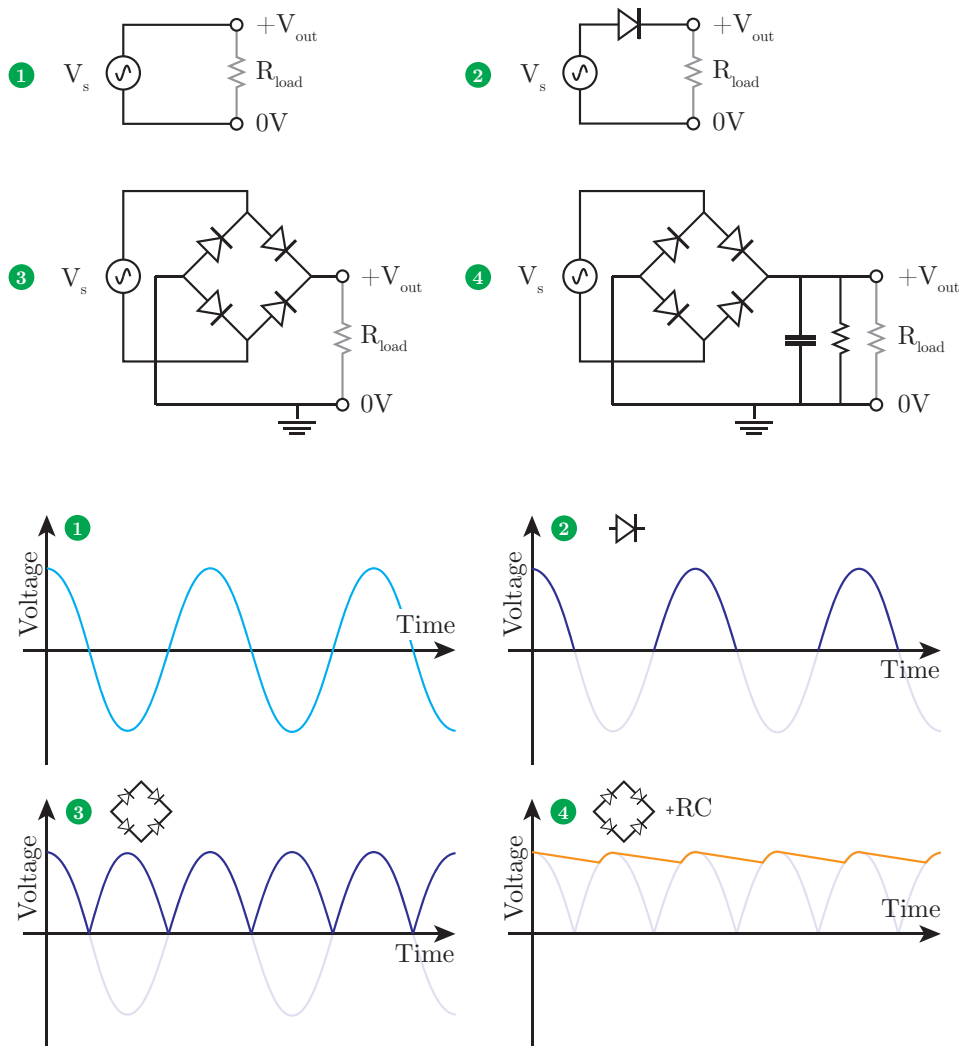
Figure 1.4: Illustration of the concept of signal rectification. The numbered circuits (top) correspond to the numbered signals (bottom). (1) an antenna is modeled as a voltage source, producing a varying voltage V_S. The output voltage V_{out} (which in this case is equal to V_S) across a load resistance is shown in the corresponding graph. (2) A diode is introduced, which only allows forward flowing current to pass through, resulting in the output shown in the corresponding graph. (3) if a bridge rectifier is used, the signal is rectified to yield more bumps. (4) Finally, adding an RC filter, which serves as a low-pass filter, or a DC filter, converts the output into a (quasi-)DC output. The height of the final oscillations depends on the design of the filter.
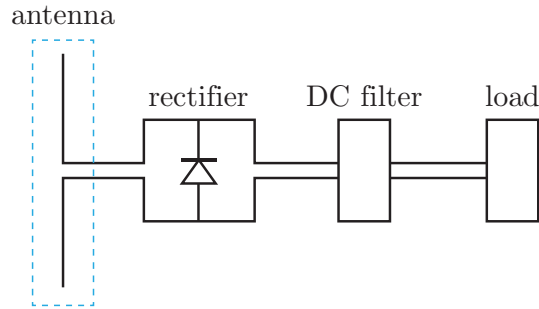
Figure 1.5: Diagram of a solar rectification (rectenna) circuit. In solar rectification, an antenna couples to the EM field (e.g. radio waves or light), meaning electrons inside the antenna absorb part of the energy in the EM field and oscillate as a result, effectively producing AC electricity. This signal is then rectified in a rectifier circuit, typically comprised of one or more diodes in a specific arrangement. This rectified signal then passes through a DC filter, which smooths out the signal and generates a DC current. The figure is based on Fig. 1.1 in [19].
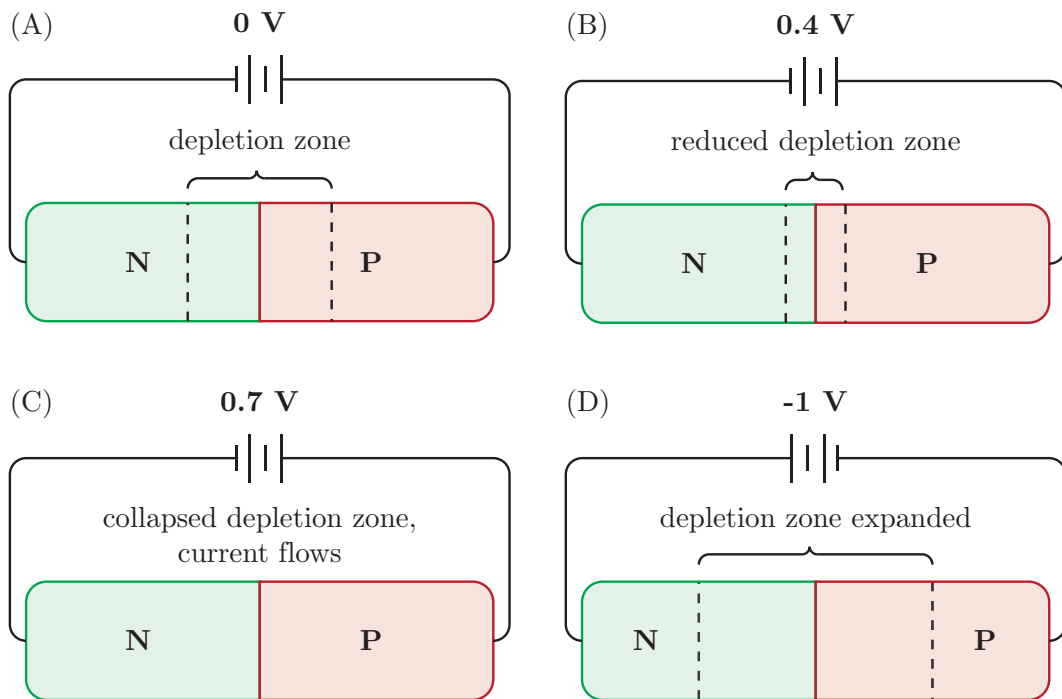

Figure 1.6: Illustration showing the workings of semiconductor diodes. A voltage source is connected to a p-n junction diode. In (A), the voltage source is set to apply 0 V across the diode. In this case the depletion zone has its equilibrium width. In (B), the voltage source is set to apply 0.4 V across the diode, where the negative terminal of the voltage source is connected to the n-type semiconductor, and the positive terminal is connected to the p-type semiconductor. This has the effect that the depletion zone is reduced in width. In (C), the voltage across the diode is increased, leading to the depletion zone collapsing. Current can now flow through the diode and it is said to be forward-biased. In (D), the terminals of the voltage source are reversed and the voltage across the diode is set to 1 V. In this case the depletion zone is increased in width and current cannot flow through the diode.

and the negative terminal is connected to the p-type semiconductor. This pulls electrons in the n-type semiconductor and holes in the p-type semiconductor away from the interface, increasing the width of the depletion zone. As before, it can also be seen as an applied external electric field that points in the same direction as the internal electric field inside the depletion zone. The result is that the potential barrier is increased in height and current cannot flow through the diode. The diode is now said to be reverse-biased.

It is now clear why a semiconductor diode allows current to flow through in one direction, but stops current from flowing through in the other direction. This does not yet explain why such diodes cannot work up to THz frequencies, however. To help understand that, a sinusoidal voltage is applied to the diode. If a sinusoidal voltage is applied to the diode, the diode must constantly switch between forward biased mode and reverse biased mode each time the applied voltage changes sign. The electrons inside a semiconductor have a limited electron mobility, defined by

$$\vec{v}_d = \mu \vec{E}. \tag{1.1}$$

In equation 1.1, an electric field $\vec{E}$ is applied to the material, $\vec{v}_d$ is the drift velocity that the electrons get due to the applied electric field, and μ is the electron mobility. The electron mobility is thus a measure for the 'responsiveness' of electrons inside a material. Electrons in a material with a higher electron mobility will get a higher drift velocity as a result of an applied electric field than a material with a lower electron mobility. This implicitly also means that electrons will not be able to follow the oscillations in an electromagnetic field if the frequency of the electric field becomes too large. Due to the limited drift velocity of electrons, the depletion zone cannot be switched fast enough[2]. For this reason, semiconductor-based diodes have maximum operating frequencies up to several GHz. Beyond this frequency, the diode cannot respond fast enough, and will no longer rectify the signal.

Another way of looking at this is by considering the equivalent small-signal circuit of a semiconductor diode [19]. In the small-signal regime, only very small variations around a DC voltage are modeled. In this case, a diode can in its simplest form be modeled as a parallel resistance and capacitance. The capacitance of a diode originates mostly from the separated charges in the depletion zone. The combination of a resistance and capacitance leads to an RC-time. In order to respond to high frequency oscillations, the RC-time of a diode must therefore be small enough. In Fig. 1.11, the wavelength of light with the highest intensity is 500 nm, which corresponds to a frequency of 600 THz, and thus with a time constant of $\tau = 1/2\pi f \approx 0.3 fs$. For a diode to respond fast enough to such frequencies, the RC-time must therefore be smaller than 0.3 fs.

Different types of diodes have been developed and researched in an attempt to reach such RC-times. An example of such diodes is the metal-insulator-metal (MIM) diode. Such a diode can respond up to several THz (IR) frequencies [19, 14, 20]. They are made of a thin layer of insulator (less than 10 nm thick) sandwiched in between two thin sheets of metal. This forms a so-called tunnel diode. The band diagram of a MIM diode when a bias voltage is applied across it is illustrated in Fig. 1.7. When no bias voltage is applied, the Fermi levels of both metals are the same. The insulator in between the two metals introduces a higher potential barrier through which electrons cannot tunnel, unless they have an energy higher than the potential barrier. If a negative bias voltage is applied across the diode, the Fermi level of one of the metals (e.g. metal 1) is raised, until it is high enough so that electrons

---

[2]there is an illustrative analogy: think of a canal with a heavy steel door, with the hinge at one side of the canal and a door stop at the other side, so that the door can open one way only. If the water flows in the forward direction, the door is opened, depending on the strength of flow, i.e. the door is heavy. In the opposite direction, the door is closed slowly until it is fully shut. If the flow is now sinusoidal with a high frequency, the door will not be able to open and close fast enough, meaning it remains in a position somewhere in between.
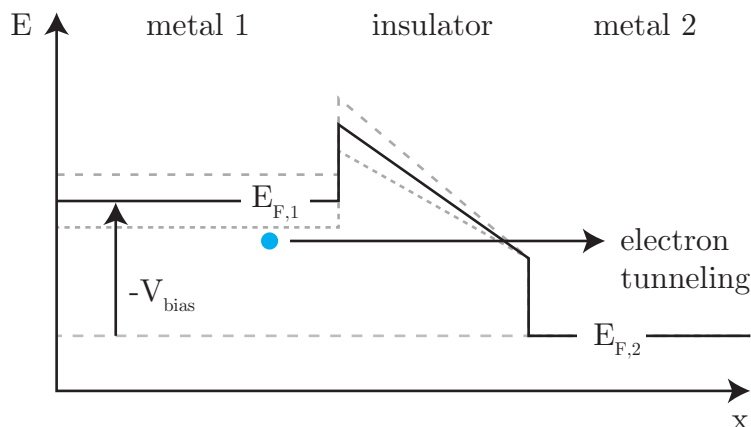
Figure 1.7: Band diagram of a typical MIM diode operating under bias voltage [19].
When no bias voltage is applied, the Fermi levels of both metals, $E_{F,1}$ and $E_{F,2}$ are at the same
level. The insulator introduces a high potential barrier through which electrons cannot tunnel. If a
negative bias voltage is applied across the diode (as shown), the Fermi level of e.g. metal 1 is raised,
until it is high enough so that electrons can tunnel through the potential barrier. If a positive bias
voltage is applied, the opposite occurs and electrons cannot pass through the potential barrier. The
figure is inspired by Fig. 2.2 in [19] and Fig. 1-2 in [20].

can tunnel through the potential barrier. If instead a positive bias voltage is applied, the
opposite occurs and electrons cannot pass through the potential barrier.

As mentioned, MIM diodes have been shown to have operating frequencies up to a few
THz. However, for higher frequency applications, their RC-times are still too long and
therefore alternatives must be considered. Variations on MIM diodes have been investigated
[19], with e.g. multiple insulator layers (MIIM diodes), but each of these comes with their
own set of difficulties, where the RC-times are constantly too large.

It is clear then that a major challenge exists. Antennas for optical rectification can be
found and are discussed later in this chapter, but diodes form the biggest challenge by far.
In the next section, a possible alternative solution for a diode is discussed, the *geometric
diode*.

1.3 Geometric diodes

In a geometric diode, the ballistic movement of electrons, combined with a geometrically
asymmetric structure, produces a nonlinear I(V) response [19]. This means that a structure
can be produced where current flowing through the device could, for instance, flow more
easily in one direction than the other. The concept is best understood using Fig. 1.8. In
Fig. 1.8, an example of an asymmetrically patterned thin sheet material is sketched. The
material is assumed to have an electron mean-free path length (MFPL) that is comparable
to or greater than the size of the asymmetry. This electron MFPL of a material describes
the average distance that an electron can travel freely between collisions (with, for example,
atoms in the material). If a material has an MFPL that is large compared to the asymmetric
structure, the electrons can be considered to move ballistically. This is also referred to as
ballistic transport. When a ballistic electron moves towards a boundary of the patterned
material (indicated by the solid outline in Fig. 1.8), it will reflect, changing its direction of
movement. The exact direction of reflection may be specular or not, depending on the exact
atomic composition of the material around the edge, but the net result of many electrons
moving in the material in this way is that electrons move more easily in the direction of the
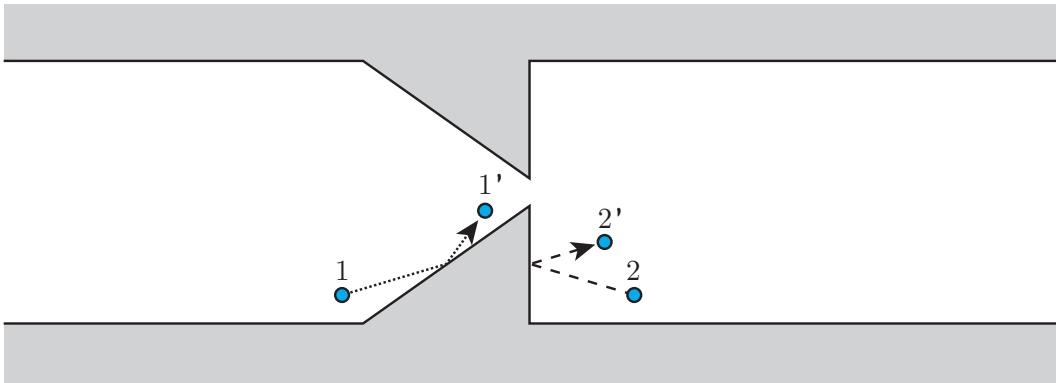
Figure 1.8: Illustration showing the concept of a geometric diode. The white region shows an asymmetrically patterned material in which electrons can move, and the gray region indicates a nonconductive substrate. Blue circles represent electrons in the material and the arrows indicate in which direction each electron moves. The figure shows that due to the asymmetric shape of the material, combined with the assumed large mean-free path length of the electrons in this material, electrons moving to the right are more likely to pass through the gap than electrons moving to the left.

arrowhead than in the opposite direction. The end result is an asymmetric current, as a result of the shape of the device. Hence the name geometric diode.

To construct a geometric diode, first, a material is needed that has a sufficiently high electron MFPL. The material needs to be patterned so that it has an asymmetric shape like in Fig. 1.8. In most metals, the electron MFPL is around 10-30 nm around room temperature [21], so the asymmetric shape itself must be several times smaller than 10-30 nm for the shape to have a noticeable effect on the electron movement. Even with modern lithographic methods, such a resolution is difficult to achieve. Therefore, a material with a larger MFPL is desired. Second, in chapter 2, simulations will indicate that geometric diodes show good asymmetry for higher voltage drops across the diode. At these voltages, the material of the diodes needs to be able to support current densities on the order of 10^7 A cm^{-2}.

Previous research has been performed to discover if geometric diodes could be created for the purpose of solar rectification. Metal (silver) was initially investigated as a material by Zhu et al. in [22], but difficulties in achieving sufficient resolution for patterning and electromigration[3] rendered this material inadequate. Graphene was suggested as a material for geometric diodes due to its large MFPL, which can be more than 1 micrometer [26, 27], and was demonstrated to work for rectification at 28 THz [22]. These results and graphene's properties seem to make graphene a good candidate for even higher frequency rectification, meaning it could be perhaps be used to rectify visible light. It is for those reasons that graphene was also used as the material of choice for the proof-of-concept devices made during the research described in this thesis.

To understand why graphene has such good properties, graphene is analyzed in more detail in the next section.

1.4 Graphene

Graphene is a so-called *allotrope* of carbon, meaning it is a specific structural form of carbon. It is a 2D material, composed of carbon atoms in a hexagonal (or: honeycomb-)lattice, as

---

[3]high current densities can lead to physical movement of ions in the conducting material. The material therefore deforms or shifts, altering the shape and possibly creating interruptions. See [25].
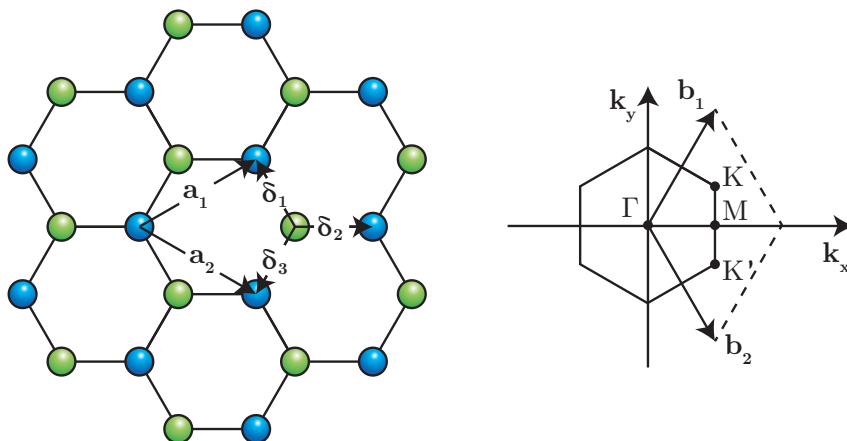
Figure 1.9: The hexagonal lattice (left) and the Brillouin zone (right) of graphene. The green and blue spheres represent carbon atoms and the solid lines represent σ-bonds. Vectors $\vec{a}_1$ and $\vec{a}_2$ define the triangular unit cell of graphene. Graphene can be seen as two triangular lattices interwoven, as indicated by the blue and green spheres. Figure based on Fig. 2 in [26].

illustrated in Fig. 1.9. The lattice, in theory, extends infinitely in both directions of the 2D plane. Each carbon atom has three strong σ-bonds with its nearest-neighbor atoms, as indicated by the solid lines in Fig. 1.9, and one π-bond that is oriented out of the plane of the paper (not shown).

The lattice of graphene can be seen as two triangular lattices that are interwoven, as indicated in Fig. 1.9 by the blue and green sublattices. The triangular unit cell is defined by the lattice vectors $\vec{a}_1$ and $\vec{a}_2$ [26],

$$\vec{a}_1 = \frac{a}{2}(3, \sqrt{3}), \ \ \vec{a}_1 = \frac{a}{2}(3, -\sqrt{3}). \tag{1.2}$$

Here, the distance between two carbon atoms, a ≈ 1.42Å. Each carbon atom can be seen to have three nearest-neighbor atoms, located at $\vec{\delta}_1 = \frac{a}{2}(1, \sqrt{3})$, $\vec{\delta}_2 = \frac{a}{2}(1, -\sqrt{3})$, $\vec{\delta}_3 = -a(1,0)$, and six next nearest-neighbor atoms, located at $\vec{\delta}_1' = \pm\vec{a}_1$, $\vec{\delta}_2' = \pm\vec{a}_2$, $\vec{\delta}_3' = \pm(\vec{a}_2 - \vec{a}_1)$.

A so-called tight-binding model can be used to determine the electronic band structure, or energy-momentum relation, of the electrons in graphene [29, 32]. In this model, electrons are assumed to be tightly bound to their atoms, and only have limited interactions with states in e.g. nearest-neighbor and next nearest-neighbor atoms. Furthermore, it is assumed that the three electrons forming σ-bonds do not contribute to conduction, and only the fourth π-electron contributes to conduction. These π-electrons are then assumed to be able to 'hop' only to the nearest-neighbor or next nearest-neighbor atoms. In that case, the band structure of the π-electrons takes on the form [29, 26]

$$E_{\pm}(\vec{k}) = \pm t\sqrt{3 + f(\vec{k})} - t'f(\vec{k}), \tag{1.3}$$

where

$$f(\vec{k}) = 2\cos\sqrt{3}k_y a + 4\cos\frac{\sqrt{3}}{2}k_y a \cos\frac{3}{2}k_x a.$$

The sign in equation 1.3 denotes the upper π^*-band (the conduction band, i.e. electrons) or the lower π-band (the valence band, i.e. holes) of graphene. The hopping parameters t
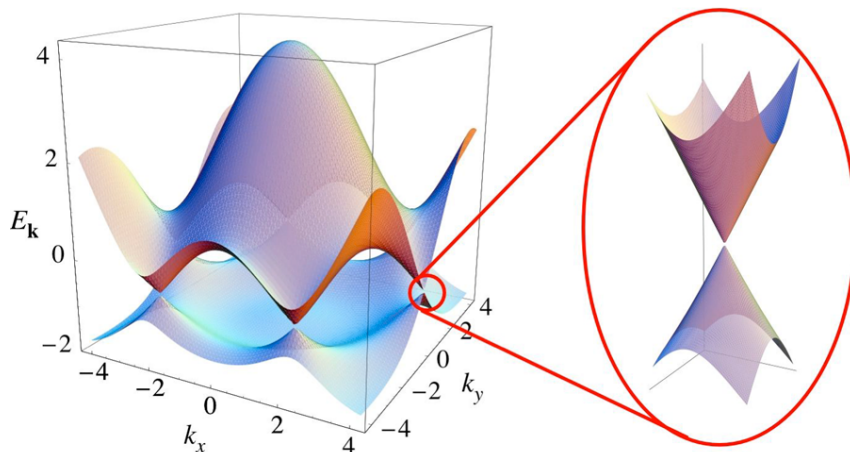
Figure 1.10: Band structure of graphene. The left part of the image shows the band structure of a single hexagonal ring. On the right, a zoom in of the band structure around one of the so-called Dirac points (K or K' in the Brillouin zone) is shown. Image taken from Fig. 3 in [26].

and t' indicate how 'easy' it is for the electron to hop to a nearest-neighbor or next nearest-neighbor atom, respectively, with a value greater than zero indicating that the likeliness that an electron can hop is higher. In graphene, t $\approx$ 2.8 eV and t' $\approx$ 0.1 eV [31].

In Fig. 1.10, the energy band is drawn for values t = 2.7 eV and t' = -0.2 t. From equation 1.3, it is clear that if t' = 0, the upper and lower bands are symmetric around E = 0. The bands are asymmetric whenever t' $\neq$ 0, however. This means that if an electron-hole pair is generated in the graphene when t' = 0, the energies are always equal in magnitude. However, if t' $\neq$ 0, then the energies are not equal in magnitude, and the symmetry is broken, leading to *electronic dispersion*.

On the right side of Fig. 1.10, a close-up is shown of the band structure at one of the so-called Dirac points. These points are located at each of the corners of the Brillouin zone, as shown in Fig. 1.9. The band structure can be approximated, close to these Dirac points, by expanding equation 1.3 using $\vec{k} = \vec{K} + \vec{q}$, where $\vec{q} = \hbar\vec{k} \ll |\vec{K}|$ is the momentum of the electron relative to the Dirac point. The resulting energy band close to the Dirac points is described by [29]

$$E_{\pm}(\vec{q}) \approx \pm v_F \hbar |\vec{q}|, \tag{1.4}$$

where v_F is the Fermi velocity of the electrons, defined as $v_F = 3ta/2$, which results in $v_F \approx 1 \times 10^6 \mathrm{ms}^{-1}$, in the case of graphene.

Equation 1.4 shows that the energy-momentum relation of electrons close to the Dirac point (i.e. for low-energy electrons) is linear in $\vec{q}$. Conventionally, the interaction of electrons with the lattice in semiconductors can be described using a finite (effective) electron mass, m*. The energy-momentum relation for those electrons, expectedly, depends quadratically on their momentum, $\vec{k}$, i.e. $E(\vec{k}) = \vec{k}^2/(2m)$. However, the energy-momentum relation of an electron in graphene, around the Dirac point, turns out to be linear in $\vec{k}$, which resembles that of ultra relativistic particles and not of particles with a mass. It turns out then that the behavior of the electrons can be described with a massless version of the relativistic Dirac equation. Apparently, the electron behaves like a massless Fermion, moving at velocity v_F. In other words, it is more reminiscent of a photon than conventional electrons. The difference between electrons in graphene and photons, however, is that an electron in graphene moves at a speed that is about 300 times smaller than that of light.

In its neutral state, the Fermi level of undoped, defect-free graphene is exactly at the

intersection of the valence and conductance band [30]. This is the reason why graphene is often referred to as a zero bandgap semiconductor, or semimetal. Since the Fermi level is at the intersection, this means that the π-electrons behave like the massless Fermions as described above, moving at a velocity v_F. This explains why in graphene, electrons respond so fast to external forces, resulting in a very high electron mobility for graphene. Furthermore, around this Dirac points, the symmetry between electrons and holes is high, explaining why the behavior of both electrons and holes in graphene are so similar. If graphene is placed on a non-conducting substrate, such as SiO_2, the electron mobility in graphene can be as high as 200 000 $cm^2V^{-1}s^{-1}$ for temperatures below 200 K [28, 33, 34]. At temperatures above 200 K, the electron mobility will be limited to 40 000 $cm^2V^{-1}s^{-1}$ due to scattering of the electrons by thermally induced surface phonons in the SiO_2 substrate. In comparison, the electron mobility of silicon at room temperature is 1 400 $cm^2V^{-1}s^{-1}$ and the hole mobility is 450 $cm^2V^{-1}s^{-1}$ [35].

In addition to the electron mobility, the MFPL in graphene is also relatively long, which can be more than 1 μm [26, 27]. This can be understood qualitatively as follows. The π-electrons in graphene are strongly localized in the plane of the graphene, but are only loosely bound to the carbon atoms. In other words, the electrons are able to move freely in the planes above and below the graphene, but are confined to that plane — they can move in a 2D plane. As long as the graphene is defect-free, such electrons can travel very long distances without encountering scattering points, such as atoms or disorders in the lattice. In contrast, free electrons in metals and semiconductors move through a three-dimensional lattice, where electrons are far more likely to encounter scattering sites. Atoms that make up the lattice, impurities and thermal vibrations in the lattice limit the MFPL to tens of nanometers [36, 21].

Lastly, graphene has also been shown to be able to support very high current densities, of over $10^8A\ cm^{-2}$ [28].

It is important to note that the (electronic) properties of graphene are dependent on the amount of impurities in the lattice. Doping or impurities in the graphene can alter the band structure, destroying the electron-hole symmetry and increasing the bandgap to a finite value [37]. Impurities will also introduce scattering sites, meaning that the effective electron mobility and MFPL in graphene are reduced. However, not only impurities have such effects. Substrates such as SiO_2 can also have an effect on the electronic properties of graphene, for example due to scattering by thermally induced surface phonons [33]. The quality of the graphene therefore depends largely on the manufacturing process. Graphene can be made using many different techniques. The earliest method used by Geim and Novoselov is called mechanical exfoliation [38]. The process used to create the graphene used in the research described in this thesis is called chemical vapor deposition (CVD). In mechanical exfoliation, also called the 'scotch tape method', graphite is repeatedly peeled to produce flakes of single layer graphene which can be transferred to SiO_2. In CVD, graphene is grown on e.g. copper substrates by exposing the substrate to finely controlled vapors of gases that react at the surface to create a graphene layer. This graphene can then be transferred to other substrates using conventional transfer methods. Both methods have clear advantages and disadvantages. For example, although exfoliation produces more pure graphene samples, the size of the samples is limited, whereas CVD produces less pure graphene, but on much larger scales.

It is clear that graphene has exceptional properties that make it a good material to make geometric diodes with. As mentioned, previous research [22] has shown that graphene can be used to create diodes that respond up to 28 THz. The MFPL of the graphene used in [22] was measured to be about 45 nm. It was shown that the MFPL is a key parameter in the performance of the diodes, with higher MFPLs leading to greater current asymmetries. Therefore, future enhancements in the fabrication process of graphene geometric diodes could lead to even higher frequency rectification.

The solar rectification challenge is now partially met. By patterning graphene in an asymmetric form, a diode can be made that can rectify oscillating electric currents at frequencies close to that of visible light. However, an important other part of solar rectification involves coupling to the electromagnetic field of light, in order to create the oscillating electric currents. The next section will discuss how light can be coupled. The section starts with a brief summary of the important properties of sunlight and then continues to discuss antennas in the optical regime, and shows how graphene might be used to create optical nanoantennas.

1.5 Coupling to (sun)light

Coupling to light (an electromagnetic field) can be done using an antenna. An antenna is a device that converts an electromagnetic field into localized oscillations of electrons. The external electromagnetic field of radio waves, for example, will exert forces on the electrons inside a metal antenna. These forces, assuming that the electrons in the material can respond fast enough, will move the electrons back and forth, creating an oscillating current or voltage across the antenna terminals, which can then be measured. If the antenna is shaped the right way and has the right dimensions, these oscillations can become resonant, enhancing the signal, much like water in a bathtub, or or a pendulum excited at the right frequency. Such an antenna is often called a resonant antenna — examples include a dipole antenna. The output signals can then be amplified and measured in a connected circuit, to produce e.g. a radio, or a WiFi antenna. In the case of optical electromagnetic fields, i.e. light, antennas become slightly more complicated. Before the details of optical antennas are discussed, it is relevant to summarize the properties of sunlight.

Properties of sunlight

Sunlight, or solar radiation, is thermal light produced at the surface of the sun. The properties of solar radiation depend on where they are measured. In Fig. 1.11, the solar radiation spectrum is shown at the top of Earth's atmosphere (indicated by the yellow area) and at sea level (indicated by the red area) [2]. There, it can be seen that the spectrum at the top of the atmosphere approximates that of a blackbody radiator with a temperature of approximately 5800 K (the solid black curve). Due to the absorption of sunlight at certain wavelengths by e.g. water, oxygen and carbon dioxide in the atmosphere, the solar radiation spectrum at sea level differs from the spectrum at the top of the atmosphere and shows clear absorption bands.

The part of the spectrum visible to the human eye, i.e. visible light, corresponds to a narrow band of wavelengths between 400-700 nm. A substantial part of the solar spectrum consists of UV and infrared light and is thus invisible to the human eye. Although a significant part of the energy in sunlight (43%) is contained in the visible light portion, the UV (5%) and IR parts (52%) of the spectrum contain a substantial amount of energy which can and are harvested [6]. This broadband spectrum allows many different antennas to be constructed, each of which could focus on specific ranges of wavelengths.

The total amount of solar irradiance, in units of W m^{-2}, averaged over a year, incident on a surface perpendicular to the sun and at the same distance from the sun as Earth $(1.4960 \times 10^{11}$ m) has been measured to be 1.361×10^3 W m^{-2} [1][4]. This is the amount of energy incident in outer space. Parts of the solar radiation are absorbed and reflected back into space by the atmosphere before it reaches the surface of the earth. The amount of solar radiation energy that is incident on the surface of the earth at a certain location,

---

[4]note that the solar irradiance varies throughout the year due to the varying distance of the earth from the sun as a result of the elliptic orbit of the earth, meaning that the irradiance varies from a minimum of 1.321×10^3 W m^{-2} to a maximum of 1.413×10^3 W m^{-2}.
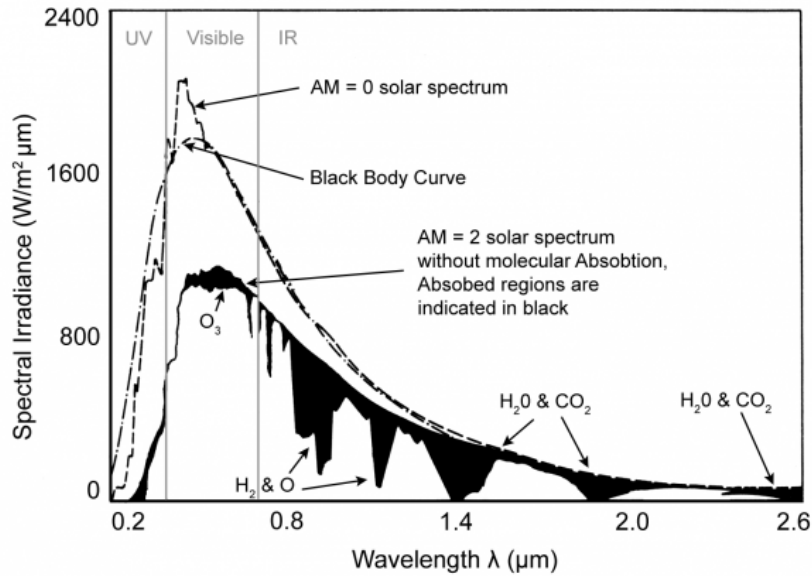
Figure 1.11: Solar radiation spectrum. The AM = 0 curve shows the spectrum of sunlight at the top of the atmosphere, i.e. incident on the earth in space. The AM = 2 curve shows the spectrum of sunlight incident on the surface of the earth, at sea level. The Black Body Curve shows a reference 5800 K blackbody spectrum. Figure taken from [2].

measured during a certain period of time, is called the insolation and has units of J m^{-2} per unit time (e.g. an hour or a day). This value is dependent on the total distance that the light has to travel through the atmosphere and the weather conditions and thus varies between locations and times. For a surface perpendicular to the sun, on a clear day and at sea level, the irradiance is measured to be approximately 1050 W m^{-2} [5].

In Fig. 1.12, the total amount of solar radiation energy reaching the surface of the earth is displayed on a world map in units of kWh m^{-2}, summed over a year or averaged per day [7]. The map shows that per year, most northern regions of the world receive about 1000 kWh of solar radiation energy per square meter, whereas some regions can receive as much as 2700 kWh per square meter. As an illustration, in the years 2000-2012, the average electricity consumption per household in the world was 3272 kWh per year [8]. This means that, if at a certain location on the world 1000 kWh m^{-2} of solar radiation is received in a year, with current high end commercial solar panels having efficiencies of around 20%, it would take roughly 16 m^2 of solar panels to make a house energy-neutral. With higher efficiency solar harvesting devices, this area could be reduced. This shows that solar energy harvesting offers real potential and there is room for improvement.

Last, the spatial coherence of relatively broadband sunlight on the surface of the earth has been measured to be on the order of 19 μm [4] and the spatial coherence can be even more when sunlight is filtered [3]. The spatial coherence of sunlight plays a crucial role when converting sunlight into electricity using antennas. As mentioned, the antenna converts light and generates an oscillating current. Multiple antennas could, for example, be combined, to increase the current and the efficiency of the geometric diode[5]. If the spatial coherence area of the incident light is smaller than the area of antennas receiving the light, the currents will not add up coherently, reducing the overall efficiency of the rectification process. Focusing light onto antennas faces the same difficulties, since it does not increase the spatial coherence.

---

[5]It will be shown in chapter 2 that an increase in voltage across the diode also increases the asymmetry and thus the efficiency of the diode.
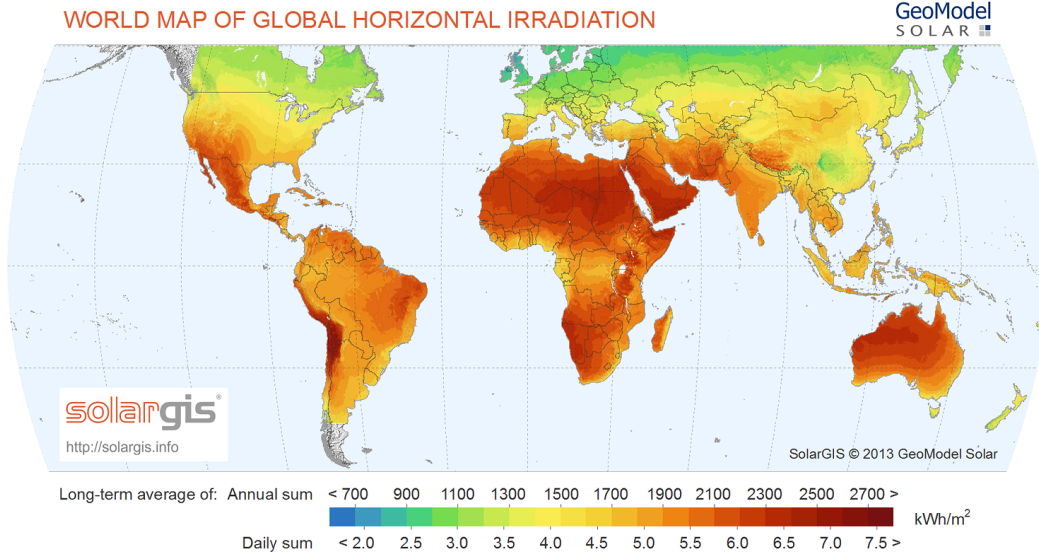
Figure 1.12: World map of global horizontal irradiation. This map shows the total amount of energy that is incident on the surface of the earth, over a year (above the color scale) and averaged per day (below the color scale). Image taken from [7].

Although e.g. radio antennas are well understood, and can be described using classical wave theory, optical antennas often work quite differently. A part of optical antennas can be described using the theory of surface plasmon polaritons (SPPs). In the next section, the theory behind SPPs will be briefly summarized and it is shown how optical antennas make use of such SPPs to create resonant structures, which can absorb and concentrate a large part of the light that is incident on them.

Surface plasmon polaritons

A surface plasmon polariton is an electromagnetic wave that propagates along a metal-dielectric interface, which is confined evanescently in the direction perpendicular to that interface (i.e. it decays in that direction) [39, 40, 41]. It can be thought of as the combination of both an electromagnetic wave in the dielectric, and an oscillation or motion of electrons at the surface of the metal. SPPs can actually propagate on any interface for which the real parts of the dielectric functions changes sign, e.g. metal and air. The interface is illustrated in Fig. 1.13.

The magnetic and electric fields can be determined for both materials. Across the interface, the continuity of these magnetic and electric fields requires that the following conditions are met [39, 42]:

$$\frac{k_{z,2}}{k_{z,1}} = -\frac{\epsilon_2}{\epsilon_1(\omega)},$$

and

$$k_{z,1}^2 = k_x^2 - k_0^2 \epsilon_1(\omega) k_{z,2}^2 = k_x^2 - k_0^2 \epsilon_2.$$

Here, $k_{z,i}$, $i = 1, 2$ describes the wave vectors of the electromagnetic fields traveling in the materials on both sides, perpendicular to the interface, k_x describes the wave vector of the electromagnetic field traveling along the interface, and $k_0 = \omega/c$ is the wave vector of the

air: $\varepsilon_2 > 0$

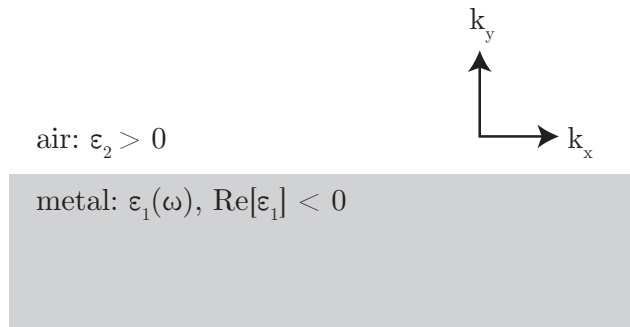metal: $\varepsilon_1(\omega)$, $\mathrm{Re}[\varepsilon_1] < 0$

Figure 1.13: Illustration showing the interface between metal and air. The dielectric function of air is assumed to be constant and real positive, whereas the dielectric function of the metal has a negative real part and depends on ω.

propagating wave in vacuum. These two equations can be combined to form the dispersion relation of SPPs propagating along the interface of the two materials [39]:

$$k_x = k_0 \sqrt{\frac{\epsilon_1(\omega)\epsilon_2}{\epsilon_1(\omega) + \epsilon_2}}. \tag{1.5}$$

In Fig. 1.14, the SPP dispersion is shown for a metal with a dielectric function given by $\epsilon_1(\omega) = 1 - \omega_p^2/\omega^2$ [40]. The dielectric material is taken to be vacuum in the figure, but could also be replaced by e.g. air. Here, $\omega_p = \sqrt{ne^2/(\epsilon_0 m^*)}$ is the resonance (or plasma) frequency of the electrons in the metal, as they oscillate around the nucleus of the metal ions, n is the electron density, e is the electron charge, ϵ_0 is the vacuum permittivity and m^* is the effective mass of the electrons in the metal. The dispersion curve approaches that of the light curve at low values of k_x, or low frequencies, meaning that in that limit, the SSPs behave like photons [40]. As k_x increases, however, the frequency reaches a limit called the surface plasmon frequency [41],

$$\omega_{sp} = \frac{\omega_p}{\sqrt{1 + \epsilon_2}}. \tag{1.6}$$

In Fig. 1.14, it can be seen that the SPP dispersion curve lies below the free space light curve, $\omega = ck$, for all values of k_x. This directly implies that SPPs cannot be excited by direct illumination with light, because both the energy and momentum needs to be conserved, i.e. $\omega = \omega_{SPP}$ and $k = k_{SPP}$ cannot both be satisfied at the same time. In order to couple light to an SPP, momentum transfer therefore has to be established. Gratings or prisms can be used to achieve this [39]. Once the light is coupled to an SPP, the SPP can propagate along the interface[6].

The above theory assumes that the metal is infinitely thick, and that the interface extends towards infinity in all directions. The theory changes slightly when looking at optical antennas, as optical antennas are usually made of metallic nanostructures that have a finite size. Still, the theory described above gives a qualitative impression of what occurs in such nanoantennas. In the case of optical antennas, the surface plasmons are called localized surface plasmons (LSPs) [42], due to their localized nature. Because the surface along which the surface plasmons propagate is now finite in size, the LSPs will reflect as they reach the edges. In that case, depending on the length of the surface, plasmons with a certain

---

[6]Note that most metals are not perfect, meaning they do not have a purely real dielectric function. Instead, most metals also have an imaginary component, which describes damping. This means that SPPs can propagate a certain distance, before the energy is dissipated. For simplicity, this is ignored for now and the focus is on the qualitative behavior of SPPs.
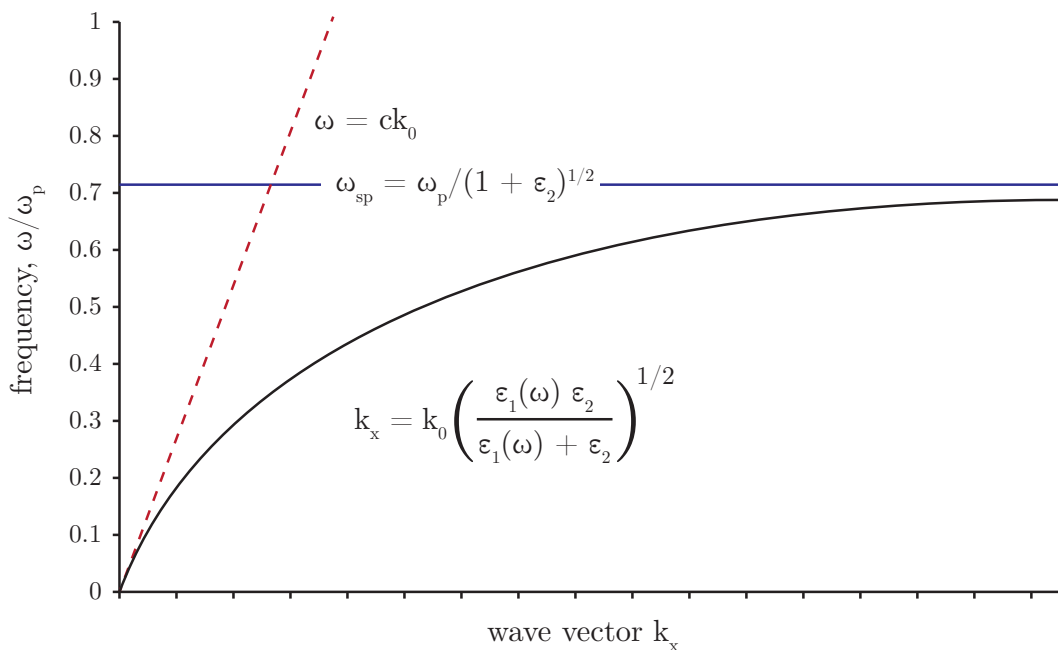
Figure 1.14: Dispersion graph for surface plasmon polaritons. The frequency on the vertical axis has been normalized to ω_p. The solid curve shows the SPPs dispersion for a metal. The red dashed line shows the free space light curve in vacuum. The horizontal blue dashed line shows the surface plasma frequency.

wavelength can start to resonate, comparable to what happens in a Fabry-Pérot cavity. For example, say that the wavelength of the LSP is λ_{LSP}, then the structure is resonant for this wavelength, if the length of the structure is approximately $L = \frac{n}{2}\lambda_{LSP}$, where n is any integer number. In this case, the LSP is referred to as a localized surface plasmon resonance (LSPR). At the resonance wavelength, the nanoantenna can couple to the light more strongly, enhancing the local field strength further. If the device is asymmetrically shaped, e.g. like a rod instead of a sphere, the device can become resonant for one specific polarization of light. A wide variety of shapes exists, but in each of the antennas, light is coupled and converted into LSPRs, which induce strong locally oscillating electromagnetic fields.

An example of an application of such antennas includes Surface Enhanced Raman Spectroscopy (SERS), in which resonant nanoantennas (e.g. gold nanoshells) enhance the local field strength dramatically, enhancing the Raman signal. Furthermore, such antennas could be used to focus light beyond the diffraction limit, which can increase the resolution of imaging.

For solar rectification, nanoantennas are interesting, if not crucial, due to the fact that they can induce very strong locally oscillating electric fields, which could drive electrons inside a circuit to move back and forth. If connected to a geometric diode, as introduced previously, it can then be used to rectify sunlight.

The concept becomes even more interesting when considering that recent research has indicated that surface plasmons can be supported in graphene [43, 44], meaning that graphene could be patterned to work as an antenna. The research also indicates that the ratio of plasmon to free space light wavelength (or confinement ratio) in graphene is given as [43]

$$\frac{\lambda_{LSP}}{\lambda_0} \approx \left[\frac{4\alpha}{(\epsilon+1)}\right]\left(\frac{E_F}{\hbar\omega}\right), \tag{1.7}$$

24

where λ_0 is the free space light wavelength, $\alpha \equiv e^2/\hbar c \approx 1/137$ is the so-called fine-structure constant of graphene, ϵ is the dielectric constant of the substrate on which the graphene lies, E_F is the Fermi energy of the graphene and $\hbar\omega$ is the photon energy of the light incident on the graphene. This equation is valid under the assumption that $E_F > \omega$. Assuming then, that the graphene is free standing ($\epsilon \approx 1$ in air), and that E_F is chosen to be the same as $\hbar\omega$ (e.g. $\hbar\omega \approx 0.117 eV$ for 10.6 μm light, which can be achieved chemically by doping the graphene, or by applying an electric field across the graphene), $\lambda_{SP}/\lambda_0 \approx 2\alpha \approx 2/137$. This means that the plasmon wavelength is approximately 68 times smaller than the free space light wavelength. In this case, to make a structure that is resonant for a certain wavelength of light, the length of the structure should be chosen to be

$$L \approx \frac{n}{2} \frac{\lambda_0}{68}. \tag{1.8}$$

This result shows that, for example, to make the nanoantenna resonant in first order mode (n = 1) for 10.6 μm light, the nanoantenna would have to have a length of L = 77.4 nm, provided that the antenna is free standing, and the graphene is doped (or a bias voltage is applied) such that $E_F = 0.117$ eV. This result also shows an inherent difficulty in using graphene as a nanoantenna material. The antennas will usually not be free standing, and will instead lie on a substrate, e.g. SiO_2, which has a dielectric constant $\epsilon \approx 3.9$. This further increases the confinement ratio, meaning even smaller antennas need to be made. Other materials such as gold do not have such extreme confinement ratio, meaning larger antennas can be made that are still resonant for the same wavelength. As shown in Fig. 1.11, the solar spectrum reaches a maximum intensity around 500 nm, which would require graphene nanoantennas of around 3 nm in length. With current fabrication techniques, this is likely too challenging. Fortunately, however, the spectrum of sunlight is reasonably broad and even at longer wavelengths still contains reasonable intensities, meaning graphene nanoantennas could still be a viable option.

1.6 Creating diodes and antennas from graphene

The previous sections have now shown that graphene can be patterned to produce an asymmetric I(V) response, i.e. it could work as a diode, even for optical frequencies. Additionally, research suggests that graphene might also be used to create optical antennas. This opens up the possibility of making rectennas using only graphene. This has the advantage that only a single fabrication step is needed to create the devices. Once graphene can be patterned, creating a diode or an antenna is a simple matter of shaping the graphene differently.

The final device could work in multiple ways. For example, separate antennas and diodes can be created, so that multiple antennas feed current to a single diode. This has the advantage that both the antenna design and diode designs can be optimized separately. It does potentially increase the difficulty in fabricating such devices, since networks of antennas and diodes need to be made. On the other hand, a single structure could also be created that acts both as an antenna and as a diode, such as illustrated in Fig. 1.15. In this design, multiple antennas are placed in a row, forming so-called optical ratchets. Each antenna is a triangular shape, which resembles single-sided bow-tie antennas. LSPRs will propagate along the surface of the graphene in each antenna, inducing strongly oscillating electric fields across the restriction, which can then theoretically move electrons around the restriction back and forth. Because the restriction is asymmetric, i.e. shaped like a geometric diode, electrons will more easily move in one direction than in the other. In that way, adding more antennas can enhance the overall output. As with all designs, the amount of antennas is limited to the spatial coherence of the sunlight, because otherwise the antennas will work out of phase, reducing the efficiency.
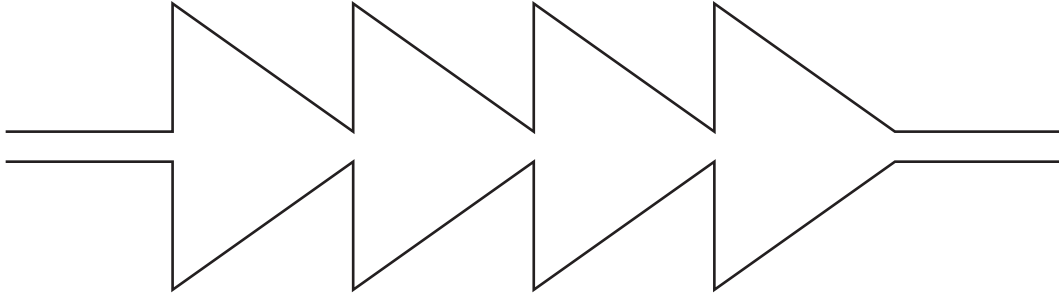
Figure 1.15: Concept for graphene rectennas, or optical ratchets. The triangular shapes are imagined to work like antennas and resemble single-sided bow-tie antennas. Each antenna will then induce strong LSPRs. Across the intersection, the fields between two antennas will shake electrons back and forth, and due to the asymmetric restriction, electrons are expected to be able to move easier in one direction than the other.

This chapter has now discussed the theory needed to understand the concepts behind optical rectification. A diode has been shown to work at IR frequencies, and antennas could be made to produce oscillating electric fields that drive the current. In the next chapter, the simulations that were performed to help optimize the diode design will be presented.

Chapter 2

Simulations

The performance of rectennas depends on many different factors. For example, antenna performance determines how much of the sunlight, incident on it, is coupled, i.e. transformed into electric energy. Furthermore, in the case of nanoantennas, each antenna has a limited area, meaning only a part of all light is incident on it, and unless complex designs are used, most antennas are only effective for specific frequency ranges. In the case of geometric diodes, the performance is determined in part by the asymmetry of the forward and backward current. Deviation from the ideal diode behavior introduces losses. These are just some of the factors, but all factors combined determine the total efficiency of solar rectification using rectennas.

Such problems are best tackled one step at a time. For this research, a start was made with the development of a simulation model for geometric diodes, to help understand the influence of and optimize the shape of the diode. The next section will discuss how the diode shape model works and will show simulation results.

2.1 Diode shape simulations

Model theory & implementation

As discussed in Chapter 1, geometric diodes are based on the assumption that, in the material, electrons move ballistically over distances larger than an asymmetric constriction. Furthermore, the electrons are assumed to reflect off the edges or borders of the material so that the geometry of the device has a significant impact on electron motion. To simulate this behavior, a Monte Carlo simulation model was developed based on the Drude model for electron movement [45, 46, 24]. In this simulation model, the following assumptions are made:

1. Electrons are the majority charge carriers in the graphene, i.e. they determine conduction;

2. There is no electron-electron or electron-ion interaction;

3. Electrons move with a constant total velocity $\vec{v}_{tot} = \vec{v}_F + \vec{v}_{ext}$, where $\vec{v}_F$ is a randomly oriented Fermi velocity ($\approx 10 \times 10^6$ m/s) and $\vec{v}_{ext}$ is a velocity due to external forces (e.g. a drift velocity due to an externally applied electric field);

4. Accelerations are neglected for simplified computation;

5. Electrons travel over a distance MFPL after which they collide or scatter;

6. At the edges, electrons reflect specularly, i.e. $\phi_{in} = \phi_{out}$.
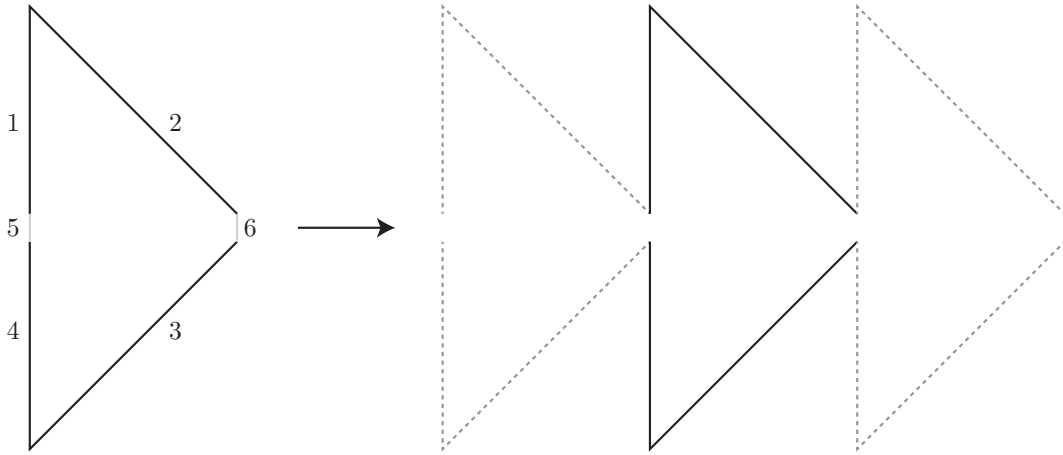
Figure 2.1: Illustration showing an example of a geometric diode shape defined as line segments. The black lines (1-4) are the borders or edges of the graphene. The grey lines (5 and 6) are periodic boundary conditions. The effective structure then looks like an infinite ratchet structure as illustrated on the right.

The first assumption states that there must be more electrons contributing to the conduction than holes. If holes and electrons are symmetric in electronic properties and in equal amounts (which is the case if the Fermi level is exactly at the Dirac point, see section 1.4), then both the electrons and holes experience the same geometric shape of the diode, and will experience the same preferential direction of movement. This naturally results in a net current equal to zero, regardless of diode geometry. By chemically doping the graphene or by applied a gating voltage, the Fermi level can be adjusted so that electrons form the majority charge carriers. Note that it is also possible to make the holes the majority charge carriers, and this should have a similar effect.

It is assumed that electrons can move ballistically, where the electrons are assumed to have no interaction with the carbon atoms in the graphene lattice or with other electrons. The electrons are instead assumed to move in a straight line, over a distance equal to the MFPL, until they collide. After each collision, the electrons are assumed to have an instantaneous randomly directed Fermi velocity $\vec{v}_F$. An external electric field can be applied, which adds a constant velocity term $\vec{v}_{ext}$, e.g. a drift velocity. The drift velocity is determined by equation 1.1, which can be rewritten to read $\vec{v}_D = \mu\vec{E}$. The magnitude of the electric field is determined as $E = V_{bias}/w_{diode}$ where w_{diode} is the width of the over which the bias is applied. For example, 10 mV applied over a 250 nm long diode yields an electric field magnitude of 40 kV/m. With an electron mobility of 4000 $cm^2V^{-1}s^{-1}$, this then yields $\vec{v}_D = 1.6 \times 10^5$ m/s. This velocity is directed either in the forward or backward direction of the diode, and is added to the Fermi velocity to yield the electron's total velocity.

A further simplification has been made in the sense that the electrons are assumed to move with a constant velocity, meaning that acceleration is neglected. This assumption is reasonable when averaged over a large number of collisions. Additionally, it greatly simplifies and speeds up the simulation. The model could be expanded later on to include such acceleration. Finally, the electrons will reflect off the edges of the graphene, where it is assumed that this happens specularly.

The geometric diode shape can be defined as an array of line segments that define the edges of the graphene. For example, see Fig. 2.1. The solid black lines 1-4 represent the border of the graphene, and the grey lines 5 and 6 represent periodic boundary conditions. In this way, theoretically, any geometric diode shape can be defined, meaning that this model could be used to determine an optimal shape for diode performance.

The simulation can be described to work as follows:

1. An electron starts out at a random position inside the geometric diode;

2. The velocity of the electron is determined as the sum of a randomly oriented Fermi velocity and a drift velocity due to an externally applied electric field;

3. The electron trajectory is calculated. The electron is assumed to move a total distance equal to the MFPL, in a straight line. If this path intersects an edge, the trajectory is reflected specularly around that edge. Step 3 is repeated until the path does not intersect any edge, i.e. the electron is now positioned inside the diode.

4. If the electron crosses a periodic boundary, the electron is teleported to the other side and the electron continues in the same direction. If the electron passes through a periodic boundary to the right, this counts as +1 for the electron flux. If the electron passes through the periodic boundary to the left, this counts as -1 for the electron flux.

5. The algorithm continues at step 2, until enough collisions have occurred for the electron flux to reach a stable value (or equivalently: the same amount of MFPL distances were covered by the electron).

The processes are illustrated schematically in Fig. 2.2.

The number of times that the electron crosses the periodic boundaries (the grey lines in Fig. 2.1) determines the total electron flux[1]. The flux is defined such that an electron passing to the right counts as +1, while an electron passing to the left counts as -1. The simulation is run, until the electron flux reaches a stable value. At this point, the current through the diode can be calculated. Each time the electron moves between collisions, it does so with a certain velocity, $\vec{v}_{tot}$ (which varies) over a certain distance (which is always equal to the MFPL). This means that a time $t = v_{tot}/d_{MFPL}$ passes between each collision. The total amount of time that has passed can be calculated by summing all of these times. Since the electron flux and the time passed are known, the current flowing through the diode can then be calculated.

The simulation was written such that a range of bias voltages could be defined for which the simulation would be run. For example, a range from -0.1 to 0.1 V in 9 steps could be defined so that the current through the diode could be plotted versus bias voltage.

Simulations and results

The simulation model was implemented in MATLAB to test the functionality and performance. The first result for a few collisions is shown in Fig. 2.3. A diode with a neck width of 50 nm, a shoulder width of 500 nm and a length of 500 nm was simulated. The MFPL was chosen to be 200 nm. The electron started out at the green circle, scattered several times at the red circles and crossed the periodic boundary to the left, to end up at the blue circle. Fig. 2.3 shows that the simulation model works as expected. The electron flux was counted as -1 electrons, indicating the current was flowing backward.

As a next step, it was analyzed after how many collisions the electron flux or current would stabilize. This result is shown in Fig. 2.4. As can be seen, the electron flux converges to a single value, and the error in the current converges as well. From this simulation, acceptable results are achieved when simulating for 10^6 or more collisions. At 10^6 collisions, the error is 9.3%, and at 10^7 collisions the error has reduced further to 3.1%. It is important to note that although increasing the number of collisions increases the accuracy, it also increases computation time drastically. An acceptable compromise was found at around 10^6

---

[1]Note that with flux, it is meant here how many electrons pass the boundary. The area of the boundaries is not relevant in this case.
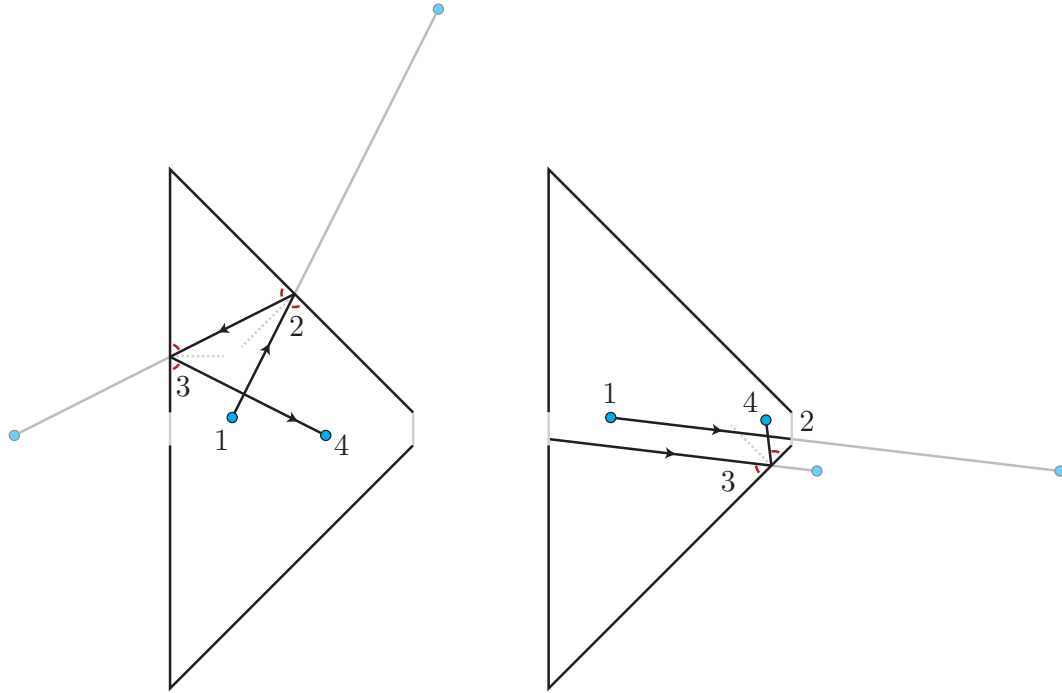
Figure 2.2: Illustration showing the steps in the simulation model. (left) The electron is given a total velocity ($\vec{v}_{tot} = \vec{v}_F + \vec{v}_{ext}$) in some direction at point 1. The next position is calculated as if there were no boundaries (shown as a gray line from point 1 through point 2. It is then checked if the line intersects the boundaries, and if so, is reflected specularly around the edge closest to point 1. The process is repeated at point 3, until the electron position lies inside the diode (e.g. in this case at point 4). At this point, the process would be repeated until a set number of collisions have occurred. (right) The same procedure, except this time the electron passes through one of the periodic boundaries at point 2. In that case, the electron is teleported to the other periodic boundary, after which the same process as before is repeated, until the electron is once again inside the diode and not hitting any borders. In this case, the electron would have contributed +1 to the total electron flux, since it passed the periodic boundary on the right.
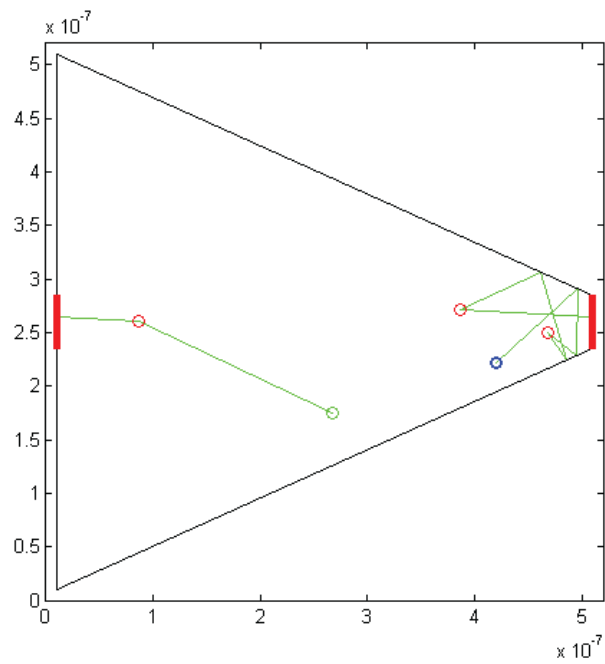
Figure 2.3: Example of a simulation run in MATLAB with the output visualized. In the simulation, a structure 500 nm wide and 500 nm tall was simulated. The electron started out at the green circle, then 'scattered' at the red circle and crossed through a periodic boundary condition, after which it scattered twice and ended up at the blue circle. This simulation counted -1 as the electron flux.
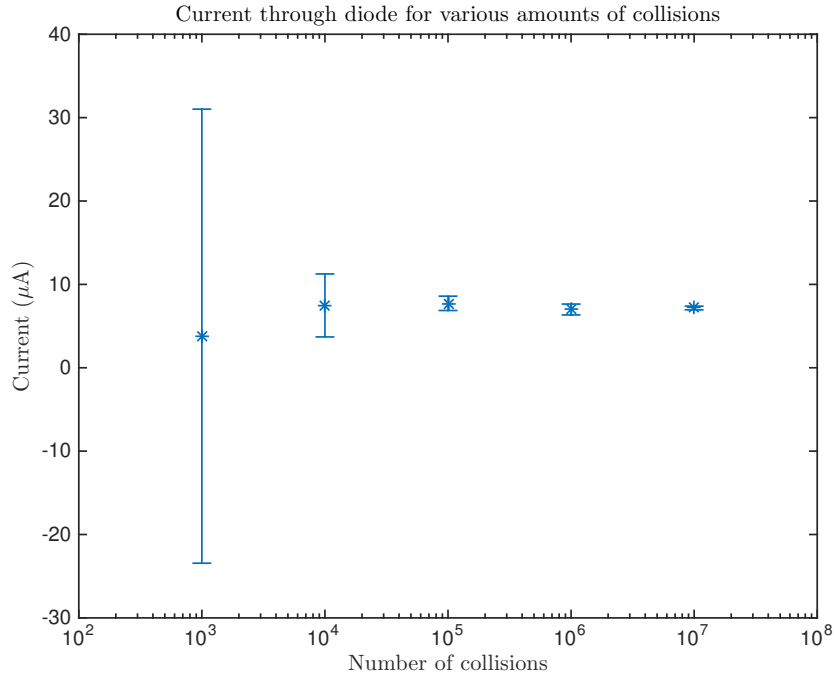
Figure 2.4: Result of simulations for different amount of collisions. A diode with a neck of 50 nm, a shoulder width of 1 μm and a length of 500 nm, with a bias voltage $V_{bias} = 10$ mV is simulated for different numbers of collisions. The result clearly shows that the current converges for an increasing number of collisions. At 10^6 collisions, the result has stabilized well enough for the simulation results.

collisions. The code was first optimized to work using parallel for-loops in MATLAB (using *parfor*). This greatly sped up the simulation (depending on the number of CPU cores in the computer). The code was later ported to Java for further improved performance.

Now that the number of collisions needed to get stable results was known, it was possible to start varying the bias voltage and the structure of the diode, to investigate the effects of such parameters on diode performance. First, the bias voltage was varied to see if any non-linear behavior occurs. To that end, the same structure as before (50 nm neck, 1 μm shoulder and a length of 500 nm) was used, and the voltage was varied from $-V_{max}$ to $+V_{max}$ in 20 equidistant steps. If a device is linear, there should be no asymmetry between the forward and backward current at equal but opposite bias voltages. The results of the simulation are shown in Fig. 2.5.

The simulations show that for lower bias voltages ($\pm$ 10 mV), the behavior is almost linear. A second order polynomial fit was applied, but the differences between forward and backward flowing current is very small. At a bias voltage of $\pm$ 100 mV, the behavior clearly changes and becomes visibly nonlinear. Again, a second order polynomial has been fit to the simulation data. At even higher bias voltages, an interesting behavior is seen, where it appears that the diode has two distinct linear responses, depending on the sign of the bias voltage and thus the direction of the current. This can be partially explained in the following way. At a bias voltage of 1 V, the drift velocity is 8×10^6 m/s. This is a factor 8 times larger than the Fermi velocity, meaning that the direction of the electrons is close to parallel to the electric field. As the voltage is ramped up further, the electrons will become more and more parallel to the electric field. In the forward direction, this means that electrons will be more likely to pass through the right periodic boundary as they are 'guided' by the funnel

shape. In the backward direction, there is no such funnel and, although as the field strength is increased, the electrons are more likely to pass through, this process is much slower. The result also clearly shows that if no bias is applied, the current has no preferential direction and the device will not yield energy.

Next, the neck width of the diode was varied, while keeping the shoulder 1 μm, the width 500 nm, and the MFPL 200 nm. The result is shown in Fig. 2.6, where both the current flowing through the diode for applied bias voltages, and the asymmetry between the forward and backward flowing currents, calculated as I(+V)/I(-V), are shown. As the neck width increases, the magnitude of the current also increases. This is to be expected, as electrons can then more easily flow through the diode. Any obstruction will lead to an increase in resistance, and increasing the neck width is equivalent to reducing the size of the obstruction. The asymmetry does not follow the same simple trend, however. The asymmetry starts to increase as the neck width is decreased. However, below a certain neck width, the asymmetry first starts to increase as the bias voltage increases but then decreases again. This can be understood by realizing that, for the dimensions chosen for the diode, the slopes have an angle very close to 45 degrees. As the electric field strength is increased, the electrons start to move almost parallel to the electric field. In addition, shrinking the neck width brings the slope of the diode even closer to 45 degrees. If the electrons move exactly parallel to the electric field, and the slope is exactly 45 degrees, it is no surprise that electrons start to reflect off the slopes at 90 degree angles, never making it through the diode. This then explains that at higher bias voltages, and at smaller neck sizes, this effect becomes more and more pronounced.

As a last simulation, the shoulder width of the diodes was varied, while the neck width was 50 nm, the width was 500 nm and the MFPL was 200 nm. The result of this simulation is shown in Fig. 2.7. This again shows a similar trend as with the neck width. Increasing the shoulder width from a small amount initially results in an increased current flowing through the diode, and an increased asymmetry. However, above a certain shoulder width, both the current and the asymmetry change. Taking the previous explanation into consideration, it can be seen that this is essentially the same effect as before. With a shoulder width below 1 micrometer, the angle is less than 45 degrees, so the electrons are more likely to pass through as the bias voltage increases. At a shoulder width equal to 1 micrometer, the angle is very close to 45 degrees, and the effect occurs again.

Discussions about the simulation model

As shown above, the simulation model seems to predict at least the basic behavior of the geometric diode and shows that the diode indeed has a nonlinear response. It is however important to note that the simulation model described in this chapter is an initial attempt at creating a simulation model to determine the effects of the shape of the geometric diode. Assumptions were made that yield inaccurate results and, as a result, there is still room for improvement. This section will treat some of the most important limitations of the simulation model.

Perhaps the most important limitation of the model is that it becomes less and less accurate, the larger the applied bias voltage is. This can be understood by realizing that in the current implementation, only constant velocities are taken into consideration between collisions. As the applied bias voltage, and thus electric field strength increases, so too will its effect increase, affecting the trajectory of the electrons significantly, even during collisions. The model is valid, as long as $v_D \ll v_F$. In that case, the drift velocity will not have a significant impact on electron motion. However, if $V_{bias} = 1$ V, for example, then $v_D = 8 \times 10^6$ m/s, which is greater than the Fermi velocity. In this case, electrons could even reflect completely backward if reflected specularly (depending on the geometry), since for reflections the drift velocity is ignored. The model will therefore yield inaccurate

results. Even at 10 mV, $v_D \approx 8 \times 10^4$ m/s, and is thus approximately 8% of the Fermi velocity. It is therefore important that acceleration of the electrons is taken into consideration. To implement this in the model, one might consider calculating an electron trajectory including acceleration, instead of calculating a straight line. Then as the electron reflects off boundaries, the reflection can be done specularly, but the path should be recalculated.

There is also the question of whether or not it is valid to assume that the electron travels a distance equal to the MFPL before 'colliding', while reflections do not count as such collision events. A reflection *is* in essence a collision event, so it can also be said that the electron starts traveling anew. Furthermore, in this model, electron-electron and electron-ion interactions are ignored. In reality, electrons will feel the presence of other electrons, especially at the edge of the material. This may affect the trajectory of such electrons. It may be worth investigating how much of an impact this might have. In the current simulation model, a single electron is simulated to 'collide' a sufficient number of times for the electron flux, or current, to reach a stable value. Periodic boundary conditions are introduced to ensure that the electron stays inside the diode. This is a limitation because it effectively means that only periodic structures can be modeled.

Lastly, as the diode size decreases, quantum effects will play a more significant role. At the atomic level, the edge of the graphene may have an impact on the reflection characteristics of the electron. Graphene can form two types of edges: armchair and zigzag. If the graphene is not cleanly cut, then any combination of the two types of edges can follow after one another. It can be imagined that the edges have an effect on the type of reflection that occurs. If the cut is not 'clean', then the electrons may scatter more off the edges than they reflect specularly. It would be interesting to simulate this as well.

In conclusion, a simulation model has been made that shows expected behavior. Although the model is basic, it can help understand geometric diode designs. With more features, the model could be used to compare experimental results with actual measurements of diodes.
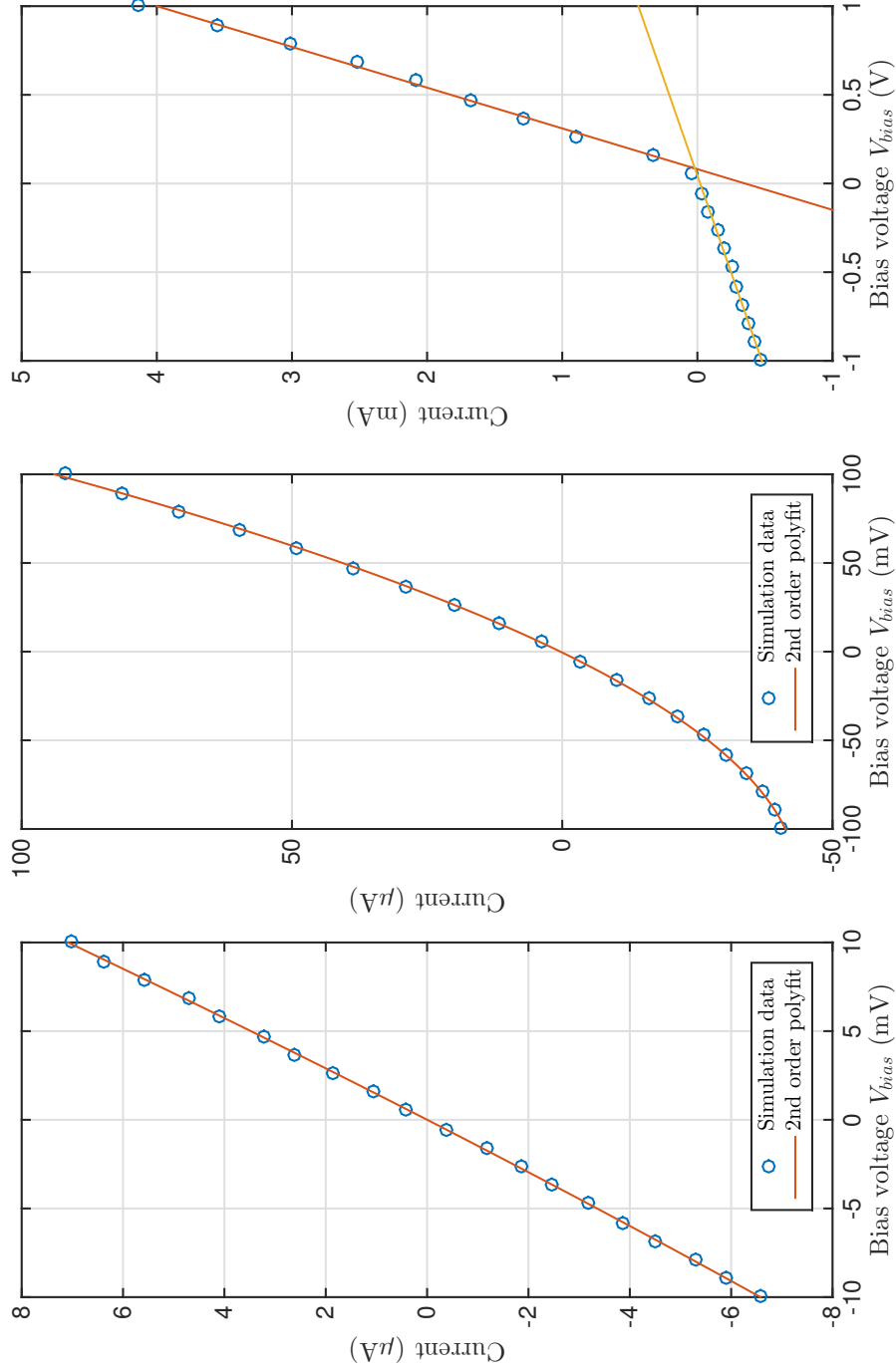
Figure 2.5: Simulation results for varying bias voltages. The bias voltages were varied between (left) ± 10 mV, (middle) ± 100 mV and (right) ± 1 V. In the 1 V case, two linear fits were applied. In the 10 mV and 100 mV cases, a 2nd order polynomial fit was applied to the two clearly different sections.
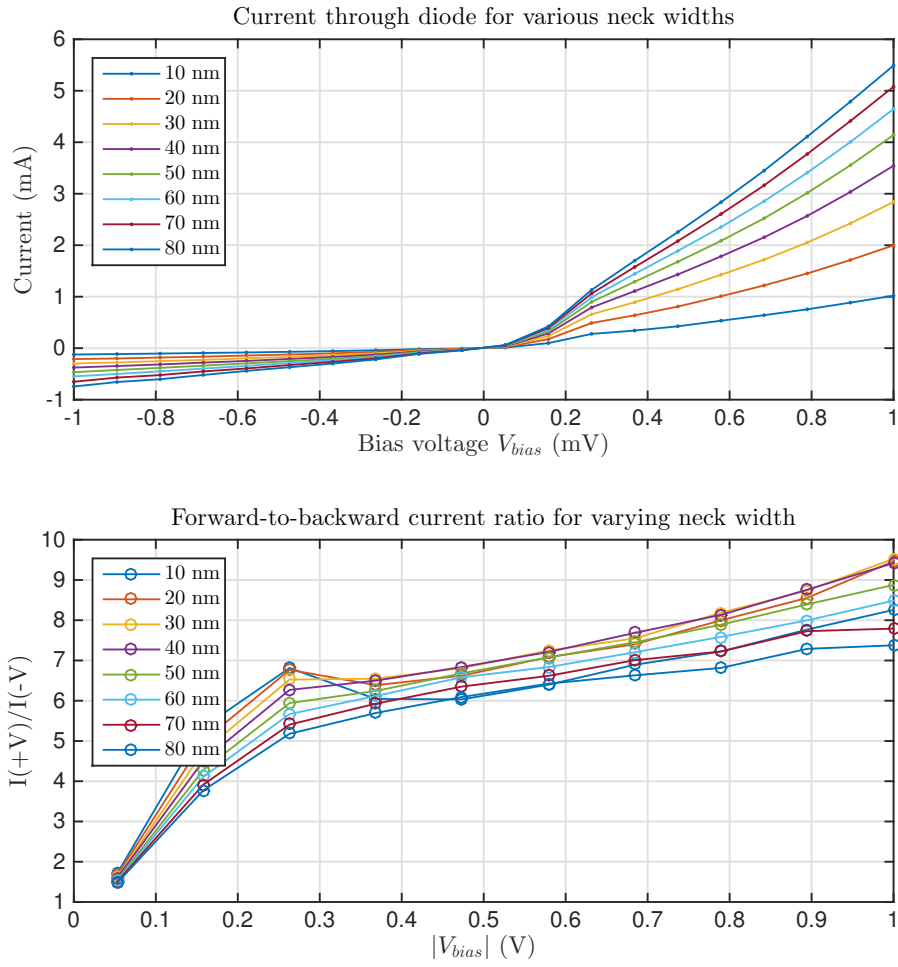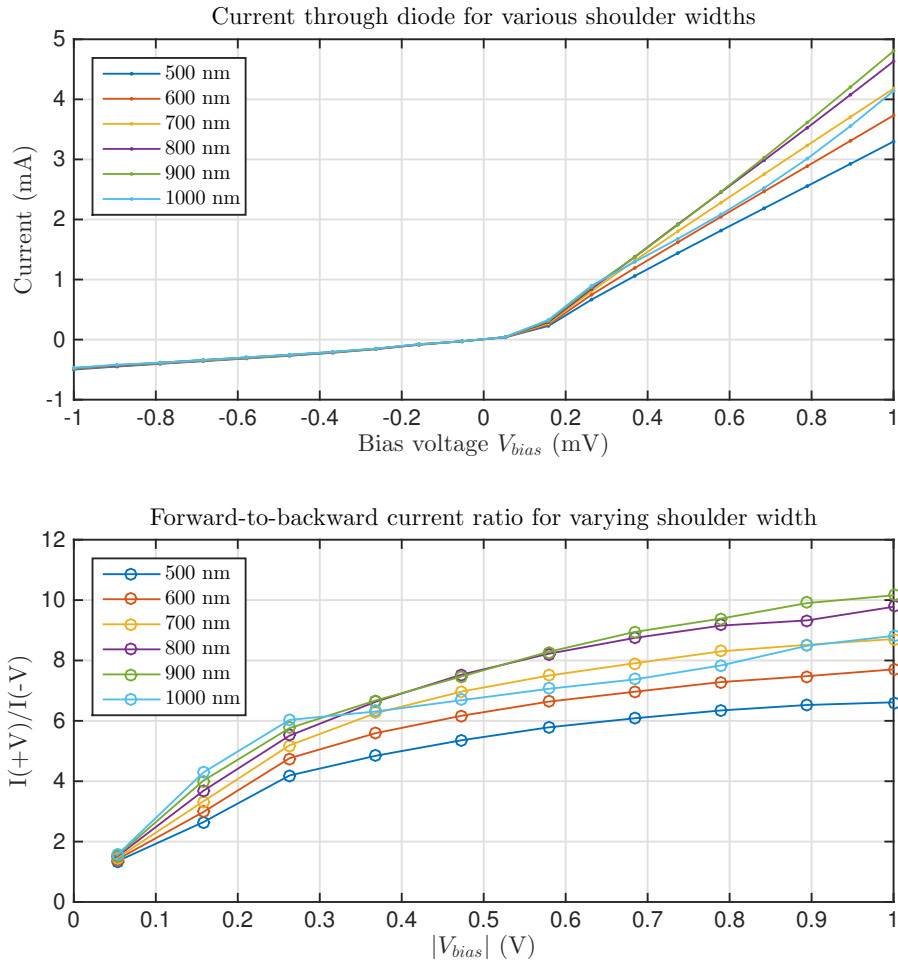
Figure 2.6: Simulation results for varying neck width. (top) The current flowing through the diode for an applied bias voltage. (bottom) The asymmetry of the forward and backward flowing current, calculated as I(+V)/I(-V).

Figure 2.7: Simulation results for varying shoulder widths. (top) The current flowing through the diode for an applied bias voltage. (bottom) The asymmetry of the forward and backward flowing current, calculated as I(+V)/I(-V).

Chapter 3

Materials and methods

We now have a simulation model that allow us to predict the diode behavior based on the shape of device. The next step is to fabricate actual samples to test the model and to see if we can actually make diodes. This chapter provides brief background information about the most important materials and methods used for the characterization, fabrication and measurement of these geometric diodes. The next chapter will explain how these methods can be combined to come to a final fabrication process.

3.1 Graphene

The graphene used here was acquired from Graphenea[1]. This graphene is produced by chemical vapor deposition (CVD) on copper substrates. Samples can be ordered on various substrates, including the Si/SiO_2 used here. The graphene is then transferred via a wet transfer process to a Si/SiO_2 substrate. The graphene is specified as having an electron mobility of 4000 $cm^2V^{-1}s^{-1}$, a sheet resistance of $450 \pm 40\Omega/\square$. The maximum grain size of the graphene, i.e. the size of the regions of graphene that were grown in the same orientation, is 10 μm. The Si/SiO_2 substrates are 10 by 10 mm, and are about 525 μm thick. The SiO_2 layer is 300 nm ($\pm$ 5%) thick. The full specifications have been included in appendix A. An additional sample of graphene was also generously donated by Applied Nanolayers. In this sample, the graphene was grown on a 2-inch sapphire substrate with copper on top.

3.2 Confocal Raman Spectroscopy

Raman spectroscopy is a spectroscopic method that was used to characterize the graphene before and during fabrication. It is a non-intrusive characterization method which does not require sample preparation. In Raman spectroscopy, monochromatic light, e.g. a laser, is incident on a sample of interest, say a molecule. This molecule can have many different vibrational resonances, which can be measured using Raman spectroscopy. If the energy of the photon incident on the molecule does not match any of the electronic or vibrational energy states of the molecule, the molecule can be promoted to a virtual energy state, as illustrated in Fig. 3.1. Once in the virtual energy state, the molecule is by far most likely to relax back into the ground state, after which the photon is re-emitted. This is called Rayleigh scattering. However, there is also a very small chance that the molecule does not relax back to the same vibrational energy level, but instead relaxes to a different vibrational energy level. The photon can then either lose (Stokes) or gain (Anti-stokes) energy. By analyzing the energy level or frequency of the photons that scatter from the
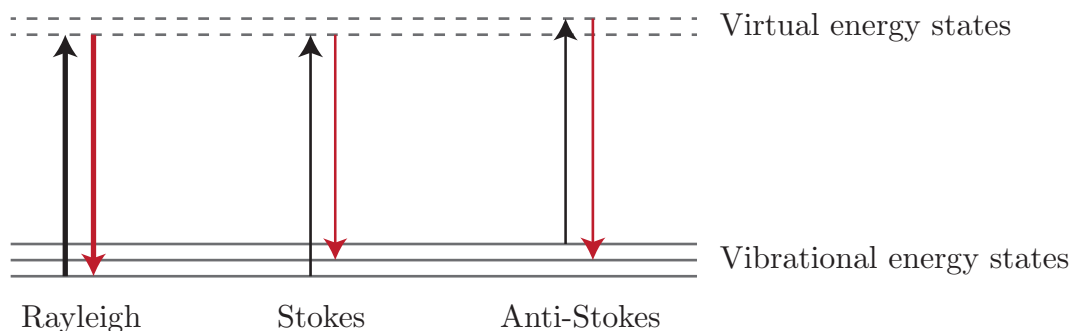
---

[1]www.graphenea.com

Figure 3.1: Illustration showing the Raman process. The assumption is made that monochromatic light is incident on a molecule, where the photon energy does not match any of the electronic or vibrational energy states of the molecule. An absorbed photon can then promote the molecule to a virtual energy state, after which is it most likely to relax back to the ground state. Once every few excitations, it will however relax back to a higher or a lower vibrational energy state, meaning the re-emitted photon either loses or gains energy on the original photon, respectively.

material, a Raman spectrum can be measured, which will yield peaks at those energy levels corresponding to certain vibrational states. This is naturally characteristic of the molecules being analyzed. This technique can thus be used to identify which molecules are present, including graphene.

Two different Raman setups were used in this research project. Both of the setups involved confocal Raman spectroscopy setups. The first setup was found in the Medical Cell BioPhysics group at the University of Twente. It features a 647.1 nm krypton laser as an excitation beam. The second setup was found in the BioNanoLab, also at the University of Twente. In this setup, a 633 nm laser was used as an excitation source. Both setups were able to measure Raman spectra at individual locations, as well as making image scans. In image scans, Raman spectra are taken in a grid of e.g. 64 by 64 points, producing a 64x64 pixel image of a region of 30 μm^2 or more.

3.3 Scanning Electron Microscope and Focused Ion Beam

To pattern the graphene into various shapes, a FEI Nova 600 Nanolab Dualbeam SEM/FIB system was used. This device features both a Scanning Electron Microscope (SEM) and a Focused Ion Beam (FIB) module.

In an SEM, the sample of interest can be placed in a vacuum chamber, after which it is scanned with a beam of electrons that are accelerated towards the sample. These electrons will interact with the atoms in the sample, e.g. exciting them. Different processes can then take place, such as backscattering of the electrons, emission of secondary electrons, and light generation. These signals can be used to either image or characterize the sample of interest. In this research project, the SEM was used to make high resolution images of the surface of the graphene. The SEM is capable of reaching resolutions on the order of a nanometer.

The FIB on the other hand, uses gallium ions, which are accelerated to the sample in a beam of ions (hence then name). These ions are much heavier than electrons. Although this technique can be used for creating images as well, it is used in this research process as a machining tool. Accelerating the ions fast enough gives them sufficient energy to etch away the graphene where needed. The maximum reported resolution of this FIB is 7 nm. Because of the high energy of the ions, the FIB cannot be used for imaging, as will be illustrated in the next chapter.
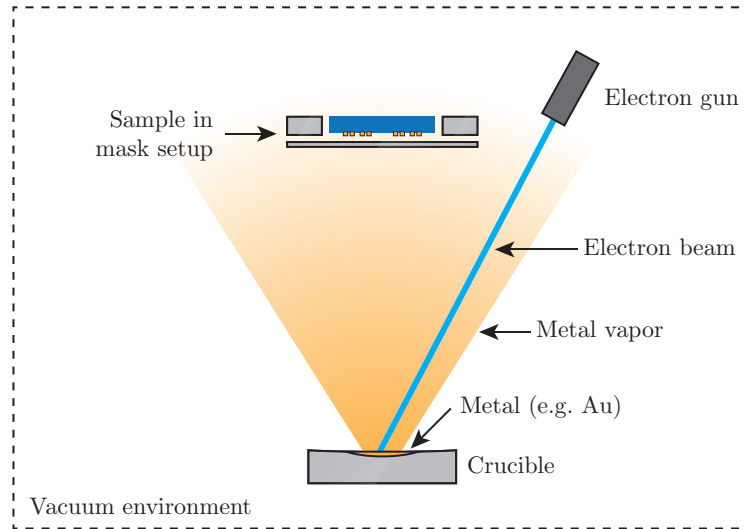
Figure 3.2: Illustration showing the working of thermal vapor deposition using a Balzers BAK 600.

3.4 Thermal vapor deposition or BAK 600

To perform electrical measurements, electrical contacts need to be deposited on the graphene samples, as will be explained in section 4.1. To deposit these electrical contacts, a Balzers BAK 600 Ion Beam Evaporator is used. The setup is briefly illustrated in Fig. 3.2. In this device, a crucible containing a metal is placed in the bottom of the device. The sample is placed on a turning wheel at the top of the device. This sample is encased in a mask setup, which will be explained in section 4.1. This mask ensures that metal is only deposited on certain regions of the sample. The entire system is then pulled to vacuum, after which an electron gun is turned on, which will heat up the metal inside the crucible. Because of this heating, ions from the metal will be ejected and a 'metal vapor' is produced. This vapor is then incident on the mask, after which a layer of metal can be grown on the sample. By controlling the heating rate and the time, the thickness of the layer can be controlled. In this research project, both gold and palladium contacts were grown on graphene.

3.5 Probe station

Electrical measurements were performed using a probe station. In a probe station, four (or sometimes more) thin metal probes can be placed directly on the sample or on electrical contacts, as shown in Fig. 3.3, after which a current can be sent through the device or a voltage can be applied across it. In other words, an I(V) response of the device can be measured. An example of a probe station is shown in Fig. 3.4. In this probe station, four needles can be seen, that have tips which are smaller than 100 μm in diameter. The tips can be moved with micrometer resolution using translation stages. This way, the probes can be accurately positioned on the sample. A white light camera is present to see where the probes are in relation to the sample. Probes are connected in pairs of two, to voltage or current sources. Using a software program, the voltage or current output of the probes can be controlled, and can for example also be swept. This allows one to measure the I(V) characteristics of a sample. More about the probe station will be explained in section 4.1.

Two probe stations were used. The first probe station is illustrated in Fig. 3.4 and was made available by the NanoElectronics group at the University of Twente. The second
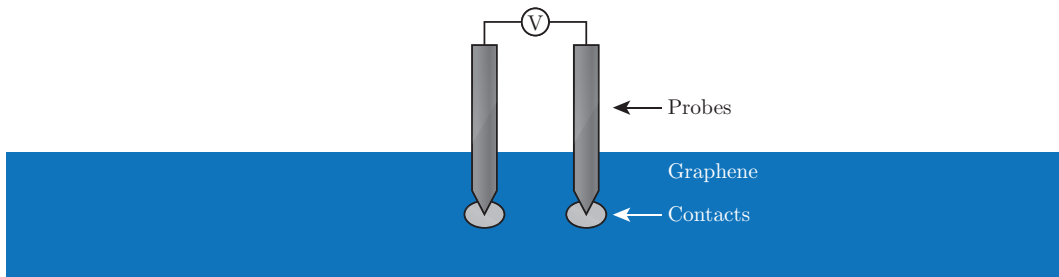
Figure 3.3: Illustration showing the workings of a probe station. This setup can be used to measure the I(V) response of a device, such as a geometric diode.
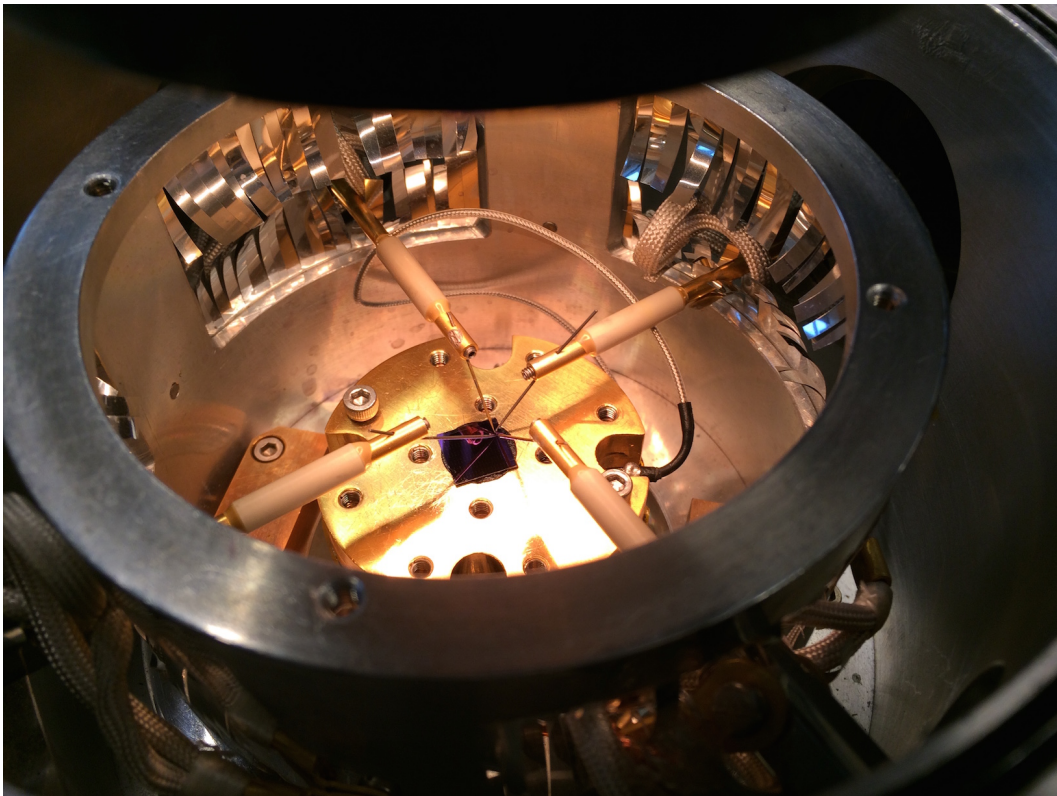

Figure 3.4: Photo of the graphene sample in the probe station. Four needles can be placed on the sample to test various samples.

probe station was made available by the Transducers Science and Technology group at the University of Twente.

Chapter 4

Fabrication results

The next step in the research involved the actual fabrication of geometric diodes. This chapter covers the different steps that were taken to pattern the graphene into the desired geometric shape. The chapter also describes how the graphene was prepared for electrical measurements using the probe station, by adding metal contact pads. Because of the limitations of using the FIB as a patterning technique, it turns out that it is best to start by preparing the sample for electrical measurements, before the graphene is patterned. As a result, the preparation for electrical measurements is discussed first.

4.1   Preparing for electrical measurements

Once the graphene is patterned, electrical measurements need to be performed to investigate whether or not the device works as intended. The probe station will thus be used to either apply a voltage across the diode or send a current through it. In any case, the probe station will use metal probes that need to be brought into contact with the graphene, as illustrated in Fig. 4.1. Here, a geometric diode shape is illustrated with a white outline, and a four-point probe configuration is used. In this configuration, a current is set to flow through the outer probes, and a voltage is measured across the middle probes. This technique has the advantage that the output signal does not contain any contact resistance. Theoretically, it is possible to place the probes from the probe station directly on the graphene to measure or apply electrical currents to the graphene samples. However, the probes have an ending diameter of roughly 100 μm, and are attached to long rods. As a result, the probes are rough and vibrate easily. Since graphene is only a single atomic layer of carbon, the probes can therefore easily damage the graphene devices. To prevent this from happening, metal contact pads were added on top of the graphene, which then act as a protective layer. Additionally, the contact pads may serve to improve the electrical contact with the probes, as the metal is expected to deform slightly to fit the shape of the probe. This is illustrated in Fig. 4.2.

To create the metal contact pads, the BAK 600 coating system was used to deposit a thin metal layer on top of the graphene in a specific pattern, e.g. as shown in Fig. 4.1. To create a four-point configuration, four individual contact pads need to be placed on the graphene device. To control where the metal is deposited and where not, a mask was designed. This mask is made of a thin sheet of e.g. steel, with holes cut out where the contact pads should be grown on the graphene. It covers the parts of the graphene where no metal should be deposited onto the graphene, and leaves holes where metal should be deposited onto the graphene.

It is desirable to be able to make many different geometric shapes in the graphene, e.g. to make several types of diodes, or perhaps in the future antennas. For that reason, a mask
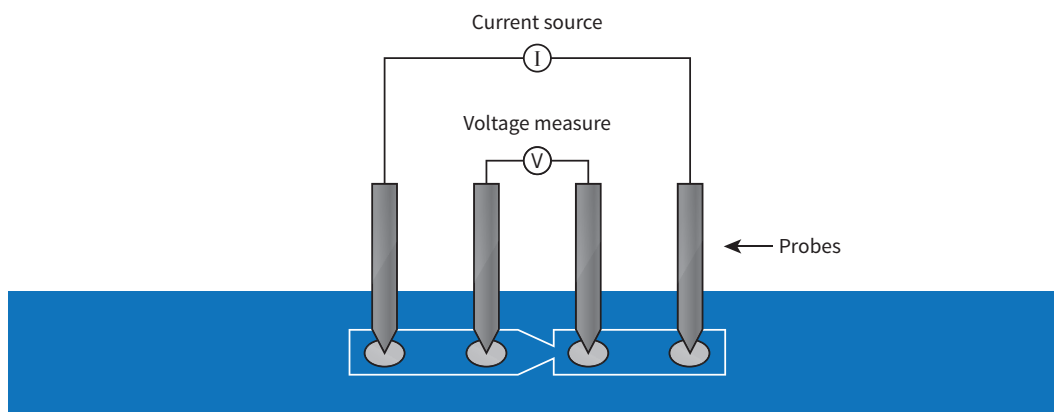
Figure 4.1: Illustration showing how the probes from the probe station would be placed on the graphene. A device (geometric diode) is illustrated by the white outline. Four probes from the probe station are placed in the four-point configuration on the graphene.
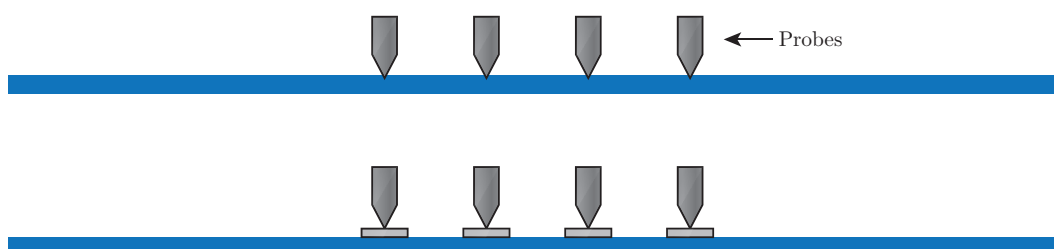

Figure 4.2: Illustration showing probes on exposed graphene versus probes on contact pads. The contact pads serve to not only protect the graphene, but may also improve electrical contact because the metal can deform to the shape of the probe.
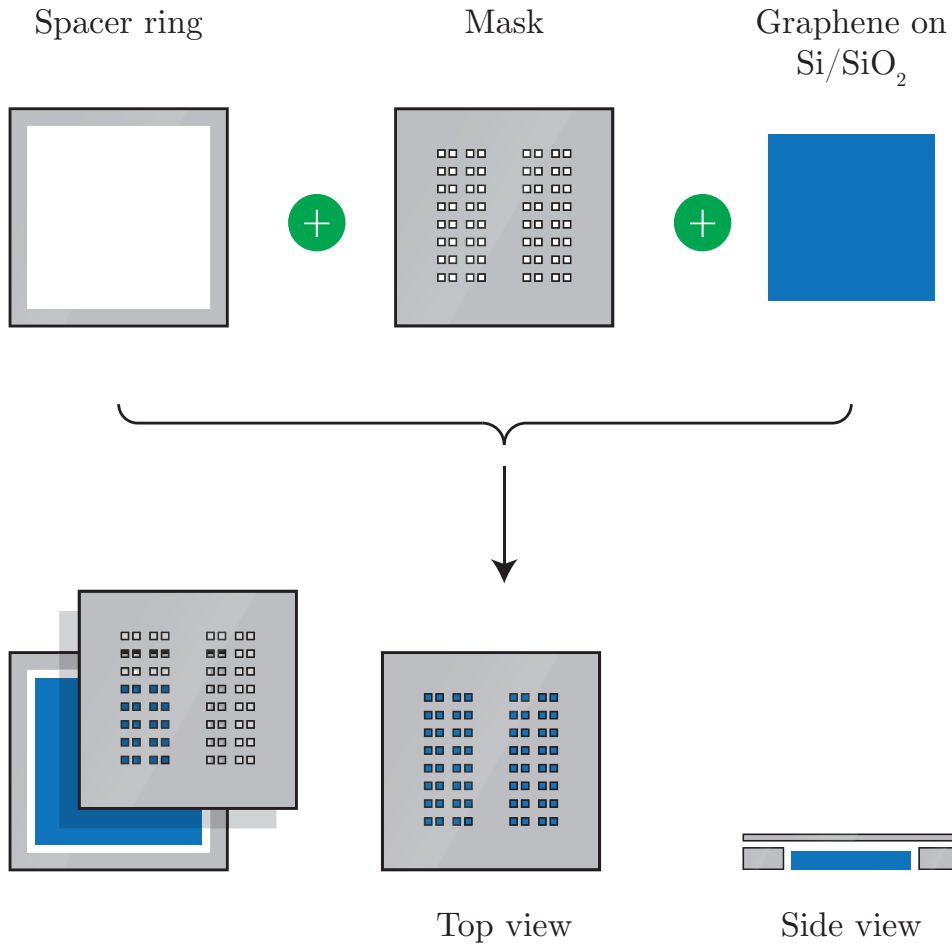
Figure 4.3: Illustration showing how the 'breadboard'-mask is assembled in preparation for deposition. (top) the three parts of the deposition mount is shown. It consists of a spacer ring, a mask and the graphene on Si/SiO_2 sample. (bottom) The sample is placed inside the spacer, after which the mask is placed on top. The mask and spacer are connected using adhesive tape. Because the spacer is slightly thicker than the sample (600 μm versus 525 $\pm$ 20 μm), a gap is left between the sample and the mask.

as illustrated in Fig. 4.3 was designed. In this design, many four-point configurations can be seen. In this way, effectively, a *graphene breadboard* is created. Four so-called contact pad shapes of each 100 by 100 μm are cut out of the mask. These pads are separated by 100 μm gaps, except for the middle two contact pads. Between the middle two contact pads, there is a gap of 200 μm. This middle gap is intentionally larger, as it then allows any kind of shape to be patterned later on with the FIB, which will be described later in this section.

The mask was constructed as illustrated in Fig. 4.3. At the top, it shows a 'donut'-shaped spacer ring, the mask and the graphene sample. At the bottom of the figure, the three parts are combined. The spacer ring serves to keep the mask suspended just above the graphene sample. Ideally, the mask would lie exactly on top of the graphene, as then the chance that the metal that will be deposited using the BAK spreads underneath the mask, covering more of the graphene than intended, is reduced. The closer the mask is to the surface of the graphene, the more defined the final contact pads will be. However, the same problem is present as with the probes from the probe station, in that laying the mask directly on top of the graphene will likely damage any graphene underneath due to
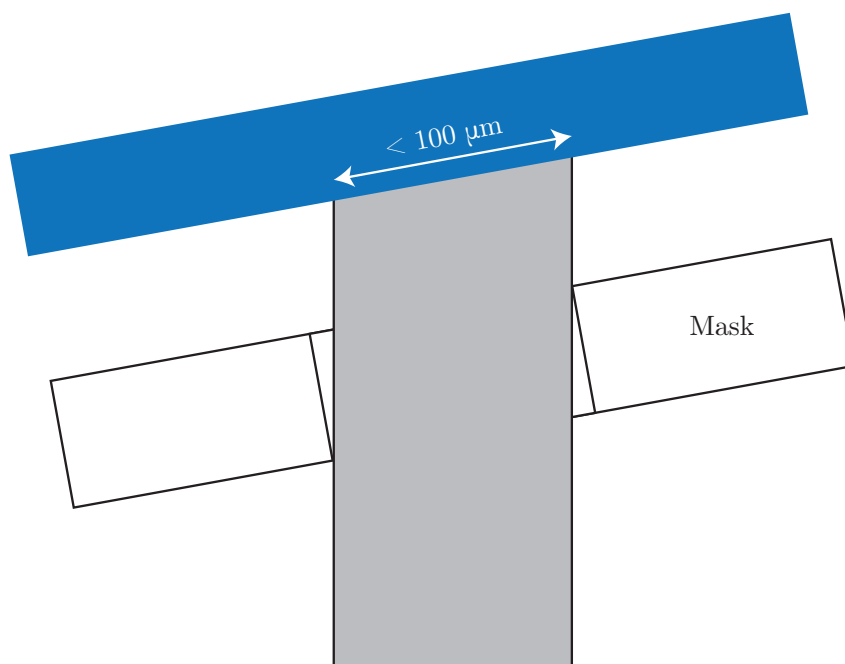
Vapor 'beam' from the crucible

Figure 4.4: Illustration showing the effect of the angle relative to the crucible on the side of the contact pads. A special mount was constructed to mount the sample at a 90 degree angle relative to the crucible.

e.g. hand movement. As a result, it was chosen to use the solution shown in the figure. The hole in the spacer ring was chosen to be slightly larger than the sample, to allow it to easily fit inside. The spacer ring has a thickness of 600 μm, and the sample has a thickness of 525 $\pm$ 20 μm (see A). This meant that a gap of about 50 to 70 μm was left between the mask and the sample. The mask itself is 100 μm thick.

Once the mask is made, the total assembly of spacer ring, sample and mask can be mounted on a special mount so that in the BAK 600, it is perpendicular to the crucible. The angle relative to the crucible is important, because otherwise the beam of vapor coming off the crucible will come in under an angle, which means that the contact pad will be smaller than intended. This is illustrated in Fig. 4.4. It therefore also helps to make the mask as thin as possible. The thinnest available material, 100 μm thick, was used in this case.

The mask was cut using a laser cutter. The laser cutter turned out to be at its limit which resulted in more irregular circles than squares. A closeup of the holes cut in the mask is shown in Fig. 4.5. This was not expected to be a problem however, because circular contact pads are also acceptable. The holes still appeared to be large enough, and spaced far apart enough to yield usable contact pads that the probes could be placed on.

The whole assembly was placed inside the BAK 600 and metal contacts were deposited. Initially, it was chosen to use a 20 nm chrome layer with about 80 nm thick gold on top to make the contacts pads from, as this was a common material used in literature. However, the conduction measurements described later in this chapter quickly showed that gold contacts are very soft, meaning they can likely only be used once. This is illustrated in the left SEM image shown in Fig. 4.6. The probe station that was used for measurements with this device has very long arms and had positioning stages that produces a lot of vibrations, further increasing the damage to the contact pads. As a result, the second sample was made using a 20 nm layer of chrome, with a layer of about 80 nm of palladium as contacts, which
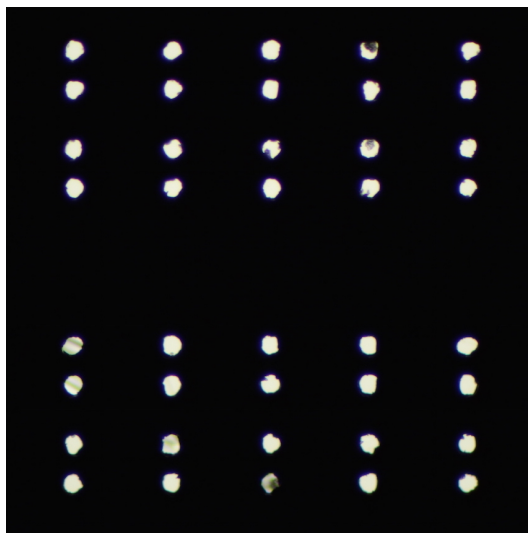
Figure 4.5: Picture taken of the deposition mask showing the resulting holes. The mask was cut using a laser cutter. As can be seen, the laser cutter was at its limits, meaning that the designed square holes turned out more as irregular circles.

was expected to be much stronger. In the end, a different probe station was used as well, which had much shorter probes and allowed for finer precision in placement of the probes, which produced less damage to the contact pads, as shown in the right image in Fig. 4.6. The final contact pads look as shown in Fig. 4.7. Both the gold and palladium contact pads have good sizes, and although they are not square turned out to be large enough for the probes to make a good contact. As can be seen, the palladium contact pads did 'leak' or spread out more than the gold. This did not show any effect in the final measurements, however.

For completeness, in Fig. 4.8, a single gold contact pad was imaged using the SEM. It shows that, although the contact pad has an irregular shape, it does have acceptable dimensions and is still fairly uniform.

A limitation of using the proposed method for depositing metal contact pads is that the contact pads cannot be positioned very accurately. The size of the graphene samples varies slightly, meaning the sample does not fit precisely inside the spacer ring. Also, positioning the mask on the spacer ring cannot be done with very high precision. As a result, it is very difficult to first pattern the graphene using the FIB, and then applying the contact pads, as then the position of these contact pads needs to be accurately defined. Because the FIB is used for patterning, it was therefore chosen to first apply the contact pads, before patterning the graphene. The FIB is capable of very high precision movements and can be used to pattern the graphene in between the contact pads easily. The proposed breadboard design allows this to be done, because the pads are spaced apart far enough so that the FIB can pattern around the contact pads and in between them. How this is done is explained in the next section.

4.2 Patterning the graphene

Now that the metal contacts have been applied, the graphene can be patterned to form e.g. a geometric diode. Patterning graphene can be done in many different ways. One common technique for patterning graphene is oxygen plasma etching, which can be used effectively to create graphene structures. In oxygen plasma etching, oxygen is flowed into
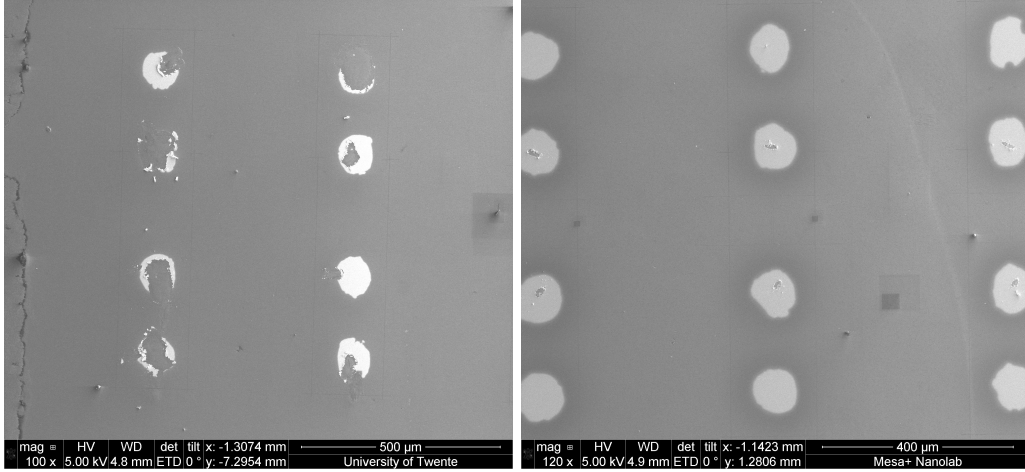
Figure 4.6: (left) SEM image of gold contact pads on graphene after measurements with the probe station. The contact pads were easily damaged by the probes, making it hard to repeat the experiment. (right) SEM image of palladium contact pads, which shows much less damage.
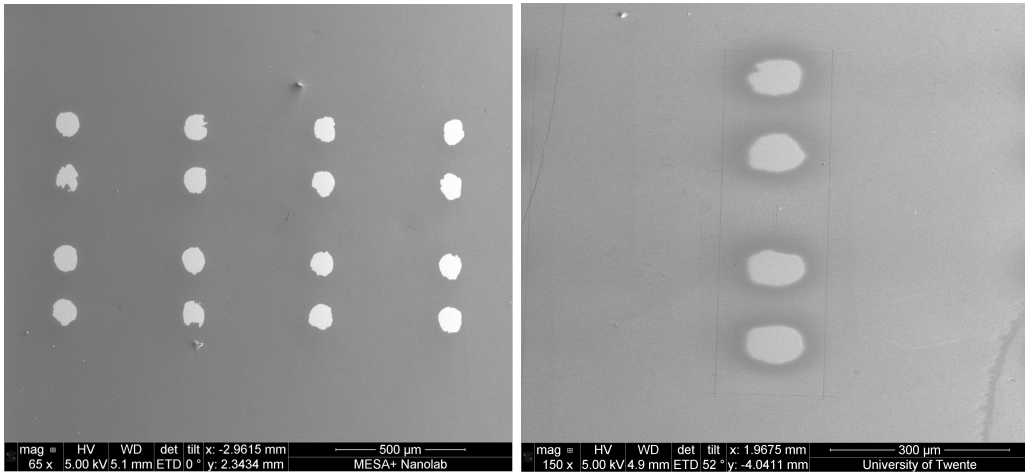

Figure 4.7: SEM images of gold (left) and palladium (right) contact pads on graphene. As can be seen, the palladium contact pads appear to have 'leaked' more than the gold contact pads.
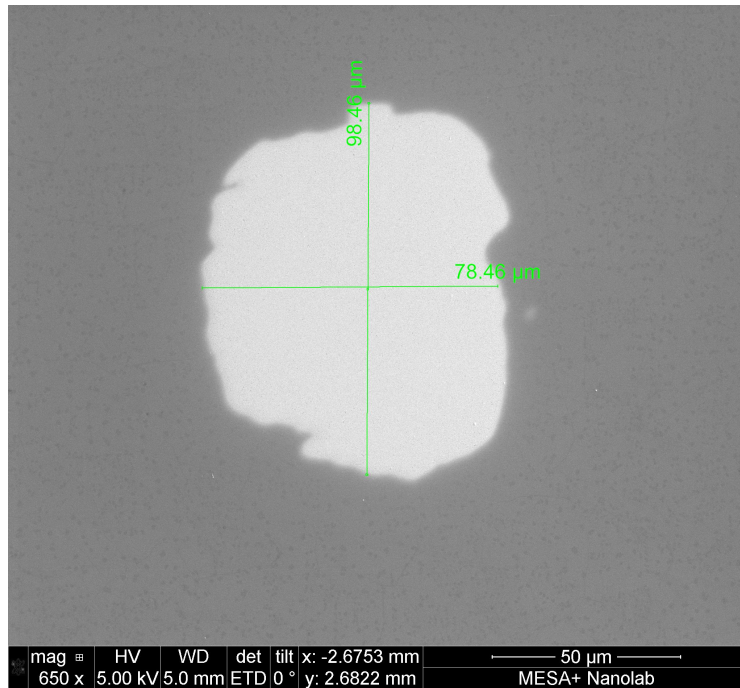
Figure 4.8: SEM image of a gold contact pad. The image shows that the contact pads are close to the designed size of 100 by 100 μm. The contact pad shown in this image is 98.46 by 78.46 μm. The size and shape varies between contact pads but most contact pads are sufficiently large for probe measurements.

a sample chamber where the graphene sample is present. This oxygen is then excited by microwaves [47]. The effect of the microwaves is to ionize the oxygen which then reacts with the graphene, creating defects and thus etches it where ever it can access the graphene. In order to control where the oxygen can etch away the graphene, a resist layer can be added on top of the graphene, after which it can be patterned using lithography. The result is that the oxygen plasma etches away the regions of the graphene that should be etched.

Oxygen plasma etching is a good technique for patterning graphene while causing marginal damage. However, it also involves many steps, e.g. designing a pattern, making a lithographic mask and then performing the lithography to pattern the resist, after which the oxygen plasma needs to be applied and then the resist needs to be removed. The research group also has access to a FIB and in the early stages of the project there was even the intention of using a Helium Ion Microscope (HIM), which is essentially a FIB but uses helium ions instead of gallium ions, greatly increasing the resolution. Unfortunately the HIM was no longer available during the project, so the FIB was used instead. This device has been known to pattern graphene without the need of any preparation steps for the sample. The sample can be loaded into the FIB, after which any pattern can be designed as the sample is being etched. It allows for a very large degree of freedom and adaptability. Patterns can be etched, tested and then adjusted if needed, without the need to design new masks. However, the FIB also has essential disadvantages. As the FIB uses heavy gallium ions to etch away graphene, it will cause collateral damage. Since the ions are so heavy and have high energies, any gallium ion incident on the graphene can be expected to cause damage. This effect is also illustrated in appendix B. The focused ion beam has a gaussian profile, meaning that some ions will fall outside the intended radius. Additionally, some of the ions may scatter in the chamber, implanting even farther in the graphene surrounding the region that should be etched.
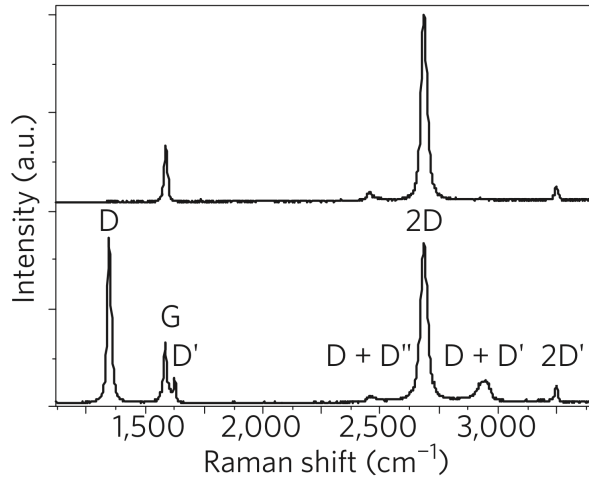
Figure 4.9: Raman spectrum of pure graphene (top) and damaged graphene (bottom).
The Raman spectrum of graphene can show three characteristic peaks: a so-called D peak at about
1350 cm^{-1}, a G peak at about 1582 cm^{-1} and a 2D peak at about 2700 cm^{-1} [49]. Image taken
from [48].

If the FIB is therefore used to etch away the graphene, it is essential to determine the
minimal gallium ion dose with which to etch the graphene. This dose should be just sufficient
to fully etch away the graphene, but low enough to cause minimal collateral damage. The
next section will discuss how this dose was determined.

Reducing collateral damage: determining the minimal FIB dose

In order to determine the minimal dose with which the graphene can be etched, a dose
determination experiment was carried out. In this experiment, the FIB was used to etch
away square regions of the graphene using varying gallium ion doses. Subsequently, Raman
measurements were performed to investigate the spectrum of the graphene inside the spectra.
The spectrum of graphene yields very important information about the quality and purity
of the graphene. In Fig. 4.9, the Raman spectrum of pure graphene (top) and damaged
graphene (bottom) is shown. In this spectrum, three characteristic peaks can be seen. The
so-called D peak occurs at about 1350 wavenumbers (cm^{-1}), the so-called G peak occurs at
about 1582 wavenumbers and the 2D peak occurs at about 2700 wavenumbers. However,
the spectral width, the height (noted as I(D), I(G) and I(2D)), the shape of a peak, and the
ratio between the heights of the peaks can give information about the sample that is being
viewed [48]. For example, in pure graphene, the D peak is suppressed due to the symmetry
of the graphene lattice. However, if the lattice is disrupted e.g. due to impurities or due to
damage, this symmetry is broken and the D peak emerges. This is then the first indicator
that the graphene might be damaged. In the research discussed here, it is relevant to know
at which gallium ion dose the Raman spectrum indicates that the graphene is fully damaged,
and therefore is no longer present. It is expected that as the FIB will begin to damage the
graphene, the D peak will increase in size, after which it is expected that the spectrum will
start to wash out completely above a certain ion dose.

The experiment is schematically illustrated in Fig. 4.10. Using the FIB, 50 by 50 μm
square regions are exposed to increasing gallium ion doses. For the Raman measurements,
a confocal Raman setup will be used that, as described in the previous chapter, has a focal
volume of about 1 μm^3. Also, it is desired to measure the uniformity of the FIB etching
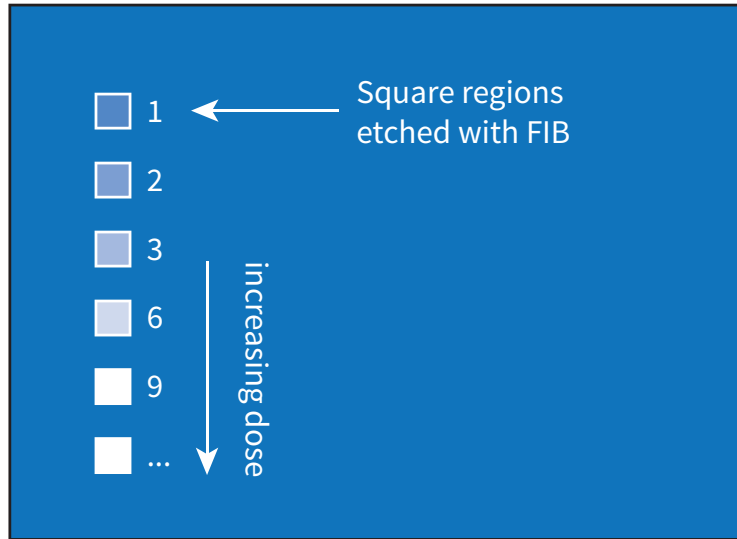
Figure 4.10: Illustration showing the process of determining the FIB dose. Square regions are etched using the FIB with increasing ion doses, which are later analyzed using Raman spectroscopy.

process, i.e. to see how homogeneous the graphene is after etching. For those regions, it is necessary to make the regions larger than 1 by 1 μm. To keep the etching time of the FIB and the measurement time of the Raman setup to a small enough time, the size of the region was therefore chosen to be 50 by 50 μm.

Before the graphene could be etched, it is necessary to determine which dose to use. To this end, a theoretical minimal gallium ion dose was calculated as follows. The assumption is made that the each gallium ion destroys whatever falls within its atomic radius. The atomic radius of the gallium ion is 135 pm. The circular area covered by a gallium ions is then 5.73×10^{-2} nm^2. A 50 by 50 μm square region has an area of 2.5×10^9 nm^2, meaning that 4.36×10^{10} gallium ions are needed to cover the entire region, or equivalently a dose of 17.5 ions/nm^2 is needed. This is a rough estimate of the absolute minimum dose for which the graphene could be etched away entirely. Due to the statistical nature of the FIB, the actual ion dose needed to accurately etch away the graphene will almost certainly need to be higher than this ion dose, but this provides a good reference with which the experiment could be started.

The gallium ion dose can be controlled in the FIB by controlling e.g. the gallium ion current, the dwell time of the beam, the beam overlap and the number of passes. The ion current directly controls how many ions per second in the beam are incident on the sample. The FIB will keep the beam at the same position for a set dwell time until it moves the beam to the next position. Depending on the beam overlap percentage, the FIB will move the beam exactly one beam diameter further (0% overlap) or e.g. half a beam diameter (50% overlap). The FIB will then move the beam from point to point until it has covered the entire area it has been instructed to cover (e.g. a square region). When the FIB has covered the area once, this is called a single pass of the FIB. Setting the FIB to etch the same pattern in one, two or three passes then means that the FIB will cover the same area one, two or three times, respectively. Logically, the effective gallium ion dose that the sample is exposed to is then one, two or three times the dose for a single pass. By setting an ion current, dwell time and beam overlap efficiently, the number of passes can be used to easily increase or decrease the gallium ion dose.

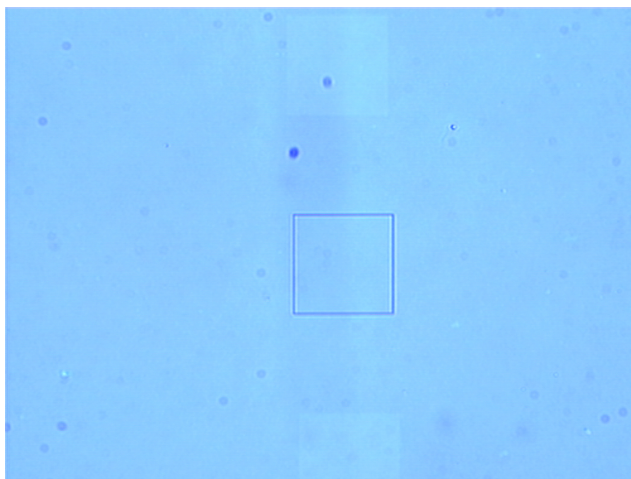The gallium ions that are incident on the sample are spread out over the beam area.

Figure 4.11: Image taken with the white light camera in the confocal Raman setup. In the middle, one of the square outline pattern is visible that was etched to help locate the square regions. However, it turned out that the square regions themselves were already visible.

The FIB used in these experiments has a gaussian beam profile with a full-width-at-half-maximum (FWHM) radius listed as 7.5 nm at a current of 1.5 pA. For a gaussian beam profile, 95% of the ions will be contained in the 2σ radius, where σ is the standard deviation. This standard deviation is related to the FWHM by FWHM $= 2\sqrt{(2ln2)}\sigma \approx 2.35482\sigma$. Solving this for σ, it is found that $\sigma = 3.185$ nm, meaning that 95% of the ions will fall in a circle with an area of 127.47 nm^2.

In the experiment the ion current was set to 90 pA, so that $90 \times 10^{-12} \times 6.241 \times 10^{18} = 5.62 \times 10^8$ gallium ions are incident per second on the beam area (127.47 nm^2). This converts to a dose of $5.62 \times 10^8/127.47$nm^2/s $= 4.41 \times 10^6$ ions/nm^2/s. To achieve a dose of 17.5 ions/nm^2, the dwell time could be chosen to be 3.97×10^{-6} s, where this assumes a beam overlap of 0%. In the actual experiment, the dwell time was set to 2.91×10^{-7} s, so that approximately 13 passes are expected to cover the sample with the minimum dose. This was done so that the dose could then be increased in smaller steps to investigate the effect of the ion dose in more detail.

The ion doses were set using the number of passes. The first three square regions were exposed to 1, 2 and 3 passes, after which the dose was increased each time with 3 passes until 75 passes, or roughly 6 times the theoretically calculated minimum ion dose. Additionally, strategically located square outlines were etched that had the same dimensions as the square regions that were etched. It was hoped that these outlines, because they show more contrast, would be visible under the white light camera in the confocal Raman setup.

After etching, the sample was placed under the confocal Raman microscope for inspection. Due to the high absorption of light of graphene, the etched squares were even visible using the white light camera, as shown in Fig. 4.11, and it turned out that the square outlines that were etched were not necessary to locate the square regions.

Various measurements were performed to inspect the Raman spectra of the square regions. The types of measurements that were performed are illustrated in Fig. 4.12. In each square, initially 3 random points were taken where single Raman spectra were taken. Since the final dose is fairly high, it is expected that in any case the graphene is completely gone. It is therefore interesting to know when the graphene Raman signal starts coming back, to investigate which dose is critical. Once the squares were located where the Raman signal started showing signs of graphene, a line scan was performed to investigate how sharp the transition is from untouched graphene to etched graphene. This would give an indication for
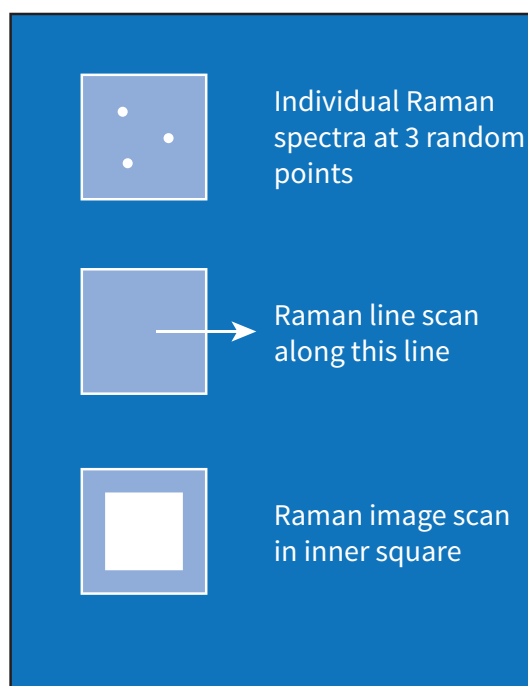
Figure 4.12: Illustration showing what types of Raman measurements were done. As illustrated, (top) Raman spectra were taken from three random points inside the squares, to see when the spectra start to show signs of graphene or lack thereof. (middle) A Raman line scan was performed across the border to investigate how sharp the etch process is. Finally, (bottom) Raman image scans were done to investigate the uniformity of the FIB etching process over larger distances.

how far from the edge the graphene is damaged. Furthermore, image scans were performed to investigate the uniformity of the etching process.

The results of the three single spectra per square are shown in Fig. 4.13. In the left top corner, the figure also features three Raman spectra for a region outside any square, i.e. where the graphene was untouched. It was found that for the square that had around 9 passes, the signal started showing more than just a flat background. The single Raman spectra for the squares with passes between 1 and 15 are shown in the figure. It is clearly visible that the Raman spectrum of the untouched graphene is similar to the spectrum of CVD-grown graphene. Remarkably, even after 1 pass of the FIB, the graphene already appears to be heavily damaged. The signal becomes more spread out the higher the number of passes, until above 12 passes the signal is completely gone and only background is measured. This seems to suggest that 12 passes are needed to completely remove the graphene, which is close to the theoretically calculated minimal dose.

As a next step, a line scan was performed in the square with 6 passes, to investigate how far from the edge the graphene would still be damaged, i.e. how much collateral damage has occurred. The result is shown in Fig. 4.14. In the left bottom graph, Raman spectra taken along the line scan are plotted in a heat map, where the color denotes the photon count. Blue is the minimum amount and red is the maximum amount. It shows that there is a clear border at around 6 μm along the line, indicating that this is where the square ended. The line was positioned roughly with the middle on the edge. It also appears that the edge is sharp, which is a good sign. In the left top graph, the intensity of the D peak at 1350 wavenumbers is plotted versus the distance along the line scan. This graph too shows that the edge appears to be quite sharp. Finally, a Raman spectrum is plotted, taken at 7 μm, to show that the spectrum outside the square looks like that of graphene, albeit damaged
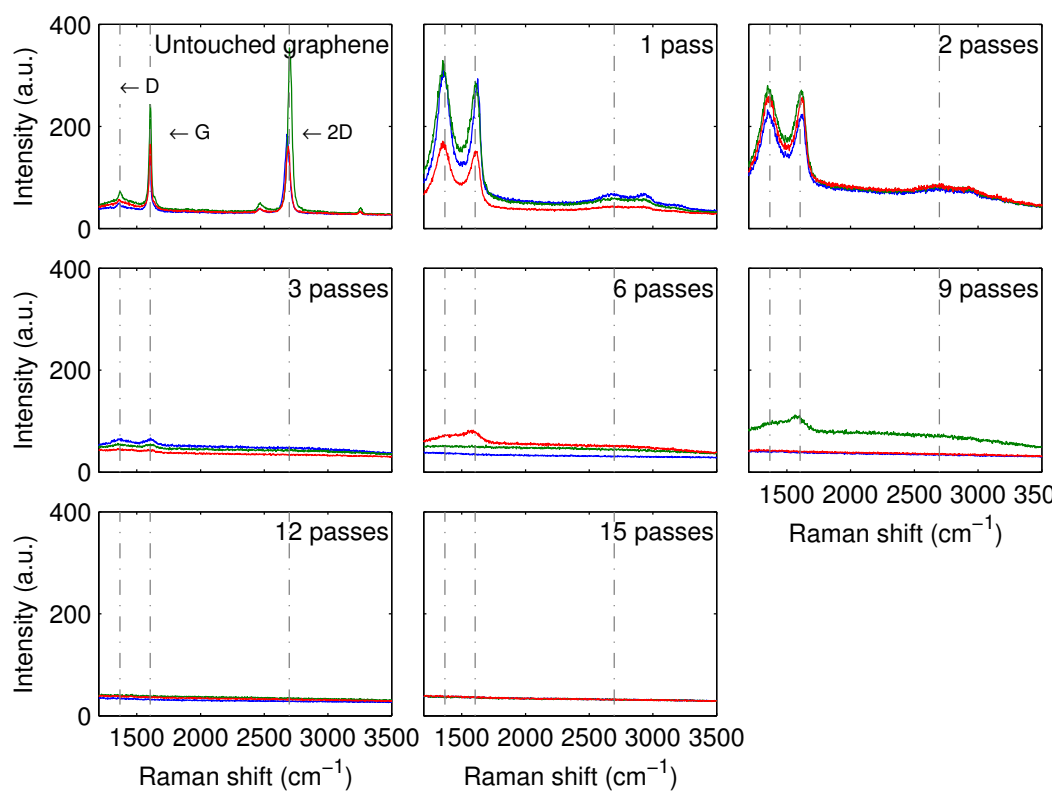
Figure 4.13: Raman spectra for three random points inside each square. The data shows that when no etching has occurred, i.e. the graphene is untouched (left top graph), the spectrum is that of graphene, with a low D peak and prominently visible G and 2D peaks. Already after one pass, for the lowest dose attempted, the graphene appears to be heavily damaged. Above 12 passes, the graphene appears to be completely gone.
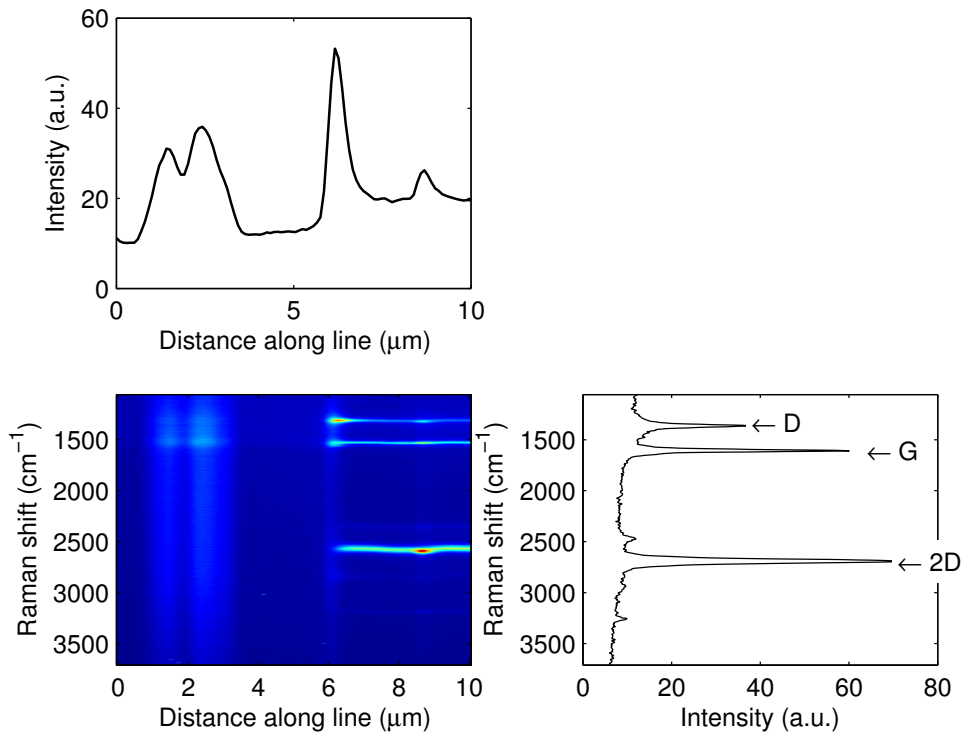
Figure 4.14: Line scan measurement results for the square with 6 passes. (left bottom) Plot showing the various Raman spectra along the line scan, where the color coding denotes the photon count. From blue to red means from no to maximum photon count. (left top) I(D) along the line scan. (right bottom) Raman spectrum at 7 μm shows a clear D peak.

due to the presence of a D peak.

The Raman spectra of the D, G and 2D peaks are zoomed in and plotted in Fig. 4.15. The graphs start at the edge of the square region, to show how the peaks decay along the line scan in the untouched graphene. The first noticeable feature in the graphs is that the signal seems to rise briefly at around 8.5 μm for all three peaks. This is likely due to random impurity sites on the graphene sample, as will be shown later with the image scans. Ignoring these bumps, these results then appear to show that the peaks stabilize to a fixed value over a distance of around 1 to 2 μm. Using the same intensity scaling functions, the intensity of the D peak in the untouched graphene is around 26 a.u., whereas, the D peak at the edge stabilizes to about 33 a.u. This appears to show that the graphene is damaged slightly, but the damage is minimal. The focal volume of the confocal Raman microscope is around 1 μm^3. This means that the distance of 1-2 μm could be even smaller in reality, but this cannot be confirmed using these measurements. In any case, it shows that the graphene is not substantially damaged more than 2 μm into the untouched regions.

As a last set of measurements, image scans were performed of the squares with 6, 9 and 12 passes, and of untouched graphene, so that these images could be compared to see the effect of etching with the FIB. The image scans covered a region of 30 by 30 μm, and were divided into 64 by 64 pixels. The Raman image scans yield hyperspectral data, i.e. a full Raman spectrum for each pixel. To analyze this hyperspectral data, a MATLAB program was written that could create hyperspectral images. The program allows the user to select a wavenumber for which a grayscale image is made. Effectively it then takes the
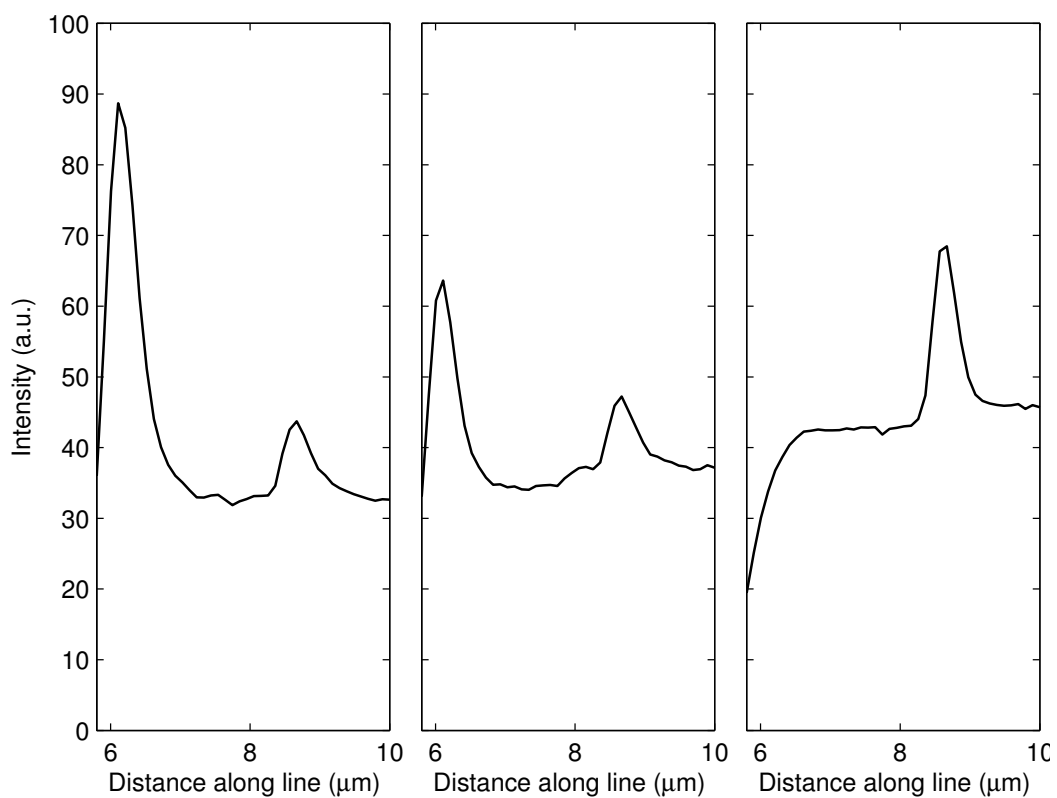
Figure 4.15: I(D), I(G) and I(2D) versus the distance across the border (along the line scan). Here, 0 μm in these graphs corresponds to 28 μm in Fig. 4.14. The graphs show a clear peak in intensity just at the border (around 0 μm), but quickly relax after roughly 10 μm, indicating that the graphene is damaged at least 10 μm outside the intended etched region.
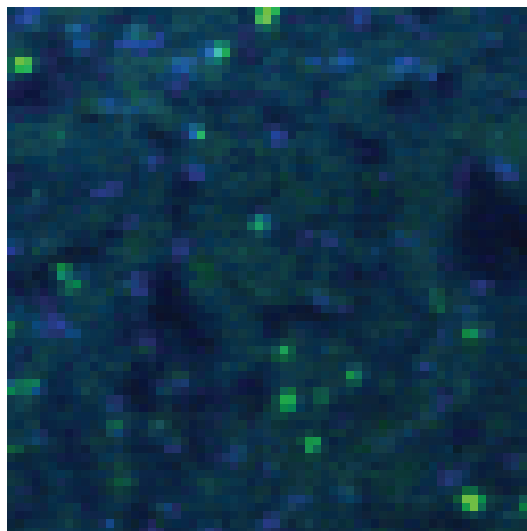
Hyperspectral image

Figure 4.16: 64x64 pixel hyperspectral image of a 30 by 30 μm region of untouched graphene. The three channels red, green and blue have been assigned to the D, G and 2D peaks, respectively. A more green pixel thus indicates the green component (or the G peak) is more present in the spectrum, whereas a more blue pixel indicates that the blue component (or the 2D peak) is more present in the spectrum. This thus yields direct visual information about e.g. the I(2D)/I(G) ratio.

intensity of the signal at that wavenumber at each pixel, and displays the value as a grayscale color. The program allows up to three such wavenumbers to be selected, after which three grayscale images are produced. By assigning each grayscale image to either red, green, or blue and then rendering the RGB image, a hyperspectral image is created which can provide information about the structure. An example image is presented in Fig. 4.16. In this image, untouched graphene was imaged, where the red, green and blue color channels were assigned to the D, G and 2D peaks, respectively. The resulting image thus contains information about all three peaks, where this information is color encoded. A pixel that has a greenish color, for example, contains more green component, meaning that the G peak is stronger in the spectrum, at that location. Likewise, a blueish pixel indicates that the 2D peak is stronger at that location. It is therefore possible to directly analyze what kind of material is present at which location.

From the example image in Fig. 4.16, it is already clear that untouched CVD graphene contains a lot of variations. Analysis shows that these areas are likely either single, double or multilayer graphene, or defects in the lattice. In between, the bright areas, the graphene is reasonably uniform, showing a green hue, indicating that the 2D peak is slightly higher than the G peak, which is the case for CVD grown graphene on Si/SiO$_2$.

Fig. 4.17 shows hyperspectral images created in a similar way for untouched graphene, and the squares with 6, 9 and 12 passes. The hyperspectral images have been made with the same wavenumbers for each image. This means that the images show how the peak intensities change as the graphene is etched. It is clearly visible that increasing the number of passes decreases the overall intensity. However, some of the features remain visible in the images as small blobs. To analyze these features, the Raman spectra were extracted at those pixels, and are shown in Fig. 4.18. Upon closer inspection of the Raman signal of the 'blob', the spectrum appears to be that of amorphous carbon, as shown in Fig. 4.19. This implies that the graphene has been damaged to the point where it now looks like amorphous
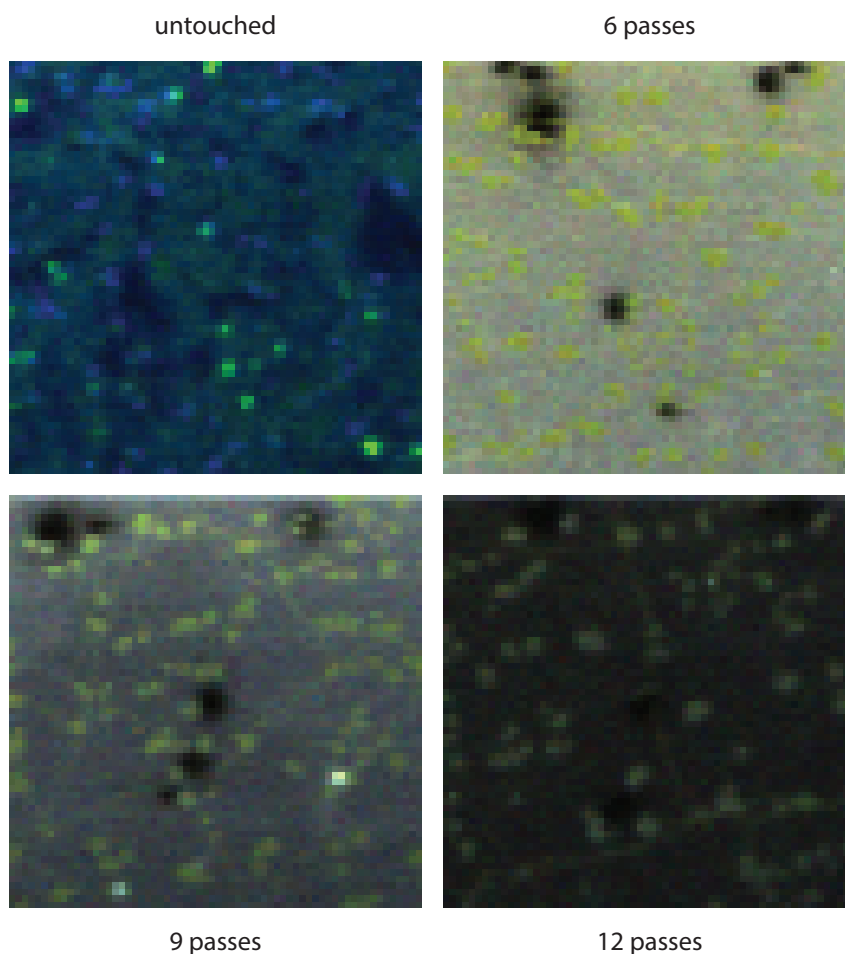
Figure 4.17: 64x64 pixel hyperspectral images of 30x30 μm regions of graphene which have been etched with varying number of passes. Each hyperspectral image shows the intensities of the D, G and 2D peaks as red, green and blue colors, respectively.

carbon. The 'blobs' may be multilayer graphene or graphite, that has grown locally due to the CVD process. Naturally, this material will be harder to remove with the FIB.

From the above results, it seems that a dose of 12 passes, or the theoretically calculated dose of 17.5 ions/nm^2 is sufficient to remove all graphene, or at least to destroy it up to the point where it has become amorphous carbon. However, there is one important downside to the method that has been used up to this point. In the previous experiment, complete regions of graphene were etched away. This is an effective way of patterning the graphene, but perhaps a better way of achieving effectively the same result is to etch outlines of structures. By etching outlines, the graphene is effectively cut through. Since the graphene lies on a insulating substrate, cutting through the graphene should be equivalent to completely removing the graphene from other areas. In the end, the goal is to electrically isolate parts of the graphene, to form a device such as a geometric diode.

The etching of outlines has many advantages. In the case of areas, the FIB will scan the area it needs to etch line by line, until it has covered the full area. This means that the FIB will come close to the same region several times, potentially increasing the amount of collateral damage. Additionally, etching full regions takes more time. It was therefore chosen to only etch outlines in the final process, using the same dose as calculated. This also
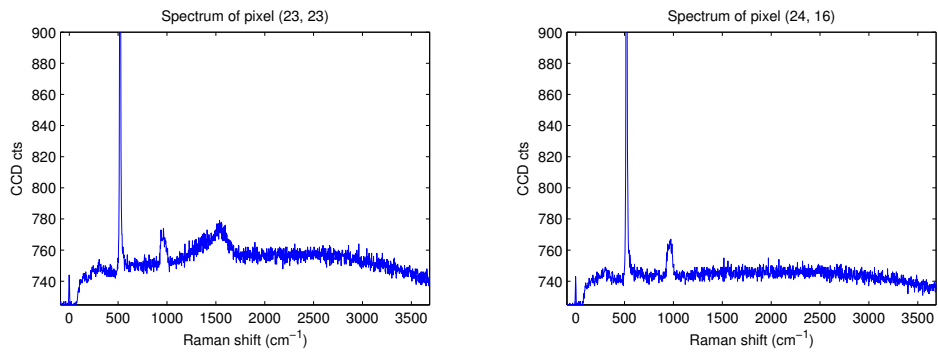
Figure 4.18: Raman spectrum of one of the 'blobs' in the square region with 12 passes (left) and Raman spectrum of the region in the area between blobs.
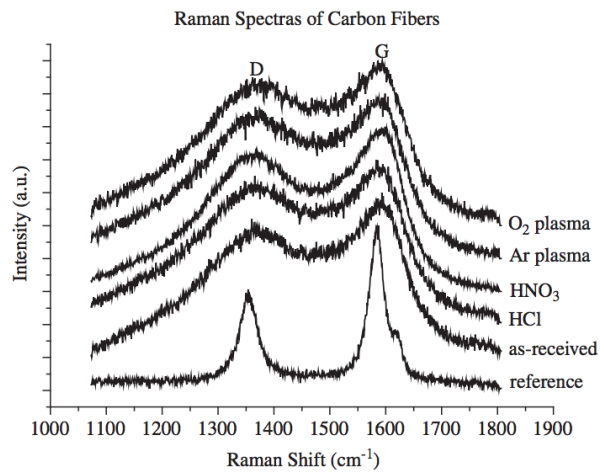

Figure 4.19: Raman spectrum of amorphous carbon. Image taken from [AMORPHOUS-CARBON].

opens up an interesting alternative type of experiment, to determine the minimum dose with which to etch the graphene. In the end, the goal is to create structures in graphene that are electrically isolated. The minimum dose that is required can thus be determined by etching around a contact pad to electrically isolate it from the bulk graphene. By then measuring I(V), the result should be that no conductance is measured. By increasing the dose from the FIB until this point is reached, the most effective, minimal dose can be determined.

The patterning recipe

Now that contact pads can be deposited, and the ion dose is known with which to etch the graphene, the actual etching could be done. As discussed in the previous section, it is sufficient to electrically isolate the graphene from the bulk graphene, in order to create a device such as a geometric diode. For that reason, it was chosen to only etch outlines with the FIB to define the shape of the final device, and not to etch away entire areas. The dose in that case can be kept on the same order as before, but it could be that a slightly lower dose is also sufficient.

The total outline process that was used to create e.g. a geometric diode is illustrated in Fig. 4.20. The FIB has a maximum working area of approximately 800 μm in both directions. In other words, the FIB cannot be zoomed out further. The final four-point configuration was slightly longer than this, meaning that the contact pads could not be isolated from the bulk graphene with one rectangular shape around them. As a result, a process was designed to create two U-shape outlines, that would connect to form a larger rectangle around the contact pads to electrically isolate them. This is illustrated in steps 1 through 3 in Fig. 4.20. As a next step, the graphene devices could be etched in between the two middle contact pads. However, the graphene devices will have characteristic sizes of several hundreds of nanometers. To achieve sufficient resolution with the FIB, the working area should be reduced, i.e. it needs to zoom in. This is because the FIB has a 16-bit controller board which controls the beam. It therefore has a 16-bit resolution in the working area it has been set to, of which 14 bits are accurate. To achieve a resolution on the order of 1 nanometer, the working area could therefore be no more than 16 μm in both directions, which corresponded to a magnification of roughly 5000 times. The rectangular outline around the contact probes shown in Fig. 4.20 is wider than 100 μm, since the contact pads themselves are on the order of 100 μm. For that reason, a narrowing was introduced, that narrows down to 5 μm. This is shown in step 4.

After the narrowing has been etched, the next step is to etch in an actual shape, such as a geometric diode. This can be achieved in a similar way to the outlines that were etched before, except this time it is done at a larger magnification to achieve smaller structures. The example of creating a geometric diode is illustrated in Fig. 4.21. In this case, two cone-shaped line segments are etched in the graphene. On the left hand side, the solid white lines indicate the pattern that is to be etched, with the light blue lines indicating the narrowing that was etched in earlier. On the right hand side, the final structure can be seen. The area of the graphene that will support a current is shown highlighted. This shows a characteristic diode arrowhead constriction, meaning that it is expected that this device should work like a geometric diode.

Now that the concept is clear, the last step needed before the patterns can actually be etched is to know where the FIB is on the sample. Unfortunately, as has been demonstrated previously in this chapter, the FIB cannot be used to look at the sample. This is because even a low dose will damage the graphene. This means that the patterning must be done blind. Fortunately, the FIB also has an SEM module inside it. SEMs are much less destructive than the FIB, meaning it could be used to look at the sample. It does mean that the FIB and the SEM must be aligned, i.e. the centers of both beams must be made to overlap, and the focus of both beams must be the same, which can be difficult to achieve since they are
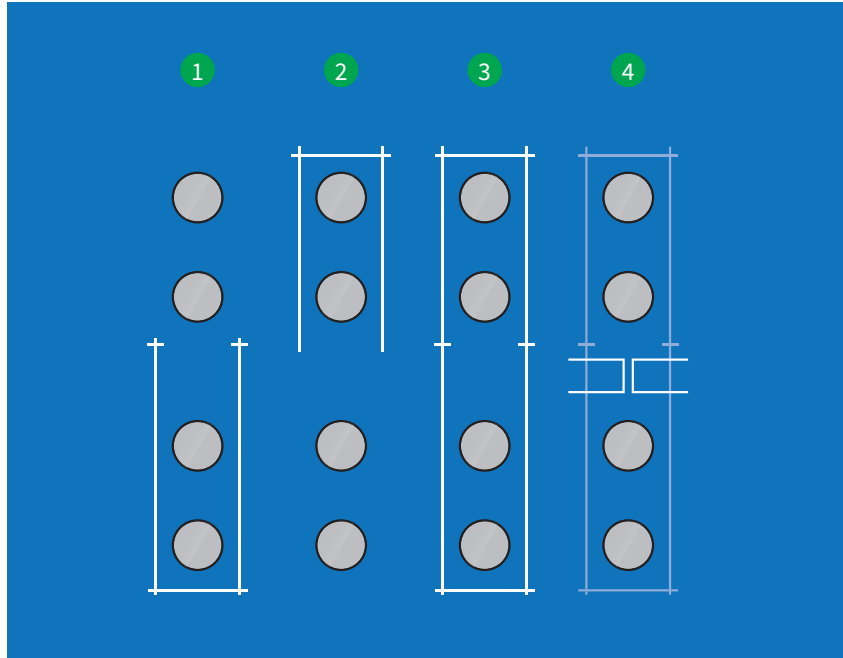
Figure 4.20: Illustration showing the concept behind etching outlines. Due to the limited working area of the FIB, first a bottom U-shape is etched, and then a top U-shape is etched to create a full rectangle around the four-point contact pads. Next, a narrowing is etched, in which devices can be etched later.
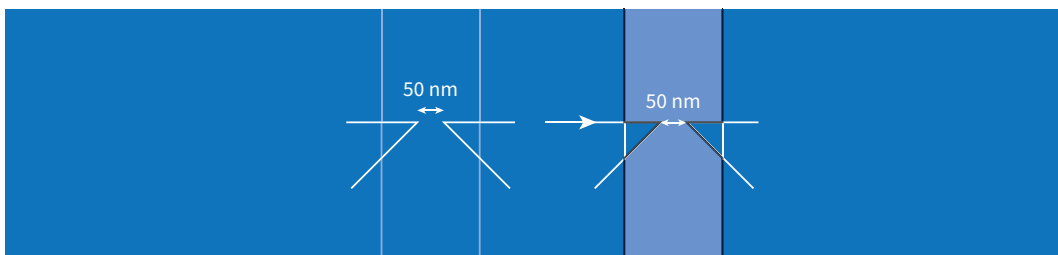

Figure 4.21: Illustration showing how a geometric diode could be patterned. Two cuts are needed to shape the graphene in the narrowing to form what is called a geometric diode.
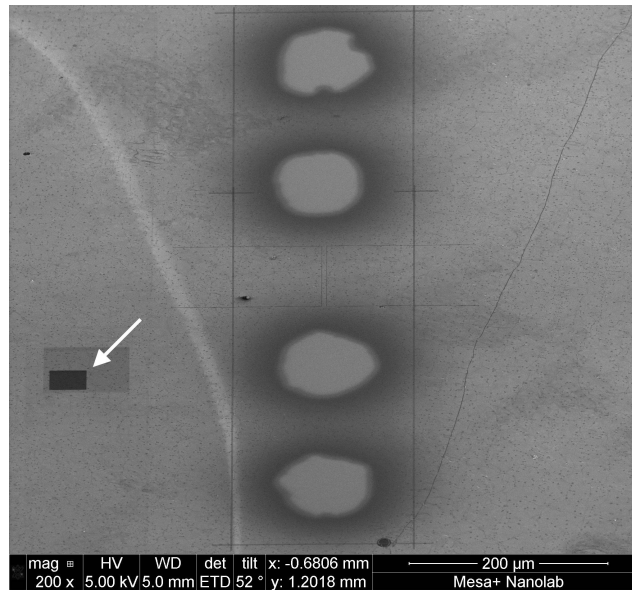
Figure 4.22: SEM image showing an alignment and focus mark for the FIB and the SEM. The dark square region indicated by the arrow marks the location where the FIB was turned on long enough for the graphene to be removed, leaving a clearly contrasting region. The SEM and the FIB were then aligned so that the center of both images lined up on e.g. the top right corner. After this, the SEM could be used to position the FIB.

independent systems. If the FIB and the SEM can be aligned, however, then the SEM can be used to navigate and and position, and the FIB can be used to pattern the graphene.

This alignment is best done at a location on the graphene where no samples of interest will be made. After alignment, the position of the SEM should then correspond to the position of the FIB, so that the position of the SEM can be used as a reference. To align the FIB and the SEM, the SEM beam was positioned in the middle of two four-point setups. This location was chosen to keep the location where the beams are aligned as close to the actual region that is to be patterned as possible. This minimizes the chance of the two beams drifting as the sample is moved. Then, the zoom level was increased far enough so that a region of about 60 by 60 μm was visible, meaning no damage will be done do any of the actual samples when the FIB is turned on. At this point, the FIB was set to make enough images until the graphene was sufficiently damaged to expose the Si/SiO_2 underneath. This resulted in enough contrast for both the FIB and the SEM to see. See for example Fig. 4.22. In this image, a dark square can be seen with a slightly dark square around it. The dark square corresponds to the region exposed to the FIB after just a few passes (also illustrating the severity of the damage). As a next step, the stage is moved so that the center of the FIB is aligned with e.g. the top right corner of the dark square. Next, the SEM is turned on and it is inspected if the center of the SEM beam is also on the top right corner of the square. If this is not the case, the two beams are not aligned, and the SEM is adjusted until it does sit directly above the top right corner of the dark square.

From this moment on, the two beams are aligned and, in theory, the etching process can begin. In reality, it was discovered that the two beams appear to 'drift' apart as the sample is moved farther from the point where the alignment originally took place. This is most likely due to the slight error in the angle under which the sample is mounted, due to the limited angular precision of the positioning stage. Both the SEM and the FIB have extremely long focal distances, meaning that even if the sample is moved away farther from the beam, this will not be reflected in the images, because they remain in focus. However,

due to the difference in angles between the FIB and SEM beam, the two beams do appear to 'drift' apart as the sample is moved farther. For this reason, it turned out to be difficult to align both the top and bottom U-shapes of the outlines while etching, for example. After some deterministic optimization of the alignment process[1], however, it was learned how to deal with this by using a precise protocol and aligning as close to the sample of interest as possible.

One last issue remained with the fabrication process. The program used to operate the FIB has the ability to let the user draw patterns and outlines that the FIB can then etch. This is, for example, how the top and bottom U-shapes were drawn. It turned out that the precision of this program is limited, as it tries to determine on its own how to move the FIB so that the desired pattern is produced on the sample. For outlines, it does so by approximating each individual line shape. This can yield issues if lines are intended to exactly overlap at the ends, because this is not always the case. To solve this, the U-shape outlines were drawn so that they always contains crossing lines, as shown in Fig. 4.20. This ensures that even if the lines are not exactly where they were intended to be, they will certainly cross and therefore still be connected. The same cannot easily be done for the narrowing and e.g. a diode shape, because there, continuous shapes are actually needed. As a result, stream files were created. These are raw files in which exact commands are sent to the controlling circuit of the FIB. These in turn tell the FIB where the beam needs to be, and for how long, allowing for precise control. A MATLAB program was created to generate the narrowing and diode shape stream files, which allow the user to choose e.g. the width of the narrowing, and the width and angles of the diode. These stream files were then tested in the FIB to see if they produced the desired shapes.

In Fig. 4.23, the result of one such diode shape is shown in a SEM image. In this case, a diode shape was made with an intended neck width of 70 nm, and an angle of 45 degrees. The resulting pattern in the graphene shows that a clean cut was made, and the resulting neck width was measured to be roughly 50 nm. This mismatch in neck width is present because in the MATLAB program, it was assumed that the beam has a width equal to the FWHM. In reality, the effective beam width will be more than that, meaning that the effective width of the neck is reduced.

In the end, the process could be perfected, and very good results were achieved. An example was already shown in Fig. 4.22. This SEM image shows the result of the rectangular outline around the contact probes, with a 5 μm gap etched in between. Close up SEM images revealed that the outlines were almost perfectly aligned, meaning that the recipe works as expected and the designed shapes can be reproduced.

Now that the fabrication process works, it was time to create actual devices and test whether they work as expected. The next chapter will discuss final structures that were etched and the resulting I(V) measurements done using the probe station.
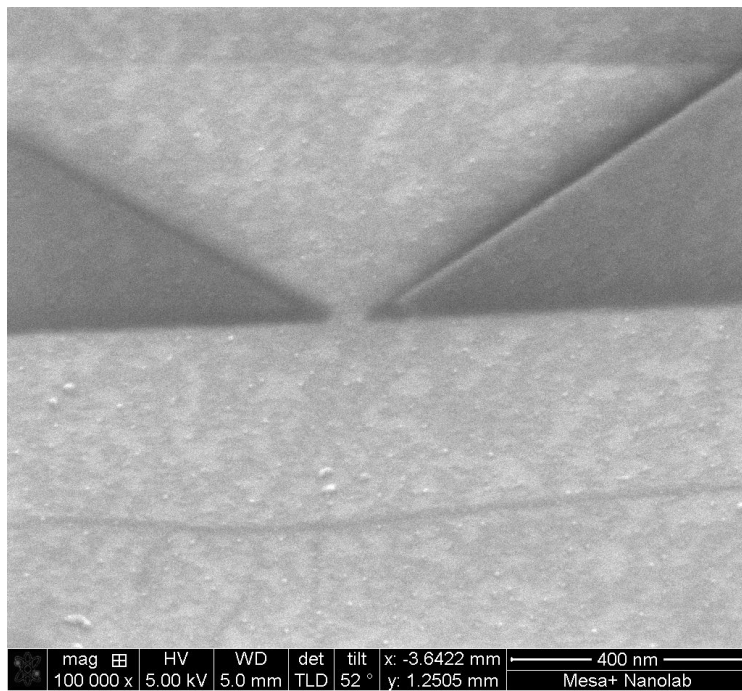
---

[1]i.e. trial and error

Figure 4.23: SEM image of a test with the stream files. The SEM image shows a diode shape with a designed neck width of 70 nm. The measured neck width of 50 nm.

Chapter 5

Results of probe station measurements

The last step of the research project involved the actual fabrication and measurement of geometric diodes using the FIB as a patterning tool. In this chapter, these fabrication steps and resulting samples and measurements performed with the probe station are shown and discussed.

5.1 Sample fabrication and verification measurements

As explained in the previous chapter, the fabrication of any device, such as geometric diodes, is done in a few steps. First, metal contact pads are deposited onto the graphene. Then, a rectangular outline is etched around these contact pads to isolate a four-point setup from the bulk graphene. Next, a narrowing is introduced in between the two middle contact pads, which will help make the fabrication of the diode shapes possible. Finally, the diode shape is etched in the narrowing, and the end result is hoped to work like a geometric diode.

It was initially interesting to know if the graphene would conduct at all. Additionally, it was hoped that we could show that the FIB did not cause so much collateral damage that no conductance takes place at all. For that reason, initially, conductance measurements were performed. Specifically, I(V) responses were measured using two of the probes in the probe station:

1. between two points on graphene, without any contact pads;

2. between contact pads from two neighboring four-point setups that were either

   (a) not electrically isolated from each other;
   (b) electrically isolated from each other by the FIB.

3. between contact pads in the same four-point setup, while

   (a) the four-point setup is electrically isolated from the bulk graphene, but nothing else;
   (b) the four-point setup is electrically isolated from the bulk graphene, and a bar is etched out between the middle two contact pads, to isolate the upper and bottom parts of the four-point setup;
   (c) the four-point setup is electrically isolated from the bulk graphene, and there is a narrowing of 5 or 10 μm;
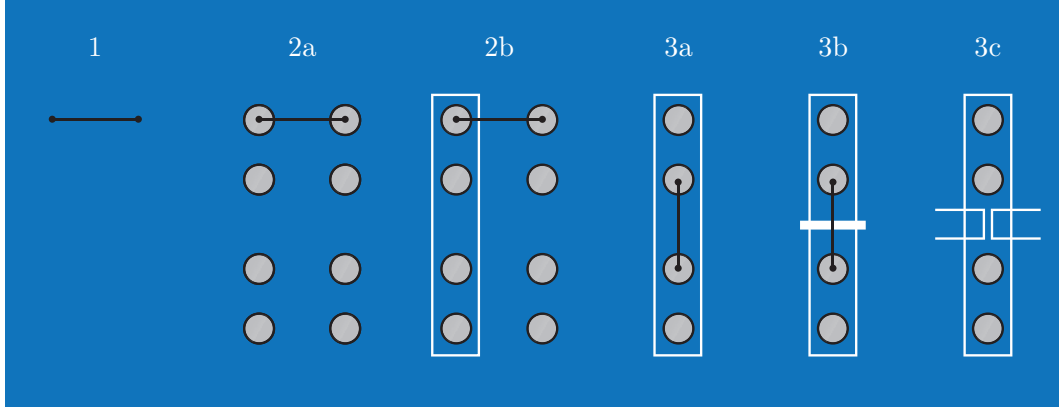
Figure 5.1: Illustration showing how the conductance measurements were done. The solid lines with dots at the end represent between which points an I(V) curve was measured. The white lines and rectangles mark etching lines and areas.

(d) the four-point setup is electrically isolated from the bulk graphene, and a gating voltage is applied to change the Fermi level of the graphene.

Measurements 1 through 3c are also illustrated in Fig. 5.1. Only two probes are used in this case, because this was easier to use, and it was interesting to know if the sample conducted at all.

In the first measurement, it is checked if it is possible to place the probes directly onto the graphene to measure current. The expectation is that since the probes are so large and vibrate, they will damage the graphene, reducing the conductance and hence the resistance is expected to be large. It therefore may be that current flows, or not, depending on the amount of damage. In any case, the assumption is made that SiO_2 is isolating so that if current is measured, it must flow through the graphene.

The second set of measurements is aimed to test if the contact pads offer good conductance to the probes, and if current can flow through the graphene. If at least one of the four-point setups has been isolated from the bulk graphene because a rectangular outline is etched around it, no current is expected to flow. However, if neither four-point setup is isolated, then current should flow between them. The expected I(V) response is then linear, because there is no geometric shape to determine a preferential direction for current to flow in. Additionally, the sheet resistance is expected to be low, around $450 \pm 40 \ \Omega/\square$, based on information from the manufacturer of the graphene (see also appendix A).

In the third set of measurements, measurement 3a is effectively the same as measurement 2b, but is done for comparison. Measurement 3b is likewise expected to yield similar results as 2b, but in case 3b an area is etched with two different doses, much like in the dose determination experiments. This experiment was performed to test whether it matters for conductance if an outline or a square region is etched away. Measurement 3c is designed to test the effect of a narrowing. In this case, the narrowing is a symmetric structure, with no constriction with dimensions close to the MFPL, so a linear response is expected.

Furthermore, a difference in measured resistance is expected when measuring with either four or two probes, i.e. using the four-point probe method or just two probes. In the case where two probes are used, contact resistance is expected to be measured as well, so the measurement result should yield a higher resistance for two probes than for four.

The fourth set of measurements (not shown in Fig. 5.1) is done to test the effect of a gating voltage applied to the silicon substrate underneath the graphene. The gating voltage is applied on the silicon so that the graphene feels an external electric field, which alters (i.e. raises or lowers) the Fermi level of the graphene. As discussed in Chapter 1, changing the
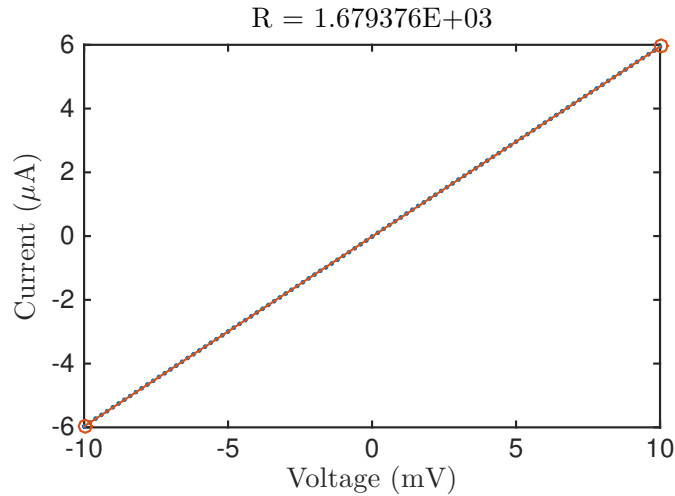
Figure 5.2: I(V) curve when the two probes were placed directly on to the graphene. The response is clearly linear and the resulting resistance is 1.68×10^3 Ω. The solid line is a linear fit to the data, and the dots represent the raw measurement data.

Fermi level means that the symmetry between holes and electrons can be broken or actually induced, depending on where the Fermi level lies, and electrons or holes may thus become the majority charge carriers for a suitable gating voltage. If now a bias voltage is applied across the graphene, a current will flow. Depending on the gating voltage, this current is expected to increase or decrease, as the Fermi level of the graphene is raised or lowered.

Measurement between two points on graphene, without any contact pads

A first measurement was done where the probes were placed directly on the graphene, without any contact pads underneath. The resulting I(V) curve is shown in Fig. 5.2. It can immediately be seen that the I(V) curve is linear, symmetric, and that the corresponding resistance is 1.68×10^3 Ω. This shows a few very important results. First, the graphene clearly conducts, as when the probes were lifted free from the graphene, no current was measured at all. Also, SiO_2 is an isolator, which has resistances well into the GΩ, meaning that this current must be flowing through the graphene. Secondly, it shows that apparently, the probes can also be placed directly on the graphene, to measure current. It was noticed, however, that it required some slight repositioning of the probes before the contact was good enough. It was not a trivial matter of placing the probe onto the graphene and then measuring. However, similar results were found elsewhere on the graphene, meaning that I(V) measurements could technically be done without contact pads. Last, it shows that it does not matter in which direction the voltage is applied.

Measurements between contact pads from two neighboring four-point setups

The next set of measurements were performed between two neighboring four-point setups, either when the two setups were isolated from the bulk graphene, or not. First, measurements were done when the four-point setups were not isolated from each other. This was expected to yield equivalent results to the free graphene. A first result is shown in Fig. 5.3. In this image, an SEM image of the two points that was measured between is also shown, after
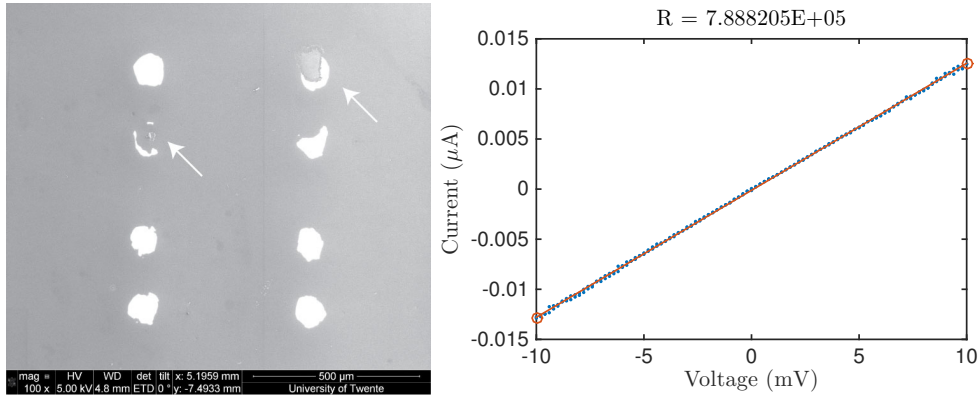
Figure 5.3: (left) SEM image of measuring points after measurement and (right) resulting I(V) curve measured between the two points. The response is clearly linear and the resulting resistance is $1.68 \times 10^3 \Omega$. The solid line is a linear fit to the data, and the dots represent the raw measurement data.

measurement. Such images could probe useful later on in explaining some of the results. The arrows indicate between which two points a measurement was done. To the right, the I(V) curve is shown. This again shows a very clear linear response, as expected. This time, however, the resistance looks to be two orders of magnitude larger than measured when the probes were placed directly on the graphene. However, as can be seen in the figure, there appears to be a faint vertical line between the two four-point setups. This line was not put there by the FIB, and may be the result of a scratch or a crack in the substrate. It could be that this line inhibits conduction, which could explain the increased resistance. Furthermore, it may be that the contact resistance is larger than for probes on pure graphene. This can be tested further later on when measurements are performed inside the same four-point setup.

To be able to say for sure if this resistance is large or small, another set of measurements was done between four-point setups which were isolated by the FIB from the bulk graphene, using the rectangular shape described earlier in section 4.2. Four measurements are shown in Fig. 5.4. In the left column, SEM images are shown of the samples that were measured. The arrows indicate where the probes were placed, and thus between which points the I(V) curve was measured. The right column shows the resulting I(V) curve for each measurement. These graphs look quite different from the I(V) responses seen in Figs. 5.2 and 5.3. In this case, the four-point setups were isolated by a rectangular outline etched around them with the FIB. The resulting resistances were (from top to bottom) 1.23×10^9, 1.65×10^9, 5.38×10^9 and 5.93×10^9 Ω. Looking at the actual I(V) measurements, it is clear that the signals just contain noise, meaning that apparently no current was flowing at all, and thus the resistance could not be measured. This is a good result, as it shows that, compared to when the sample is not isolated, isolating the samples with the FIB ensures that no current can flow. Hence, the samples are truly electrically isolated.

Measurements between contact pads in the same four-point setup

The next step involved measuring I(V) characteristics between contact pads in the same four-point setup. As explained, four types of measurements were done in this set of measurements. The first type of measurement involved measuring an I(V) curve between two contact pads, while the four-point setup was electrically isolated from the graphene, i.e. 3a in Fig. 5.1. Two such measurement are shown in Fig. 5.5. In this case, the measurements were done using two probes on either the inner or the outer contact pads to see if there is a difference between the two.
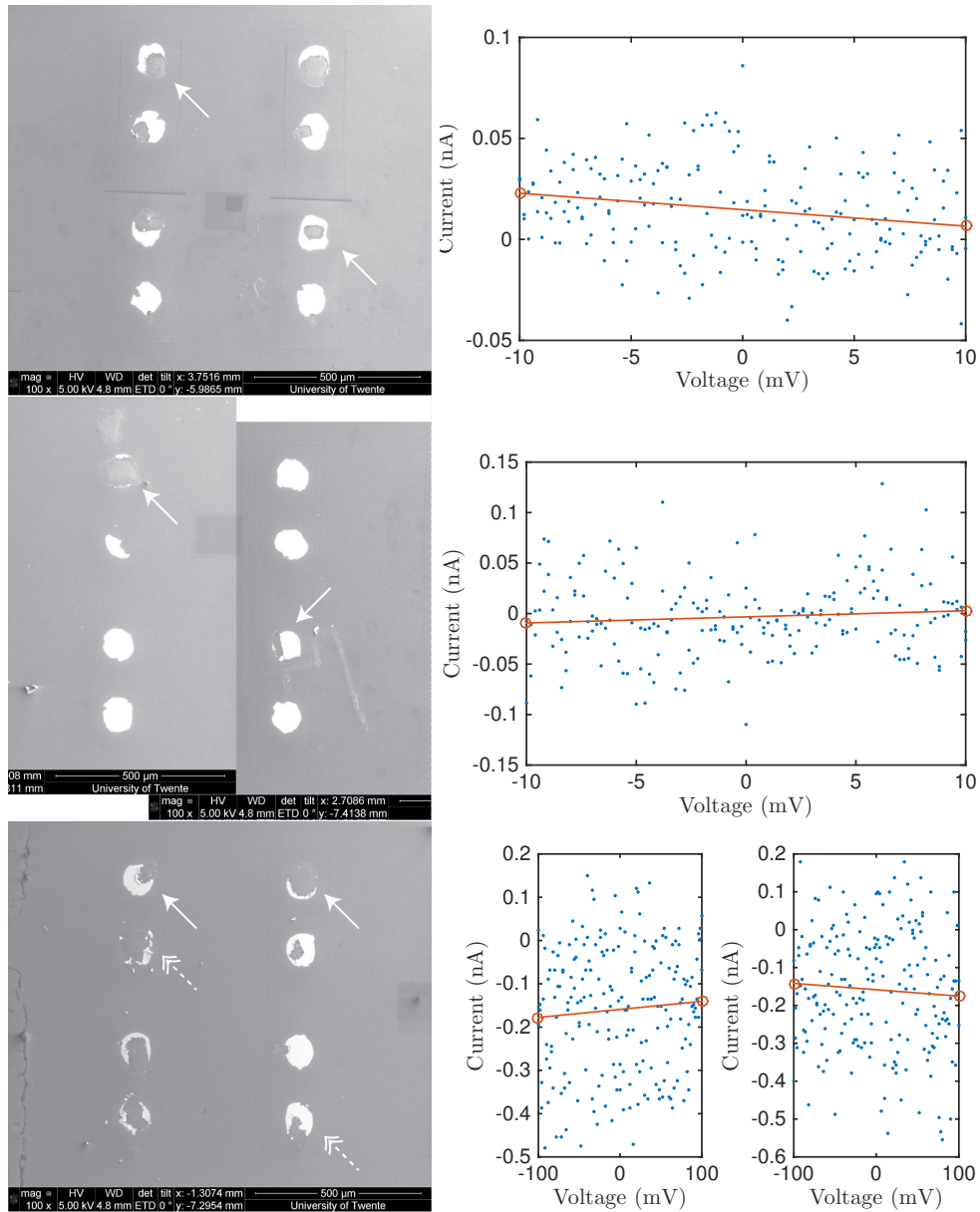
Figure 5.4: Multiple I(V) measurements between isolated four-point setups. The measurements were performed between the points indicated by the arrows. The SEM images show the sample after measurements. The I(V) graphs on the right show the raw data as blue points and a linear fit through this data as a solid red line. In the last row of measurements, the I(V) curve between the contact pads indicated by the solid arrows is shown in the left graph, and the I(V) curve between the contact pads indicated by the dashed arrows is shown in the right graph.
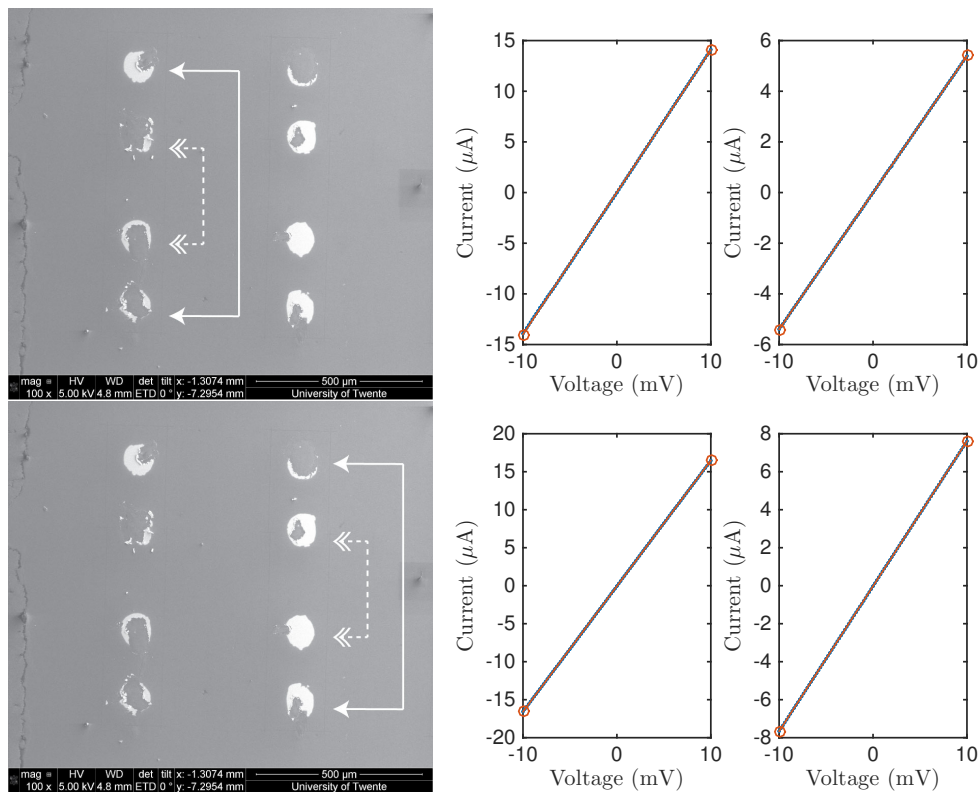
Figure 5.5: Multiple I(V) measurements inside isolated four-point setups. The measurements were performed between the points indicated by the arrows. The SEM images show the sample after measurements. The I(V) graphs on the right show the raw data as blue points and a linear fit through this data as a solid red line. The I(V) curve between the contact pads indicated by the dashed arrows is shown in the left graph, and the I(V) curve between the contact pads indicated by the solid arrows is shown in the right graph.
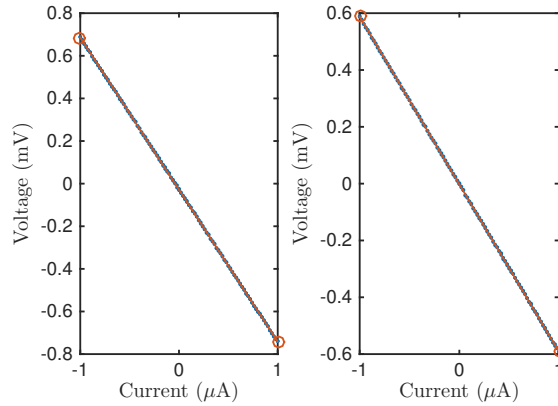
Figure 5.6: Four-point probe measurement of the same samples as in Fig. 5.5. The left graph in this figure is the V(I) measurement of the sample shown at the top of Fig. 5.5 and the right graph in this figure is the V(I) measurement of the sample shown at the bottom of Fig. 5.5.

The results clearly show that the responses are again linear and symmetric, as expected, and that the resistances are low. For the first set, the resistances for the inner contact pads and the outer contacts pads are 7.13×10^2 and 1.85×10^3 Ω, respectively. For the second set, the respective resistances are 6.05×10^2 and 1.31×10^3 Ω. Compared to the measurement where the probes were placed directly on the graphene, 1.68×10^3 Ω, this shows that the contact pads may in fact improve electrical contact and resistance with the probe station. Furthermore, the close similarity to the results between two different four-point setups shows that the experiment is repeatable. It also shows clearly that the measured resistance increases as the distance between the probes increases, as for both cases the outer contact pad resistance is larger than the inner contact pad resistance.

As a verification, four-point probe measurements were also performed with the same samples as shown in Fig. 5.5. The result of these measurements is shown in Fig. 5.6. Note that in this case, the setup was configured so that a set current flowed through the outer contact pads, so that a voltage is measured across the inner contact pads. This is the reason that the graphs are now V(I) graphs rather than I(V) graphs. This does not change the results, however.

The resulting resistances from these measurements are 7.14×10^2 and 5.89×10^2 Ω for the first sample and the second sample shown in Fig. 5.5, respectively. These results are very close to the resistances measured using just two probes on the inner contact pads, meaning that the contact resistance is very low in these cases, and two probes are apparently sufficient to measure at least the behavior of the devices.

As a next set of measurements, shown as 3b in Fig. 5.1, a bar area was etched with the FIB through the middle of a four-point setup, to see what the effect is of etching an area, versus an outline. The same method for determining the dose was used as with the dose determination experiments. In this case, a rectangle with 1 and with 6 passes was etched. These doses were chosen to see if some conductance still occurs with slightly lower doses than theoretically calculated as necessary to completely isolate the samples. The results are shown in Fig. 5.7.

When 1 pass was used to etch the bar shape, the average resistance measured over a few structures was 5.13×10^5 Ω. In the case where 6 passes were used, the average resistance was determined to be 1.68×10^6 Ω. These results show that the samples, although they have a large resistance, are still conducting when only 1 or 6 passes are used to etch the bar. In contrast, when an I(V) curve was measured between four-point setups that were isolated using outlines, no current was measured above the noise level. This shows that the
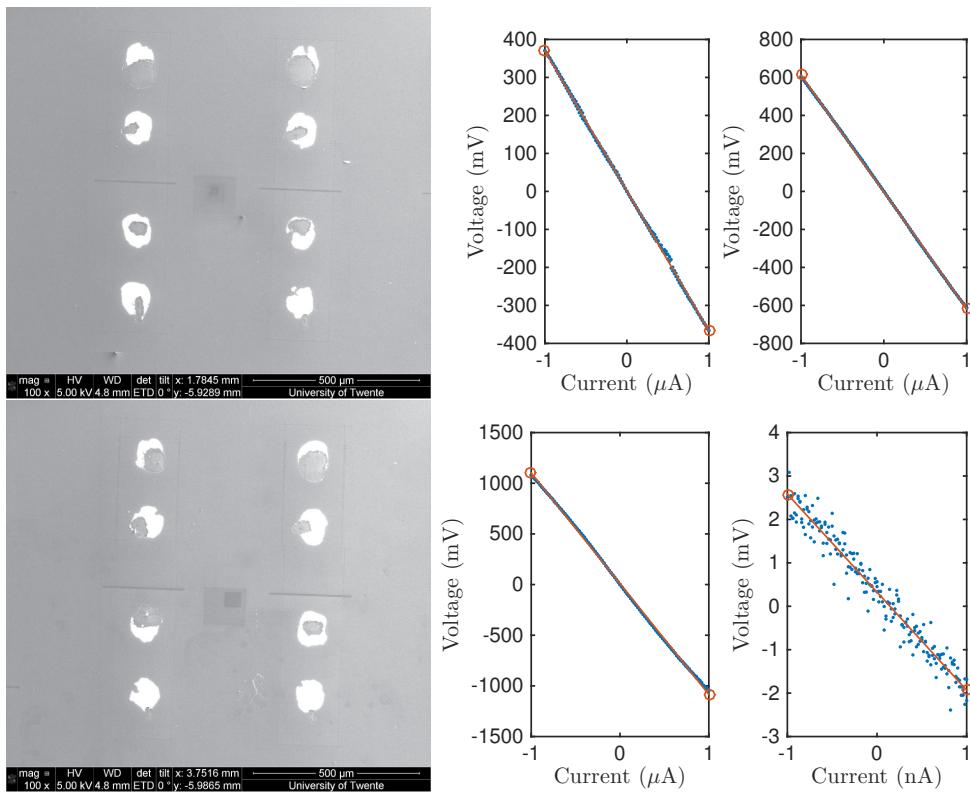
Figure 5.7: Four-point probe measurements on isolated four-point setups with a bar etched through the middle. At the top, two examples are shown where the bar was etched using 1 pass of the FIB. The bottom shows two examples where 6 passes were used.

graphene is not fully removed when using 1 or 6 passes. It must be noted that the outlines were etched with a higher dose, explaining why they do not allow conductance. In any case, this measurement does show the potential of determining the dose by doing conductance measurements, in addition to Raman measurements.

The next step of the verification measurements, 3c in Fig. 5.1, involved etching narrowings of 5 and 10 μm in the four-point setup. The hope is that the FIB has not damaged the graphene so much, that no more current can flow through. The results are shown in Fig. 5.8 for a 5 μm gap. Here, the outline structures were superimposed onto the SEM images to help see them. The outlines in the original SEM images were not very visible. The resulting resistances averaged to 1.48×10^4 Ω, and were quite consistent between samples. In comparison, when no narrowing was present, as in Fig. 5.6, the average resistance was measured to be 6.5×10^2 Ω. The width of the rectangular outline (i.e. when no narrowing is present) is approximately 180 μm, whereas the narrowing is, in this case, 5 μm. This means that the width of the narrowing is 36 times smaller than the full width of the rectangular outline. In comparison, without a 5 μm narrowing, the measured resistance is about 23 times smaller than with a 5 μm narrowing. Unfortunately then, the resistance does not scale with the ratio of the widths. However, the same measurement was also performed with a 10 μm narrowing. Here, the average resistance was determined to be 6.78×10^3 Ω, which is 2.1 times smaller than the resistance measured in the 5 μm narrowing. Coincidentally, the width is also reduced by a factor of 2.

These measurements may also allow us to approximate the sheet resistance of the graphene. The sheet resistance is defined in units of $\Omega/\square$, which indicates that the resistance of a sheet material is dependent on the shape of the region under consideration. For example, if a square sheet is taken, and a voltage is applied all along two of the edges, as shown in Fig. 5.9, then a certain resistance, R, is measured. This resistance is given by $R = R_s L/W$, where R_s is the sheet resistance of the material. This shows that if the shape is rectangular, then the measured resistance is equal to the sheet resistance. However, if the length of the material is increased by a factor 2, the measured resistance will also increase by a factor 2.

In the four-point setups used here, a voltage is not applied across the whole width of the samples, because the contact pads do not have the width of the rectangular outline. This means that the sheet resistance cannot be exactly measured. In order to make a good measurement of the sheet resistance, the contact pads would have had to cover the full width of the four-point setup. However, the narrowings are very small compared to the rest of the four-point setup, and so the assumption is made that the narrowings determine the majority of the resistance. The narrowings are 100 μm long and either 5 or 10 μm wide. This means that there is an aspect ratio L/W of 20 or 10, respectively. Therefore, the sheet resistance should be approximately a factor 1/20 or 1/10 of the resistance measured for the 5 μm narrowing and the 10 μm narrowing, respectively. Based on the resistances listed above, the resulting sheet resistances are then calculated to be 742 Ω for the 5 μm narrowing, and 678 Ω for the 10 μm narrowing. The manufacturer listed the sheet resistance of the graphene to be 450 ± 40 Ω. The note must be made that this the sheet resistance cannot be determined accurately using this setup, but since the calculated sheet resistance is close to the expected value based on the manufacturer's specifications, it can be stated that the graphene appears not to be heavily damaged as a result of etching with the FIB, which is a good sign.

The last measurements in this set involved measuring the current flowing through the graphene as a function of a gating voltage. Firstly, in this experiment, a bias voltage is applied across the inner contact pads of a four-point setup, where the four-point setup is only isolated from the bulk graphene. This bias voltage is initially set to 1 mV. As a result of this bias voltage, a current will flow through the material. Next, another probe is connected to the silicon substrate (i.e. not to the SiO_2), so that a gating voltage can be applied. This should induce an electric field in the graphene, raising or lowering the Fermi level. It is then expected that the current flowing through the graphene either increases or decreases,
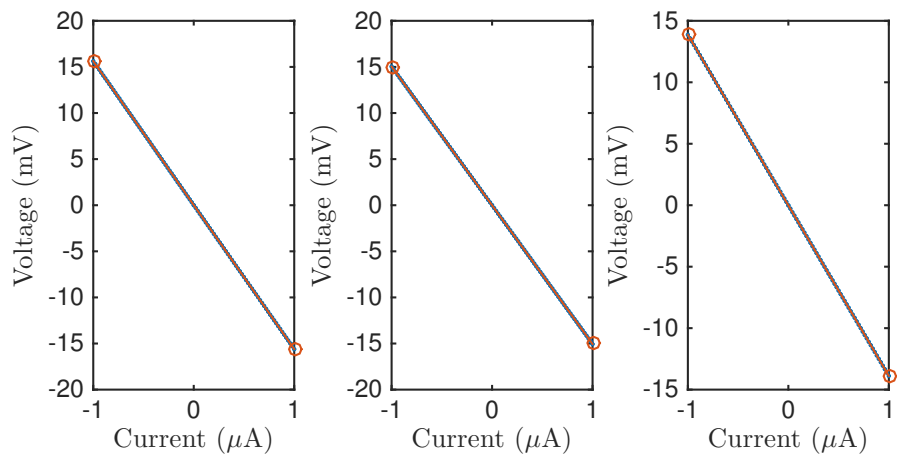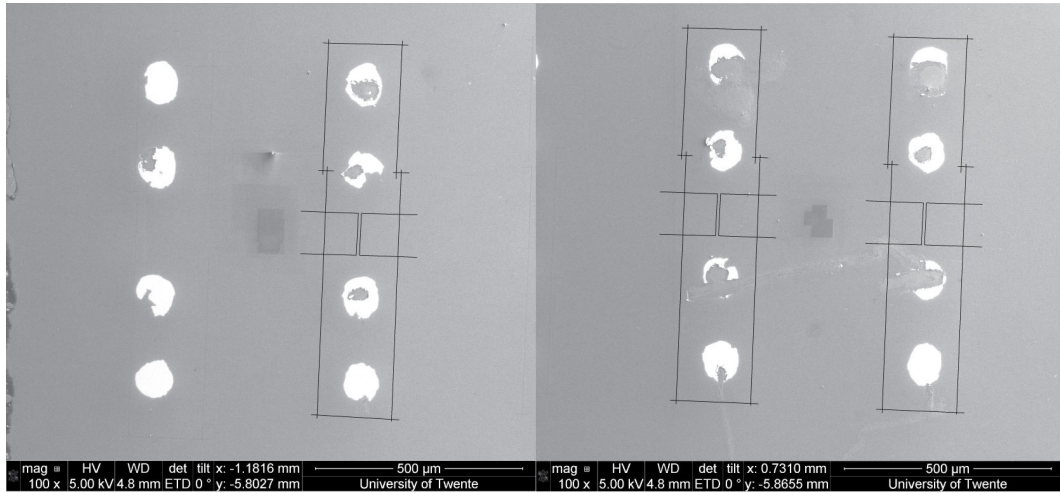
Figure 5.8: SEM images (top) and four-point probe V(I) measurements of four-point setups with 5 μm narrowings introduced. For visual aid, the outlines that were etched with the FIB have been superimposed.
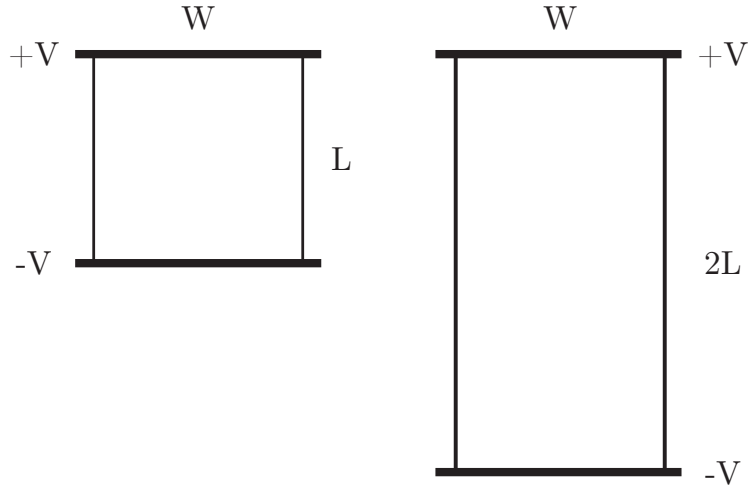
Figure 5.9: Illustration showing the working of sheet resistance. A voltage is applied across the two edges of the sheet. Increasing the length of the sheet by a factor 2, will also increase the measured resistance by a factor 2.

depending on the gating voltage, and thus Fermi level.

The results of these measurements are shown in Fig. 5.10. Initially, the bias voltage was set to 1 mV, and the gating voltage was varied between $\pm$ 10 V, starting from 0 to $-V_{max}$, back through 0 to $+V_{max}$ and then back to 0 V. As can be seen in the top left graph, not much beyond noise is measured. In the next measurement, the gating voltage was increased to $\pm$ 20 V, which made barely any difference. When the gating voltage was increased to $\pm$ 50 V, something strange happened, as can be seen in the bottom left graph. This result shows that some hysteresis appears to take place. However, the magnitude of the current is still the same as before, it is just the noise that appears to have decreased. The exact reason for this behavior is unfortunately not known. Performing the same measurement again, this time with a four-point probe configuration showed that the noise returned, however. As a result, it is expected that somehow the measurement was incorrectly performed or some cables were shifted. When the bias voltage was increased to 1.5 V, although the current flowing through the sample increased (expectedly), the noise also returned, but still showed that the magnitude does not change visibly as a result of the gating voltage. These results show that the gating voltage appears to have no effect on the current flowing through the graphene. Upon further inspection, it turns out that the Si/SiO$_2$ substrate used in this case has an SiO$_2$ layer that is about 300 nm thick. This layer is much thicker than normally used in gating experiments, where thicknesses of around 50 nm or less are used. This means that the electric field cannot penetrate far enough into the SiO$_2$ layer to reach the graphene. Increasing the gating voltage is dangerous, because other effects can start to play a role. For these samples, gating experiments can therefore not be performed.

Fabrication of diodes

As a final step in the research project, geometric diodes were fabricated, which were then measured using a probe station. A few types of geometric diodes were made. First, diodes were made with a neck width of 30 or 50 μm, and second, diodes were made with two diodes in a row, with neck widths of 30 or 50 μm. In all of the designs, the slope had an angle of 45 degrees.

The results of the diode with a neck width of 50 nm are shown first, in Fig. 5.11. At the top part of the figure, the SEM images of the samples are shown, and at the bottom part, the
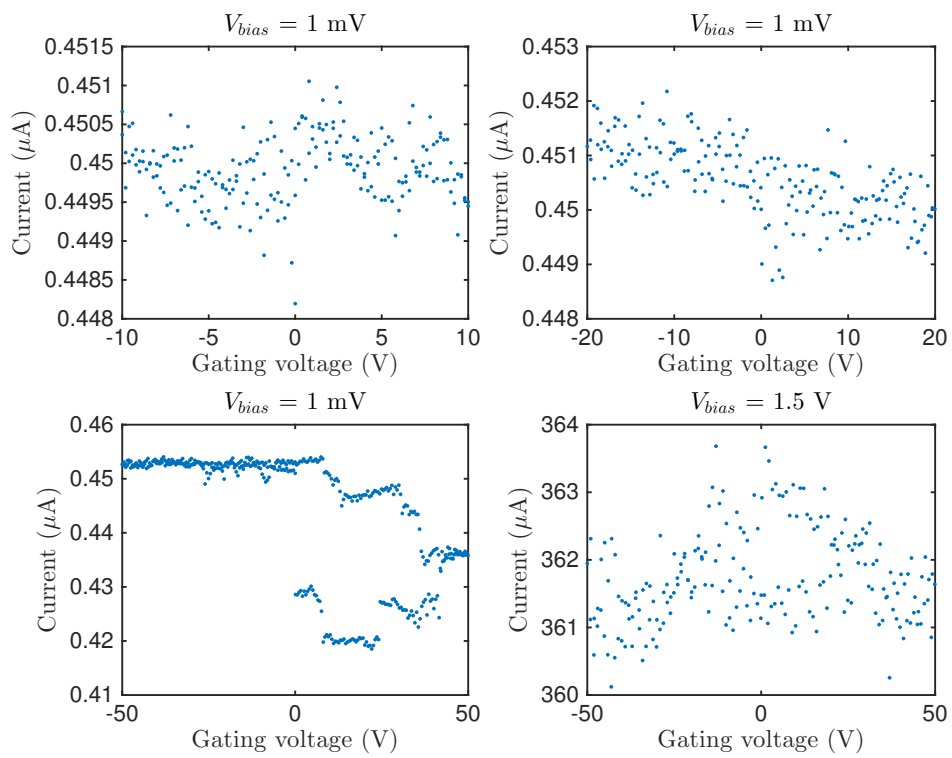
Figure 5.10: I(V) measurements for a fixed bias voltage V_{bias} applied across the inner contact pads of a four-point setup, for varying gating voltage.

two-probe I(V) measurements are shown. A few things are immediately apparent. First of all, the I(V) response is no longer linear, for any of the structures. A test measurement was done elsewhere on the sample, where no diodes were made, and this showed the characteristic linear response for the same applied bias voltages. This is therefore the first clear indicator that devices have been made with nonlinear I(V) responses. However, the second thing to note is that the I(V) curves seem to be fairly symmetric. The close observer may note that the curve for diode 1 seems to be slightly asymmetric, but the same does not appear to be true for diodes 2 through 4. Furthermore, the amplitude of the responses differs quite a bit between samples.

An important factor to consider, is that the graphene used here is made using the CVD technique. This means that the graphene has so-called grains, which in this case are typically 10 μm in diameter. At the boundaries between grains, the graphene is certainly not uniform, and therefore electrons will likely not travel very freely across those boundaries. If such a boundary happens to lie exactly at the geometric diode shape, then the reflection at the diode will not be perfect and the diode may have a decreased performance. This could explain why in some cases the diode does seem to work, while in others it does not work as well. This can easily be verified by making SEM images of the samples after measurements were done. However, measurements should not be done beforehand, as the SEM too can damage the samples, as discussed previously.

In Fig. 5.12, measurements are shown for diodes with a neck width of 30 nm. In this case, the results vary even more, although in one of the diodes, nonlinear behavior can still be observed. The magnitude of the current for one of the diodes seems to be comparable to the current flowing through diodes with a neck size of 50 nm. However, no conclusions can be made certain, since the magnitude of the currents vary significantly between diode shapes. It may well be that the current is, on average, smaller or higher for smaller or larger diodes, but further inspection of the samples is needed to be more certain. It is expected that the variation between the measurements is due to defects in the graphene, causing the electrons to be obstructed around the neck shape. Further inspection with the SEM should be done to check this.

As two last measurements, the diode shapes were duplicated, so that two diodes followed each other in line. Such structures were made for both a 50 nm neck width and a 30 nm neck width and are shown in Fig. 5.13 and Fig. 5.14 for 30 nm neck width and 50 nm neck width, respectively. These results show that the current is again comparable in magnitude to that seen before, and also shows that some of the diodes did not seem to work as well. In this case, since two diodes follow each other, the chance that there is a defect in one of the necks is higher, meaning that it is more likely that the diode does not work. Still, in two cases, the diodes do seem to conduct, albeit less than what was measured for single diodes. From these measurements, it would appear that duplicating diodes reduces the current flowing through the device, which can be expected, but it does not seem to create more asymmetry between forward and backward current, either.

Taken together, the measurements leave a few questions unanswered. The nonlinear response seems to suggest that the geometry of the devices may indeed have an influence on the current flowing forward or backward. However, the asymmetry, or lack thereof, raises more questions. It may be that the grain size of the graphene is too small. Another cause may be that the FIB does in fact damage the graphene around the neck sufficiently for the electrons not to be able to reflect (specularly), or it may be that the MFPL is reduced because defects are introduced. Further inspection with the SEM is desired, as well as more diode structures, perhaps even using graphene samples that are more pure, i.e. have a larger MFPL. It may also be that the slope of the diodes is not perfect. The simulations performed earlier seemed to suggest that the slope of the diodes has a significant impact on the characteristics. In any case, the measurements do show that the fabrication process is clearly able to make samples in graphene with high precision.
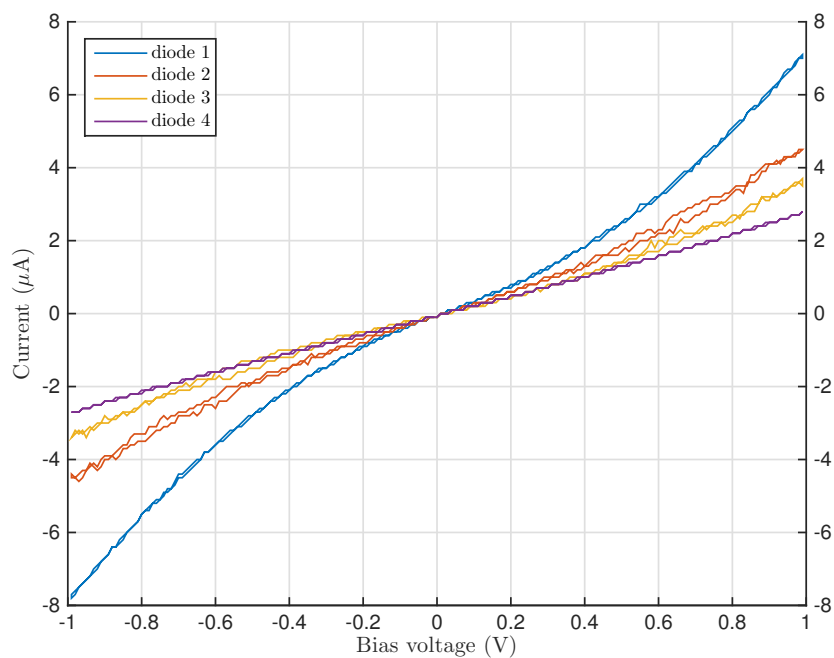
Figure 5.11: I(V) measurements for diodes with a neck width of 50 nm. The top images are SEM images acquired before the I(V) measurements and correspond to the I(V) curves shown below.
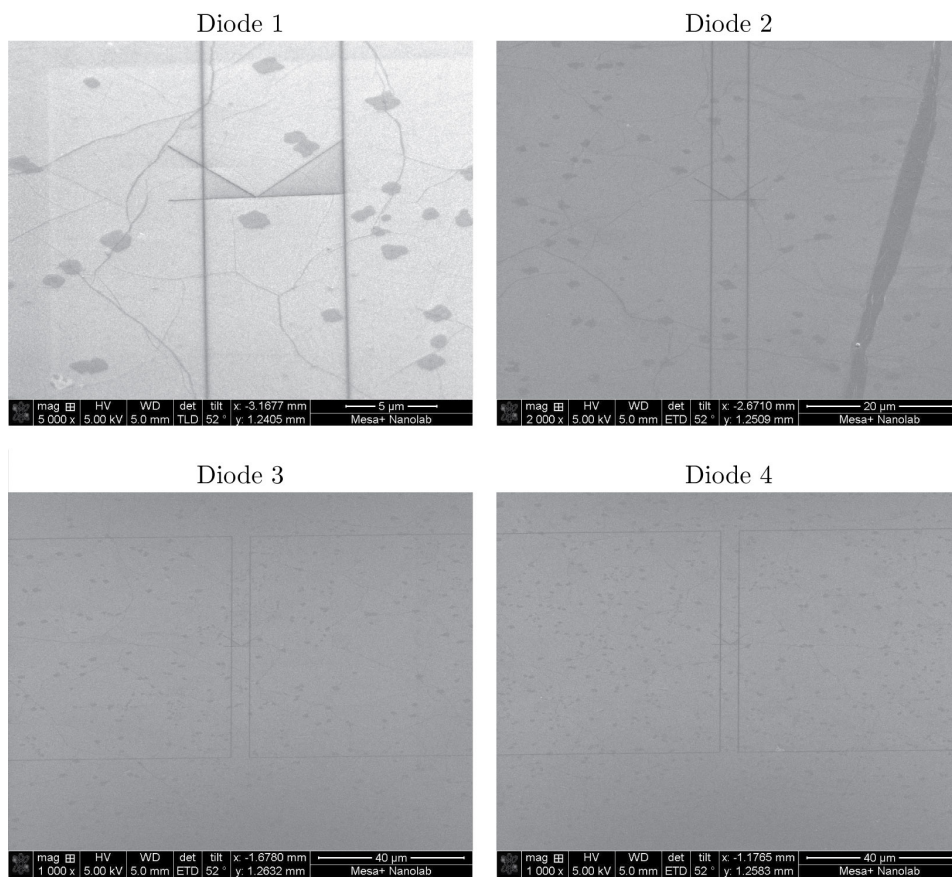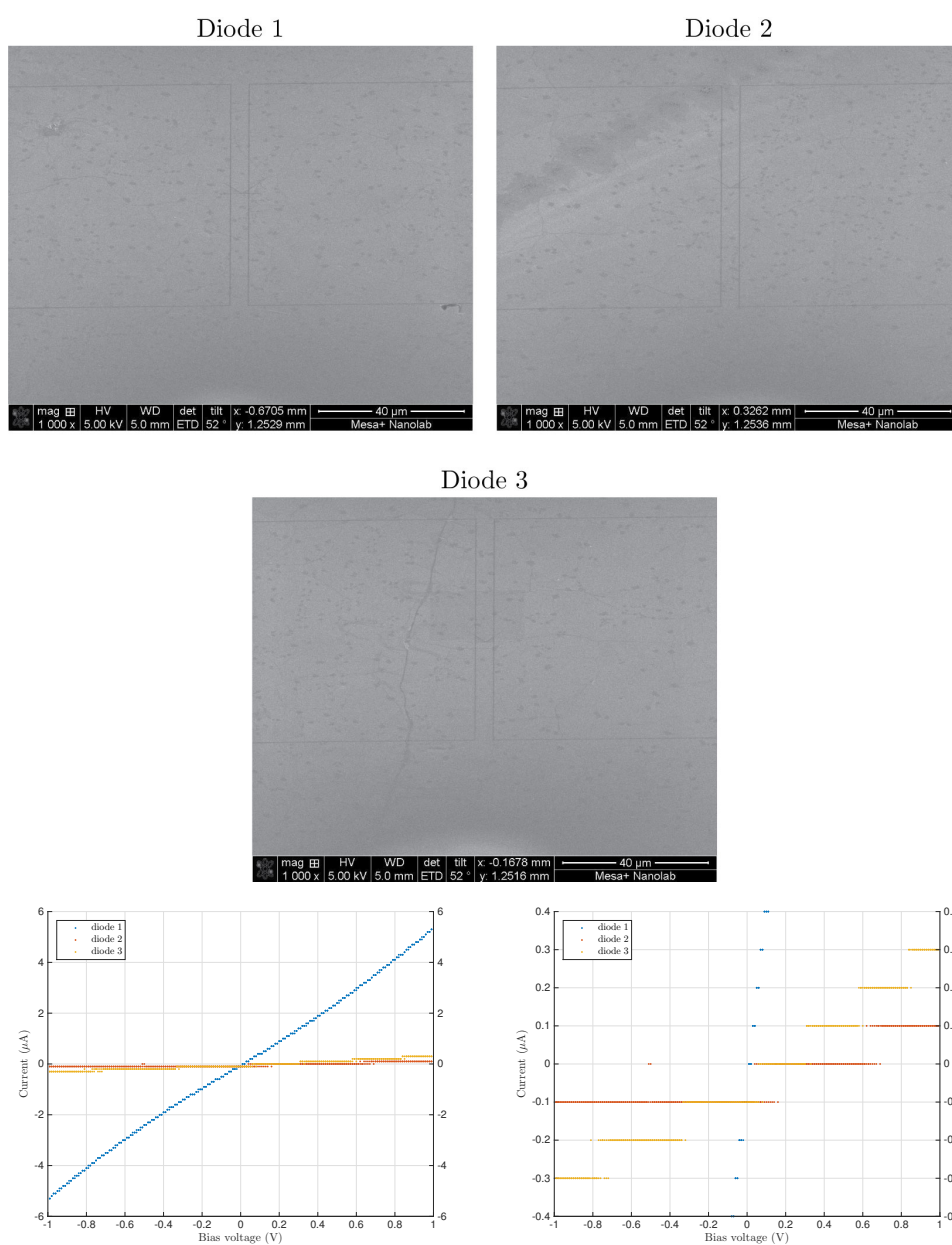
Figure 5.12: I(V) measurements for diodes with a neck width of 30 nm. The top images are SEM images acquired before the I(V) measurements and correspond to the I(V) curves shown below. The right graph is zoomed in on the left graph to show more detail.

Diode 1

Diode 2

Figure 5.13: I(V) measurements for double diodes with a neck width of 30 nm. The top images are SEM images acquired before the I(V) measurements and correspond to the I(V) curves shown below. The right graph is zoomed in on the left graph to show more detail.
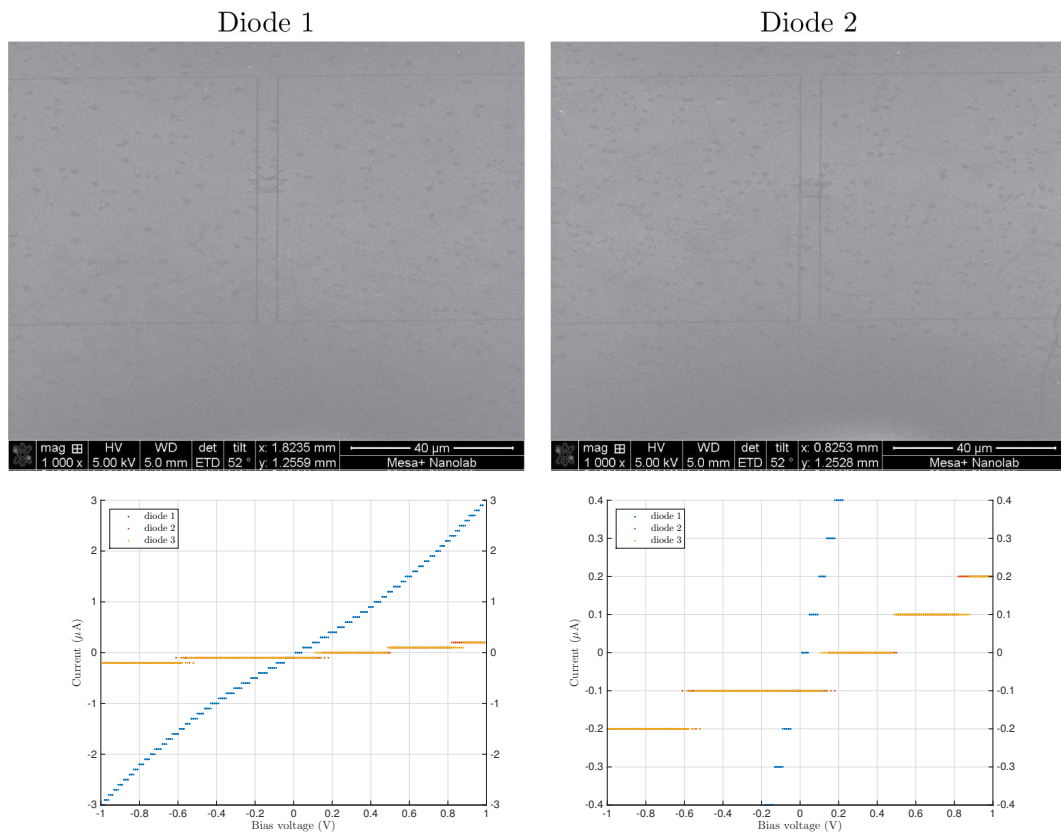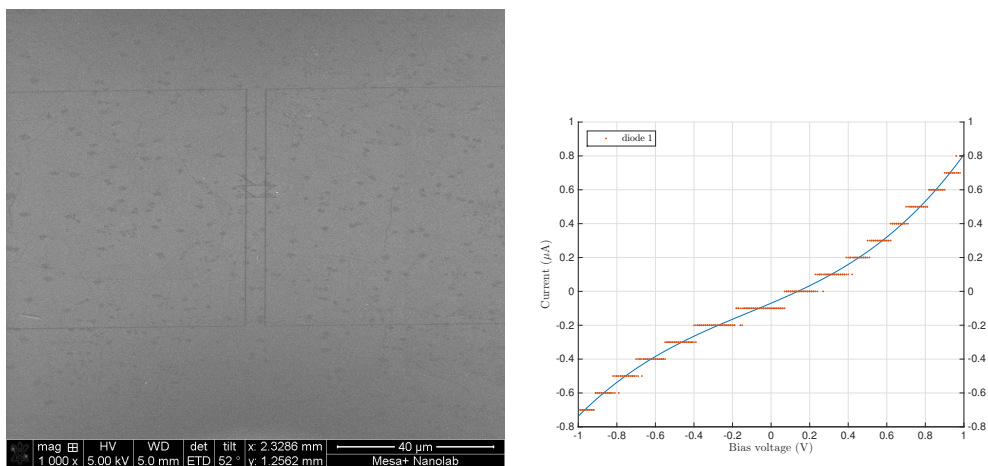

Figure 5.14: I(V) measurements for double diodes with a neck width of 50 nm. The left image is an SEM image acquired before the I(V) measurement and corresponds to the I(V) curve shown to the right.

Chapter 6

Conclusions and discussion

6.1   Conclusions

The goal of the research project was to investigate a new type of solar cell using a single 2D material, such as graphene, patterned to work as an optical antenna and as a diode. Such a device forms a rectenna, in which light is coupled to electrons, producing an alternating current in the graphene. This current is then rectified using a geometric diode, again made from graphene, to produce direct current. This new technique for solar energy harvesting, called solar rectification, is shown to be based on the ballistic behavior of electrons in a 2D material, so that the geometry of the material influences the movement of electrons in a controllable way. In this research project, a theoretical study was performed, and geometric diodes were designed, fabricated and analyzed to investigate the feasibility of this new technique.

As a first step, a simulation model was made to analyze and, in the future, optimize the geometric diode shape. The model serves as a starting point for more advanced simulations, and allows an arbitrary geometric diode shape to be defined in order to analyze its performance. Simulations were done with this model to investigate the effects of, for example, the neck width, shoulder width and the slope angle of a geometric diode. From these simulations, it was shown that the neck size and slope angle have a large impact on the performance of geometric diodes. Suggestions were also made how this model could be improved to yield more realistic results. Combined with experimental data, this model can provide insight and help with the design process of geometric diodes.

Since samples were going to be etched using a Focused Ion Beam, experiments were performed to determine the optimal gallium ion dose in a FIB, so that the graphene can be etched while causing minimal collateral damage in the graphene. Square areas were etched with the FIB, while the ion dose was increased between squares. A confocal Raman spectroscopy setup was then used to analyze the effects of the FIB. Single Raman measurements, line scans and image scans showed clearly that the graphene was damaged more as the dose increased. For better understanding, a program was developed to create hyperspectral images from the resulting image scan data. The combined Raman data then made it possible to determine the optimal FIB dose to use in the final fabrication. It was suggested that etching outlines instead of areas would also likely decrease the amount of damage, while achieving the same goals.

A fabrication process was developed to create geometric diodes in graphene. Graphene samples were prepared by depositing metal contact pads in a matrix of four-point probe configurations on a graphene sample. To this end, a mask was designed and created that could be used to control where metal was deposited in a thermal vapor deposition system. The samples were analyzed using an SEM to inspect the deposition results. Next, it was

found that the FIB could not be used to look at the graphene while patterning, as this would damage the graphene significantly. To solve this, a protocol was developed, to make the SEM and the FIB work in unison. The SEM was used to look at the sample, and the SEM and FIB beams were aligned so that etching could be done blindly. With this fabrication protocol, several samples were prepared to investigate the influence of etching on the graphene. Samples were prepared where contact pads were isolated, and where narrowings had been introduced. These samples were then measured electrically using a probe station, which showed that the FIB could successfully isolate samples electrically, without damaging the graphene too much.

Finally, several geometric diodes were produced with the FIB. These diodes had 30 and 50 nm neck widths, and were placed in single or double configurations. Probe station measurements showed clear nonlinear behavior in the I(V) responses, meaning devices have been created and they are conducting electricity. The behavior appeared to be more symmetric than asymmetric, however, and also showed relatively large variation in magnitude. It can therefore not be concluded with certainty that geometric diodes have been created. More measurements will be necessary to verify that. It does show, however, that the fabrication protocol produces reproducible results, which opens up the opportunity to create better samples in the future, with the use of higher quality graphene.

6.2 Discussion and outlook

As is common in research, there are always questions unanswered or room for improvement. In this section, some important discussion points will explained and future points of interest will be discussed.

Although a few discussion points about the simulation model were already listed in chapter 2, we will discuss some of them briefly here as well. Due to limited time, there was unfortunately no more time to run simulations to compare the measurements performed with the fabricated geometric diodes to the simulation model. However, a few conclusions can already be drawn about the simulation model and the measurements. The measurements do not match the expected behavior based on the simulations as shown in, for example, Fig. 2.6. The behavior there shows two distinct linear regimes, whereas the behavior here is more symmetric. However, as discussed in chapter 2, the simulation model is a very basic simulation model, where assumptions were made that limit the accuracy of the model. For example, electron-electron interactions were neglected which, in bulk materials, might yield acceptable results. In the case of a 2D material, and especially around the edge of a 2D material, this likely yields inaccuracies. Furthermore, the electrons are assumed to move in straight lines, without accelerations taken into account. Reflections also do not take into account the electric field that was applied. All of these assumptions may lead to significant errors in the simulation model. For that reason, it would be interesting to see the impact of those assumptions on the simulation model. It would in any case be advisable to improve the simulation model by including these effects, as then the model can be used to predict the effects of the shape on the performance of the diode.

In the process of determining the optimal ion dose for the FIB, experiments were only performed where square areas were etched, after which Raman measurements were done to determine how much the graphene was damaged (or not). However, it was determined afterwards that it would be better to etch using outlines, rather than areas. It makes sense then to repeat the measurements to investigate the influence of line scans versus area scans. One of the experiments that could be performed involves etching parallel lines, say, 100 μm apart, and sufficiently long (e.g. 0.5 mm), where the ion dose is increased between each successive line. Then, a Raman line scan with the confocal Raman microscope could be made perpendicular to these lines. By then plotting the ratio of the peak heights of the 2D, G or D peaks of graphene, one should be able to see that the damage in the graphene

increases close to an etch line, and decreases farther away from it, and that the damage should decrease with decreasing ion dose. This could give insight in how far from the lines the graphene is still damaged, and should show at which dose the damage becomes visibly present. However, even though it is a nice comparison to the experiment with square areas, it also comes with an important limitation. Since the lines are much thinner than the focal volume of the Raman microscope, the spectrum will always be an average of the graphene around the line. A much better experiment in that case is to take a graphene sample with many contact pads. These contact pads could be isolated from other contact pads close to them with the FIB, while using various ion doses. If the contact pads are not isolated, current will readily flow, but if the dose is increase, the resistance of the graphene should go up until no conduction takes place. Since we are interested in electrically isolating graphene, this may be a better experiment.

As shown in the fabrication chapter, the gold contact pads had less leakage than the palladium contact pads. It was noticed that the mask for thermal vapor deposition was warping slightly. The actual mask material is only 0.1 mm thick, and apparently stress in the material led it to wrap whenever it is not firmly attached. The mask was attached to the spacing ring using adhesive tape, but it was noticed after deposition that the tape has come loose slightly. This may be the reason why the contact pads have spread out slightly more. It might prove useful to make sure that the mask is firmly attached whenever new samples are made. Another issue with the masks is that the laser cutter had a limited resolution, meaning that the contact pads could not be made smaller inside than 100 μm. If more complicated contacts need to be deposited, this method is therefore not useful. In that case, it might probe to be better to use lithography, or e-beam assisted growth to grow contacts. In the current fabrication process, it was furthermore necessary to first deposit the contact pads before patterning the graphene, because the mask could not be placed precisely on the sample. For most of the experiments, this was more than sufficient, but if the sheet resistance needs to be determined, the contact pads need to cover the full width of the rectangular outline. This could be achieved by using alternative production methods, such as e-beam assisted growth. Lastly, it was found that gold contact pads were much weaker than palladium contact pads. It would be advisable to keep using palladium in the future, as it turned out to be able to withstand the probes much better.

Gating experiments were not possible using our samples, because the oxide layer was too thick for the electric field to penetrate far enough. The oxide layer of our samples was about 300 nm, whereas a thickness of less than 50 nm is desired. If possible, it would be a good idea to find a sample that has a less thick oxide layer, so that gating experiments could be performed, as this may provide insight and could potentially even be necessary for diode operation. This does however require that the graphene is either transferred from the current Si/SiO_2 samples, or that new samples are ordered. A sample with graphene on top of a copper substrate was made available to us by Applied Nanolayers, which could be used for this purpose. Additionally, this sample promised a much higher quality compared to the Graphenea sample, which means that the expected MFPL is higher, meaning the diode characteristics should improve as well.

An interesting question that remained unanswered is whether the absorption of light in graphene should be considered classically, or quantum mechanically. For example, in appendix C, the electric field of sunlight is calculated, assuming sunlight is described as a classical electromagnetic field, and the displacement of an electron as a result of this electric field is calculated. In that case, even if an electron is assumed to have a mass of 0.02 m_e, which is achievable around the Dirac point, the electron would be displaced just 10^{-15} m during one optical cycle, which is an incredibly small displacement. In other words, the electron would hardly move in the classical description, meaning a geometric diode would not work. Another option is that one electron absorbs one photon, in which case e.g. a 500 nm wavelength photon has an energy of 2.48 eV, which seems like an incredible amount for

a single electron. Although it was not necessary during this research project to know, it would be interesting to know what the actual physical process is that would take place in an antenna.

Although some very nice results were achieved, the work presented in this thesis is not yet finished. For example, we have not been able to make antennas and couple them to the graphene to attempt to make rectennas. It is also not yet certain that geometric diodes have actually been made. Therefore, a lot of work still remains for future research, which offers many exciting opportunities for future students. An example includes simulating antenna behavior. In this case, an FDTD solution is typically used. However, it is difficult to simulate the graphene in such solvers, since the theoretical thickness of graphene is 0.345 nm. Simulations cannot easily be made where light around 500 nm is simulated as well as a material with such a small thickness. Therefore, some tricks need to be performed. It was found that some simulations exist already in packages like Lumerical, that seem to open up the possibility for simulating graphene this way. In that case, antenna design could perhaps be done in such packages. This is something that could still be done in the future.

The last challenge is to improve the quality of the graphene. It is likely that as time moves on, the quality of graphene will improve drastically. It is expected that as the purity of the graphene improves, so will the performance of the geometric diodes and rectennas. Especially for a proof of concept device, it may therefore be wise to move to more pure graphene samples as the project moves on.

Acknowledgements

During the past few years, I have been lucky to work with some fantastic people, without whom the work presented in this thesis would not have been possible, and without whom my time as a student would not have been as great as it has been. Words always fall short of expressing my gratitude, but I would still like to take this opportunity to try and thank those people that have helped me in one way or another.

First off, I would like to thank Frans Segerink for his excellent help with the fabrication of the samples used in this work. Frans showed real dedication for perfecting the fabrication method and was always open to discussions and questions, and of course provided the perfect audio system for Beer O' Clocks. Together with Frans, I believe we have created a very nice protocol for fabricating samples, which I hope can be used in the future as well.

The Raman measurements were done in two sessions, one using the confocal Raman setup from the Medical Cell Biophysics (MCBP) group, and the other with the confocal Raman setup in the BioNanoLab at the University of Twente. From MCBP, I would like to express my thanks to Frank Timmermans and Aufried Lenferink for allowing me to use the setup, helping me with the measurements and understanding the spectra. In the BioNanoLab, I was helped by Pablo Muñoz, who, beside helping with the Raman measurements, was always happy to help whenever I had questions.

The probe station measurements were done in two research groups that generously allowed me to use their probe stations and helped me by explaining and setting up the experiments. The first set of measurements were done at the NanoElectronics group, led by prof. dr. ir. Wilfred van der Wiel, with the help of Matthias Brauns and Joost Ridderbos. The second set of measurements were done with the probe station from Transducers Science and Technology, with the help of Thijs Bolus and Remco Sanders. I am very grateful for the kindness and support from both groups, and for answering the many questions I had.

I would also like to thank dr. Ageeth Bol, and her PhD students, who answered many questions regarding the fabrication process. During the research project, we visited her group with questions about the theory and fabrication of graphene samples. Their input and discussions helped us greatly in achieving the final results. For the more theoretical aspects, I would like to thank prof. dr. Mikhail Katsnelson, prof. dr. Annalisa Fasolino and dr. Shengjun Yuan, who were also very kind in answering some of our questions. One of the graphene samples was generously donated to us by Richard van Rijn, from Applied Nanolayers. It is my hope that we will be able to use this sample in the future to create even higher quality devices.

Of course my thanks also go out to my graduation committee, composed of my supervisor dr. ir. Herman Offerhaus, who is the chairman of the committee, and prof. dr. Jennifer Herek from Optical Sciences, prof. dr. ir. Wilfred van der Wiel from NanoElectronics and prof. dr. ir. Harold Zandvliet from Physics of Interfaces and Nanomaterials. Thanks to Herman for offering me this really fun and challenging project and guiding me through it. What started out as a interesting concept, turned out to be a really multidisciplinary, educational and fun experience. Thanks to Jennifer for always being motivational and supportive, and for leading such a fun group of people. I would also like to thank Wilfred

and Harold for their involvement, not only for being part of my committee, but also for being great teachers during my education and always being open for questions.

For the past year, I have been lucky to be part of a great group of people, who work together closely and have fun while doing so. From my Bachelors project to the Experimental Laser Physics and Nonlinear Optics course and finally my Masters thesis, each period spent there, I have learned new things and had fun. The dog fights with RC helicopters, the retreats and the Beer O' Clocks, they are just a few examples of fun experienced at the Optical Sciences group. You are too many to list, but thank you all for the awesome experience and the fun!

Of course I would also like to thank all of my friends for their support. Some I have known for a long time now, some since a little later, but I am very happy to have met and still know all of you. Thanks also to Tartaros, the survival running group, who have taught me that, although there is no gain without pain, it can still be fun! And thanks to Faalaap for being an awesome group of people, with whom I have always had fun. I will see you guys on Wednesday!

Last, but certainly not least, thanks to my family and my girlfriend for their continuing support and love, which guided me through good times and bad.

Bibliography

[1] Willson, R. C., and A. V. Mordvinov, "Secular total solar irradiance trend during solar cycles 21–23", Geophys. Res. Lett., vol. 30, no. 5, 1199, 2003.

[2] ITACA, "The Sun As A Source Of Energy", retrieved online from http://www.itacanet.org/the-sun-as-a-source-of-energy/part-2-solar-energy-reaching-the-earths-surface/spec/ on 9 March 2015.

[3] H. Mashaal et al., "First direct measurement of the spatial coherence of sunlight", Opt. Lett., vol. 37, issue 17, pp. 3516-3518, 2012.

[4] S. Divitt and L. Novotny, "Spatial coherence of sunlight and its implications for light management in photovoltaics", Optica, vol. 2, no. 2, 2015.

[5] Newport Corporation, "Introduction to Solar Radiation", retrieved online from http://web.archive.org/web/20131029234117/http://www.newport.com/Introduction-to-Solar-Radiation/411919/1033/content.aspx on Mar 11, 2015.

[6] Lawrence Berkeley National Laboratory, "Cool Colors Project: Improved Materials for Cooler Roofs", retrieved online from http://eetd.lbl.gov/newsletter/nl19/ on Mar 9, 2015.

[7] SolarGIS © 2015 GeoModel Solar, "World Map of Global Horizontal Irradiation", retrieved online from http://solargis.info on Mar 10, 2015.

[8] World Energy Council and Enerdata, "Average electricity consumption per electrified household", retrieved online from www.wec-indicators.enerdata.eu on Mar 10, 2015.

[9] W. C. Brown, "The history of power transmission by radio waves," IEEE Trans. Microwave Theory Tech., vol. MTT-32, pp. 1230–1242, 1984.

[10] A. Hagerty et al., "Recycling Ambient Microwave Energy With Broad-Band Rectenna Arrays", IEEE Tans. Microwave Theory Tech., vol. 52, no. 3, pp. 1014-1024, 2004.

[11] C. Kittel, "Introduction to Solid State Physics", Wiley, 8th edition, 2005.

[12] R. Dalven, "Introduction to Applied Solid State Physics", Springer US, 1990.

[13] P. Bharadwaj, B. Deutsch and L. Novotny, "Optical Antennas", Advances in Optics and Photonics, vol. 1, issue 3, pp. 438-483, 2009.

[14] S. Grover, G. Moddel, "Applicability of Metal/Insulator/Metal (MIM) Diodes to Solar Rectennas", IEEE J. Photovolt., vol. 1, no. 1, pp. 78-83, 2011.

[15] T.M. Razykov et al., "Solar photovoltaic electricity: Current status and future prospects", Solar Energy, vol. 85, no. 8, pp. 1580-1608, 2011.

[16] Fraunhofer Institute, "Photovoltaics report", retrieved online from http://www.ise.fraunhofer.de/de/downloads/pdf-files/aktuelles/photovoltaics-report-in-englischer-sprache.pdf on Mar 10, 2015.

[17] A. De Vos, "Detailed balance limit of the efficiency of tandem solar cells", J. Phys. D: Appl. Phys., vol. 13, issue 5, pp. 839-846, 1980.

[18] W. Shockley and H. J. Queisser, "Detailed Balance Limit of Efficiency of p-n Junction Solar Cells", J. Appl. Phys., vol. 32, pp. 510-519, 1961.

[19] G. Moddel, S. Grover, "Rectenna Solar Cells", Springer Science+Business Media, New York, 2013.

[20] B. J. Eliasson, "Metal-Insulator-Metal Diodes For Solar Energy Conversion", PhD thesis, accessed online at http://ecee.colorado.edu on Mar 12, 2015.

[21] N.W. Ashcroft, N.D. Mermin, "Solid State Physics", New York: Holt, Rinehart and Winstom, pp. 2-11, 1976.

[22] Z. Zhu et al., "Graphene geometric diodes for terahertz rectennas", J. Phys. D: Appl. Phys., vol. 46, no. 18, 2013

[23] G. Moddel et al., "Ultrahigh speed graphene diode with reversible polarity", Solid State Comm., vol. 152, pp. 1842-1845, 2012.

[24] P. Zhang and D. M. H. Hung, "An analytical model for ballistic diode based on asymmetric geometry", J. Appl. Phys., vol. 115, 2014.

[25] J.R. Black, "Electromigration - A Brief Survey and Some Recent Results", IEEE Trans. on Electron Devices, vol. 16, no. 4, pp. 338–347, 1969.

[26] A.H. Castro Neto et al., "The electronic properties of graphene", Dev. Mod. Phys., vol. 81, no. 1, pp. 109-162, 2009.

[27] K.I. Bolotin et al., "Ultrahigh electron mobility in suspended graphene", Solid State Communications, vol. 146, pp. 351–355, 2008.

[28] R. Murali et al., "Breakdown current density of graphene nanoribbons", Appl. Phys. Lett., vol. 94, 2009.

[29] Wallace, P. R., "The band theory of graphite", Phys. Rev., vol. 71, 622, 1947.

[30] B. Bhushan, "Scanning Probe Microscopy in Nanoscience and Nanotechnology 2", Springer, 2011.

[31] R. S. Deacon et al., 'Cyclotron resonance study of the electron and hole velocity in graphene monolayers", Phys. Rev. B, vol. 76, 2007.

[32] S. Reich et al., "Tight-binding description of graphene", Phys. Rev. B, vol. 66, 2002.

[33] J. H. Chen et al., "Intrinsic and extrinsic performance limits of graphene devices on SiO2", Nature Nanotechnology, vol. 3, 2008.

[34] S. V. Morozov, "Giant Intrinsic Carrier Mobilities in Graphene and Its Bilayer", Phys. Rev. Lett., vol. 100, 2008.

[35] Ioffe, "Electrical properties of Silicon", retrieved online from http://www.ioffe.rssi.ru/SVA/NSM/Semicond/Si/electric.html on Mar. 18, 2015.

[36] E.H. Sondheimer, "The mean free path of electrons in metals", Advances in Physics, vol. 1, Issue 1, 1952.

[37] T. Altanhan, B. Kozal, "Impurity effects in graphene", Eur. Phys. J. B, vol. 85, 2012.

[38] K.S. Novoselov et al., "Electric Field Effect in Atomically Thin Carbon Films", Science, vol. 306, 2004.

[39] S. A. Maier, "Plasmonics: Fundamentals and Applications", Springer, 2007.

[40] C. Kittel, "Introduction to Solid State Physics", 8th ed., Hoboken, NJ: John Wiley & Sons, 2004.

[41] S. A. Maier and H. A. Atwater, "Plasmonics: Localization and guiding of electromagnetic energy in metal/dielectric structures", J. Appl. Phys., vol. 98, 2005.

[42] V. Giannini et al., "Plasmonic Nanoantennas: Fundamentals and Their Use in Controlling the Radiative Properties of Nanoemitters", Chem. Rev., vol. 111, 2011.

[43] F. H. L. Koppens, D. E. Chang and F. J. G. de Abajo, "Graphene Plasmonics: A Platform for Strong LightMatter Interactions", Nano Lett., vol. 11, 2011.

[44] J.M. Jornet, I. F. Akyildiz, "Graphene-based Plasmonic Nano-Antenna for Terahertz Band Communication in Nanonetworks", IEEE Journal On Selected Areas In Communications /Supplement, vol. 31, no. 12, 2013.

[45] N. W. Ashcroft; N. David Mermin, "Solid State Physics", Saunders College. pp. 6–7, 1976.

[46] P. Drude, "Zur Elektronentheorie der metalle", Annalen der Physik, vol. 306, 1900.

[47] I. Childres et al., "Effect of oxygen plasma etching on graphene studied using Raman spectroscopy and electronic transport measurements", New Journal of Physics, vol. 13, 2011.

[48] A. C. Ferrari and D. M. Basko, "Raman spectroscopy as a versatile tool for studying the properties of graphene", Nature Nanotechnology, vol. 8, 2013.

[49] L.M. Malarda, M.A. Pimenta, G. Dresselhaus and M.S. Dresselhaus, "Raman spectroscopy in graphene", Physics Reports, vol. 473, pp. 51–87, 2009.

[50] Liliana Burakowski Nohara et al., "Evaluation of Carbon Fiber Surface Treated by Chemical and Cold Plasma Processes", Materials Research, vol. 8, no. 3, 281-286, 2005.

Appendices

Appendix A

Graphene datasheet

Graphenea

Product Datasheet

Graphenea Monolayer Graphene film on various substrates

Graphene Film

Growth Method	CVD synthesis
Transfer Method	Clean transfer method
Quality Control	Optical Microscopy & Raman checked
Appearance (Color)	Transparent
Transparency	>97%
Appearance (Form)	Film
Coverage	>95%
Number of graphene layers	1
Thickness (theoretical)	0.345 nm
Field Effect Mobility on SiO_2/Si	2,000 cm^2/V·s
Hall Effect Mobility on SiO_2/Si	4,000 cm^2/V·s
Sheet Resistance	350 Ohms/sq.
Grain size	Up to 10 µm

Substrates

	Si	SiO_2/Si
Type/Dopant	P/Bor	P/Bor
Orientation	<111>	<100>
Growth Method	CZ	CZ
Resistivity	1-30 ohm cm	<0.005 ohm cm
Thickness	525 +/- 25 µm	525 +/- 20 µm
Front Surface	polished	polished
Back Surface	etched	etched
Flats	2 SEMI	2 SEMI
Coating	--	300 nm thermal oxide on BOTH wafer sides

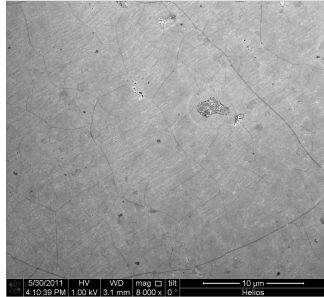| Cu foil		Quartz	
Thickness	18 µm	Flatness	bow: 20um; Warp: 30um
		Roughness	6 Å (polished side)
		Polished	Double side polished

www.graphenea.com
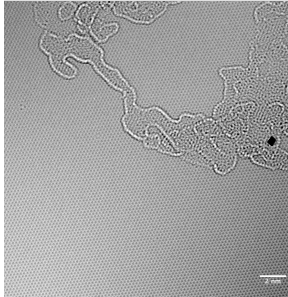
91

Optical Microscopy

Raman Spectrum
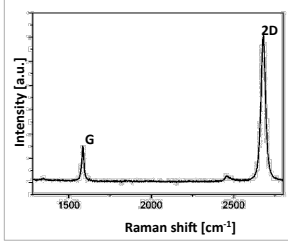
SEM image

HRTEM image

Appendix B

FIB damage

To show the effect of the FIB on graphene samples in a more illustrative way, the FIB was programmed to take 11 images using the FIB at 3500 times magnification, at 90 pA ion current. The resulting images in Fig. B.1 clearly show the damage done to the graphene as it is exposed to the FIB in just a few passes. This illustrates the importance of reducing the ion dose to the minimal value required and why the FIB cannot be used to image the sample, while patterning.
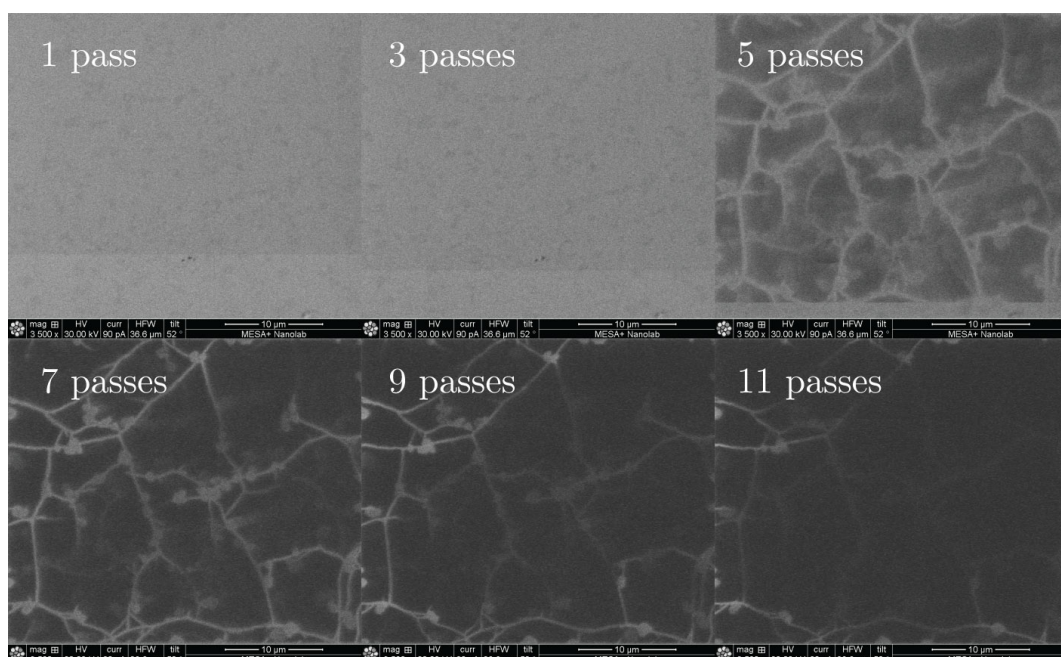
Figure B.1: The effect of the FIB on graphene. The FIB was used to make about 11 sequential images at an ion current of 90 pA, at 3500 times magnification.

Appendix C

Electron movement in the classical description of sunlight

One theory behind how a geometric diode could work involves assuming that the electromagnetic field of sunlight directly drives the electrons in the graphene back and forth, as if the sunlight was an oscillating electric field applied across the diode. In this appendix, the displacement of an electron is calculated when sunlight is considered to be a classical (electromagnetic) field. The assumption is made that sunlight has an irradiance of around 1 kW per m^2 on the surface of the earth. The irradiance of an electric field field is defined as

$$I \approx \frac{cn\epsilon_0}{2}|E|^2, \tag{C.1}$$

where c is the speed of light, n is the refractive index of the medium through which the light propagates, ϵ_0 is the electric permittivity of free space and E is the electric field. Taking the irradiance to be 1 kW per m^2, and assuming $n = n_{air} \approx 1$, we find:

$$|E| = \sqrt{\frac{2 \times 10^3}{cn_{air}\epsilon_0}} \approx 868.02 V/m \tag{C.2}$$

Next, the assumption is made that the electric field is sinusoidal, i.e. $E = |E|cos(\omega t)$, where $\omega = 2\pi f = 2\pi c/\lambda \approx 3.77 \times 10^{15}$ rad/s for light with a wavelength of 500 nm (which happens to be the wavelength at which sunlight has a maximum intensity). The force on an electron, taking the amplitude of this electric field and the charge of an electron, is then

$$F = eE = 1.39 \times 10^{-16}N = m_e a = m_e \ddot{x}. \tag{C.3}$$

Filling in the equation for the electric field, we can find that

$$\ddot{x} = \frac{e|E|}{m_e}cos(\omega t),$$

so that

$$x = -\frac{e|E|}{\omega^2 m_e}cos(\omega t).$$

The displacement of the electron is then given by

$$x = -\frac{e|E|}{\omega^2 m_e}cos(\omega t),$$

and the maximum displacement is equal to

$$x = -\frac{e|E|}{\omega^2 m_e}, \qquad\qquad (C.4)$$

which yields $|x| = 1.08 \times 10^{-17}$ m, which is a very small displacement and effectively means that an electron would not move at all if sunlight is regarded as an electric field that drives the electrons back and forth. Even taking an effective electron mass of $0.02\ m_e$ only yields a displacement of 10^{-15} m. Therefore, this picture would not yield any rectification and is therefore not correct.